Department of Materials Science

PhD program in Materials Science and Nanotechnology   Cycle: XXXV

Charge and spin-dependent transport in devices for unconventional computing

Surname: Taglietti   Name: Fabiana

Registration number: 824315

Tutor: Prof. Marco Fanciulli

Coordinator: Prof. Marco Bernasconi

ACADEMIC YEAR 2021/2022

Contents

Abstract

The accelerating rise of data-intensive applications is pushing the conventional computing technologies towards physical and environmental limits. A necessity to rethink computing has emerged, starting from the study of alternative device physics, materials, and computational paradigms. A huge research field that is referred to as unconventional computing. Particularly interesting for this work is the so-called in-materia computing, based on the exploitation of the intrinsic physical properties and non-linear effects of materials to perform computation.

The work presented here focuses on the analysis of charge and spin-dependent transport in devices based on networks of shallow donors in silicon. Two different systems have been investigated: the dopant network processing units (DNPU) and silicon-on-insulator (SOI) based devices.

The DNPU are multiple electrodes nanoelectronic devices based on a network of arsenic atoms in silicon. They have already been proposed as a promising scalable platform for in material computing. In this work, we investigated the network's physical properties more in depth, in order to possibly expand the DNPU's computational capability. Charge transport has been analyzed, identifying the temperature ranges in which variable range hopping is the dominant mechanism. Hopping transport is responsible for the high non-linearity required for computation. In the hopping regime, it is also possible to obtain negative differential resistance behavior, necessary to solve linearly inseparable classification problems. The DNPU's response was also investigated in response to external stimuli, such as photoexcitation and static magnetic field, showing field dependent photoconductivity. Finally, we studied the possibility to incorporate the spin physics of the dopants, in order to obtain new extended spin dependent functionalities. Spin dependent transport has been investigated performing electrically detected magnetic resonance on the DNPU. Spin dependent recombination processes via clusters of arsenic dopants and silicon/oxide interface defects have been identified.

A second approach starts instead from the investigation of the material's properties, in particular phosphorus doped SOI substrates with different device layer thicknesses. Knowing the fundamental properties of the material and the associated computational power will allow to properly design a device, with tailored function-

alities. In particular, we focus on the analysis of the material's spin properties and on the identification of spin dependent transport mechanisms. It was possible to observe spin dependent scattering responsible for a reduction in the device's current in resonant condition. In addition, we observed spin dependent recombination between conduction electrons and silicon dandling bonds.

1 Introduction

Modern society has come to rely on computing technologies in everyday life, from conventional computers to the growing field of the 'internet of things' (IoT). This high demand on computing performance comes with the awareness that standard technologies limits are approaching. Since the 1960s, the driving force in the development of more performing technology has been the Moore's law [1]. This techno-economic model has enabled the technology industry to double the number of transistors on a microprocessor chip every two years, with resulting improvement of chip performance. We are now approaching the limit of this model, with prevision that the performance improvements will flatten approximately by 2025 [2][3][4]. One of the main reasons is that the miniaturization is getting closer to the physical limits, with transistors reaching the atomic scale. At this level, quantum effects cannot be neglected and can affect the device reliability. Another aspect to be considered is the incredibly huge amount of data that is produced and needs to be stored, transferred, and processed. This creates two problems to be addressed: energy consumption and memory bandwidth. It is estimated that approximately 10 % of the global electricity usage is spent in computing technology, involving some sort of data manipulation [5]. This number is unfortunately expected to rise rapidly [6], due to the exponential increase of data. This huge amount of energy, necessary for data storage or processing, results also in a terrible carbon footprint [7]. Moreover, conventional computers are based on the von Neumann architectures in which the processing and memory units are physically separated. This results in a substantial data movement between the two units, which is relatively slow and energy consuming. For data-intensive applications, these architectures have become now largely inefficient. This introduction gave a brief overview of the main issues of conventional computing technologies. A necessity to rethink computing technologies has emerged, starting from the study of alternative device physics, materials, and/or architectures but also exploring novel computational paradigms. This novelty research has contributed to the rise of the unconventional computing field.

1.1 Unconventional computing

The field of unconventional computing (UC) starts to be developed in the late 90s, gathering all the novel and unusual computational models, aimed at outdoing the classical approaches [8][9]. On the one hand, UC explores a wide range of materials and non linear effects that can be harnessed for computing. It takes inspiration from the mechanisms of information processing in physical, chemical and biological systems, and it exploits the functional properties of the materials to design optimal architectures for emergent computing devices. On the other hand, there is a parallel need for developing new efficient and more powerful computing paradigms. Therefore, UC comprehends also the quest of other ways to compute inspired by nature, the proposal of novel theories of computation, and software implementation of new algorithms. Unconventional computing is therefore a niche for interdisciplinary science, varying from computer science, physics, mathematics, electronic engineering, to chemistry, biology, materials science and nanotechnology [10] [11][12]. A great variety of computing approaches has been proposed during the last two decades. I report some examples: DNA computing, analog computing, mechanical computing, optical computing, spintronics, chaos computing [13] [14] [15] [16] [17] [18] [19]. In the following subsections, we will explore more in details two of the main branches of unconventional computing, often interrelated: neuromorphic computing and reservoir computing. The first one is the ensemble of novel hardware, circuits and algorithms that try to reproduce the neurobiological architectures and to mimic the learning capability of the human brain. The second one proposes a new computational framework suitable for temporal information processing, that exploits the dynamics of a complex high-dimensional non-linear system.

1.1.1 Neuromorphic computing

The term *neuromorphic* was originally coined by Carver Mead in 1990 [20] to refer to brain-inspired large scale adaptive analog technology, to be integrated in the conventional silicon technology. The definition can then be expanded to generic computing systems that are inspired by the biological architectures and working mechanisms of the brain. Biological brains perform complex tasks with extremely high energy efficiency. A typical human brain contains 10^{11} neurons and 10^{15} synapses, and the power consumption is estimated to be around 20 W. Considering instead a digital simulation of an artificial neural network of approximately the same size, the power consumption increases to 7.9 MW [21] [22]. The human brain uses a different architecture compared to the conventional computing systems: memory and data processing are not separated, leading to an enormous energy saving. In the brain, the

same elements can store and deal with complex data, and perform multiple tasks in parallel. Moreover, the brain has the intrinsic capability to learn: to receive information and to retain it as knowledge. It can respond to external stimuli and adapt to a changing environment, showing high plasticity. Finally, even noisy and stochastic signals can be processed with high precision. In-memory computing, learning and adaptability, massive parallelism, and robustness are some of the main features of the brain that researchers aim to integrate in neuromorphic computing systems. Neuromorphic computing is nowadays a vast field that comprehends different research topics [23]. A first approach, often referred to as neuromorphic engineering, aim at the realization of electronic devices or circuits, that emulate the working mechanisms of real neurons and synapses. Research is focused on the identification and consequent exploitation of physical phenomena to reproduce neural functions. New architectures are being investigated too. For example, neuromorphic devices can be integrated with the standard CMOS technology to develop neuromorphic circuits characterized by a non-von Neumann architecture. This sector grows in parallel with the necessity to develop new computational frameworks and algorithms capable of processing complex and unstructured data. On the one hand, the focus is on the simulation of biological neural networks. On the other hand, inspired by the way information are encoded and transferred in the brain, the necessity to model spikes. Therefore spiking neural networks have been designed to reproduce the action potentials in biological brains. The result is a new, more efficient, kind of computation that is event-driven. Underlying everything there is the demand for a new class of materials and devices that could meet the needs and expand the capabilities of neuromorphic computing.

1.1.2 Reservoir computing

Reservoir computing (RC) is a computational framework particularly suited for temporal/sequential information processing [24] [25]. It derives from studies on recurrent neural network models (RNN), such as Liquid State Machines (LSMs) and Echo State Networks (ESNs), respectively introduced by Maass *et al.* (2002) [26], T. Natschlger *et al.* (2002) [27], Jaeger and Haas (2004) [28], and Jaeger (2001, 2010) [29]. A reservoir computer is generally composed by two parts: a dynamical non-linear system, called the reservoir, and a readout layer. The concept of RC is to transform input data into a high dimensional dynamical state of the reservoir, that can be accessed by the readout layer. The main advantage of this approach is that the reservoir is fixed and only the readout is trained with simple, mostly linear, learning algorithms [9]. This makes the RC an efficient computational model, characterized by fast learning, resulting in low training cost. Within reservoir com-

puting applications, it is possible to find pattern classification (e.g. spoken digit recognition [30]), time series forecasting (e.g. non-linear autoregressive moving average (NARMA) time series prediction [31] [32],) pattern generation (e.g. limit cycle generation [33]), adaptive filtering and control, and system approximation. All these applications can be useful in a variety of field, spanning from biomedical (EEG, ECG, neural recordings, etc.), financial, environmental to engineering and robotics. Since the reservoir act as a black box, any system with 'sufficiently rich' dynamical behavior can be in principle used as reservoir, not only RNN. Hardware-based reservoir has therefore attracted interest for developing novel machine learning devices. A variety of physical reservoirs have been already demonstrated using electrical, photonic, spintronic, mechanical, and biological systems [34]. The underlying concept of physical RC is to exploit the intrinsic physical properties of the system to perform computation. Therefore, the urge in finding unconventional physical substrates available for computation with improved performance. As mentioned before, the physical reservoir needs to fulfill a few characteristics such as high dimensionality and non linearity. It must separate different inputs, but also be insensitive to unessential small fluctuations, such as noise. Finally, in order to process sequential data, a fading memory is necessary, meaning that the reservoir states have to be dependent on recent-past inputs but independent of distant-past inputs. Towards the application of hardware-based RC systems, a fundamental challenge is to understand what makes a 'good' reservoir and how the reservoir characteristics can be related to computational performance. A substrate-independent framework to characterise reservoir computers has been proposed by Dale *et al.* [35]. Using generic computational capacity measures, such as kernel quality rank, generalization capacity rank and memory capacity, it is possible to characterise the quality of potentially any substrate for RC.

1.2 Physical System for UC

As mentioned before, the development of unconventional computing called for an exploration of a wide range of substrates suitable for computation. Novel materials and devices have been investigated, new architectures proposed and working prototypes manufactured. One approach has been to employ standard CMOS technology in a novel non-von Neumann architecture, as in the case of IBM TrueNorth (2014) [36]. TrueNorth is one of the first neuromorphic chips, that integrated 1 million programmable spiking neurons in an area of 4.3 cm^2. Artificial neurons mimic the spike-base communication in the biological brain. Spike-based processing is very efficient, due to its event-base nature. Another approach is based instead on the exploitation of the intrinsic physical properties of the materials to perform computa-

tion, the so-called *in-materia* computing. Therefore the search of intelligent matter [37]: materials that can perceive inputs, change their properties in response to external stimuli, store information, adapt and learn. Computing in that case could be truly embodied in the physical system. Many materials or devices have been proposed, here we report some examples. Phase-change materials (PCM) have been widely investigated due to their storage capability, which enables in-memory computing [38][39][40]. These materials can be reversibly switched between amorphous and crystalline phases, with consequently changes in the electrical resistivity. A continuous level of resistivity can be stored in PCM in a non-volatile manner, enabling efficient matrix-vector multiply (MVM) operations. PCM devices have been already engineered in crossbar arrays, with a concrete possibility to further scaling and commercialization. Phase-change materials have been also integrated on photonics chips, in which the PCM memory can be written, erased, and accessed optically [41][42]. Another approach leaves aside the rigid grid-like architecture of the crossbar arrays, in favor of a more complex and disordered system that emulates the topology of the brain [43]. Self-assembled networks and disorder materials have therefore started to be investigated. For example, self-organized memristic nanowires networks have been proposed [44]. The idea is to exploit the complex behavior of the network instead of focusing on the single element, here the nanowire. Inspired by the biological neural networks, they are focusing on the synapses' behavior and communication processes, rather than trying to replicate single neurons. These nanowires networks have been already implemented as physical reservoir [45]. Another example is shown in [46] where percolating nanoparticles networks exhibit brain-like spatio-temporal correlations, criticality and avalanches. Atomic-scale switching processes between nanoparticles have been shown to mimic the integrate-and-fire mechanism of biological neurons [47]. One final approach we would like to discuss is evolution-in-materio [48]. Evolution-in-materio is a training method that uses evolution inspired genetic algorithms to tune the response of a complex non-linear material system. This artificial evolution allows to define physical variables (e.g. voltages) to be applied to the system in order to modify its behaviour, and to obtain a physical output (e.g. currents) that matches the desired response [49]. In such a way the material system is adapted in response to external stimuli and it learns how to perform a specific computational task. Using the evolutionary method, it has been possible to reconfigure designless gold nanoparticles network to perform all the Boolean logic gates [50]. The follow-up of this research employs network of disordered dopants atom in silicon [51]. The resulting devices, called dopant network processing units, will be treated later in this thesis.

1.3 Overview of the thesis

The aim of this thesis is the investigation of devices and materials suitable for unconventional computing. In particular, we focus on the analysis of charge and spin-dependent transport in devices based on arrays of dopants in silicon. The work presented here follows two approaches. The first one is an investigation of the physical properties of a working device, the dopant network processing units (DNPU), that has been already demonstrated to be capable of solving multiple computational tasks [51]. A deeper understanding of the physical properties could lead to an enlarged knowledge of the DNPU computational power. Special interest is put on the possibility to incorporate the spin physics of the dopants, to obtain new extended spin dependent functionalities. Our second approach starts instead from the investigation of the material's properties. We studied a phosphorus doped silicon-on-insulator (SOI) substrate, in particular spin dependent transport in it. Knowing the fundamental properties of the material and the associated computational power will allow to properly design a device, with tailored functionalities.

This thesis is organized as follow. In Chapter 2 a theoretical introduction of the physics of semiconductors will be given, to provide the necessary background to understand the results presented in this work. We will focus in particular on the electronic properties of shallow donors in silicon. The main charge transport mechanisms and spin-dependent processes will be also presented. Chapter 3 covers the experimental techniques and set-up used in this work. Electron paramagnetic resonance (EPR) and electrically detected magnetic resonance are here introduced (EDMR), together with the set up for the electrical characterisation of the devices. Chapter 4 presents the investigation of the dopant network processing units. An electrical characterization of different DNPUs is presented, analyzing charge transport mechanisms and the response to external stimuli, such as illumination and magnetic field. Finally, spin dependent transport is examined and discussed. In Chapter 5 an investigation of a SOI-based simple device is presented. Results on spin dependent transport in these substrates are presented and future applications discussed. Finally, Chapter 6 summarizes the main results of this work and presents future outlooks.

2

Shallow Donors in Silicon

The devices investigated in this thesis' work are based on silicon doped with shallow donors. Donor impurities, such as phosphorus or arsenic atoms in silicon, supply extra electrons to the conduction band. Donors are considered shallow when they introduce energy levels in the semiconductor energy gap located in the vicinity (typically less than 100 meV) of the conduction band edge. Doping is therefore a fundamental process in semiconductors electronics, since it allows to properly tune the characteristic of a semiconductor in terms for example of conductivity, charge carriers type and concentration.

In this chapter, we will introduce the main theoretical concepts that are necessary to understand the results presented in this thesis. We will focus on the electronic properties of shallow donors in silicon, giving a parametrization of the density of state as a function of the dopants concentration. Then, the possible charge transport mechanisms in doped semiconductors will be presented. Finally, the spin properties will be introduced and an overview of the spin dependent transport mechanisms will be given.

2.1 Electronic properties

Shallow donors in silicon introduce energy states in the energy gap, whose energy positions and broadening depend on the impurities concentration. At low concentration, typically $N_{dop} < 10^{16}$ cm^{-3}, dopant atoms are isolated. They are practically all at the same energy level, resulting in a peak in the density of state centred at $E_{dop,0}$. Increasing the dopant density, dopants are closer together and start to interact. Clusters of dopants are forming, resulting in a broadening of the dopant states in a dopant band D_{dop}. At higher concentrations, the DOS broadens significantly since dopant atoms within the clusters are interacting. Furthermore, the energy of this miniband start to approach the conduction band edge, because electrons are less bound to the dopant atoms in large clusters. At the critical concentration N_{crit}, clusters connect to each other such that electrons can move freely. The dopant band touches the conduction band and merges with it at concentration just above

Parameters	Si:P	Si:As
$E_{dop,0}$ (meV)	45.5	53.7
N_{ref} (cm^{-3})	3×10^{18}	4×10^{18}
c	2	1.5
N_{crit} (cm^{-3})	3.74×10^{18} [54]	8.5×10^{18} [55]
r $(eV\,cm^{-3/2})$	4.2×10^{-12}	4.2×10^{-12}
s (cm^{-3})	10^{19}	10^{19}
N_b (cm^{-3})	6×10^{18}	1.4×10^{19}
d	2.3	3

Table 2.1: Parameters for the estimation of the DOS. Values are from [52] and [53].

the critical one. The free movement of electrons results in a dc conductivity on a macroscopic scale, a typical metallic behavior. N_{crit} is therefore the concentration at which the Mott transition occurs, also called metal-insulator (M-I) transition. In order to understand the semiconductor behaviour, it is useful to know when the dopants band forms and where it is energetically located. We therefore report here the DOS parametrization proposed by Altermatt *et. al* in the case of phosphorus [52] and arsenic [53] dopants. The dopant band energy peak (E_{dop}) can be parameterized as follow, as a function of the number of impurities (N_{dop}) compared to the reference value(N_{ref}):

$$E_{dop} = \frac{E_{dop,0}}{1 + (N_{dop}/N_{ref})^c} \tag{2.1}$$

where $E_{dop,0}$ is the ground state of the dopants. All the parameters are reported in table 2.1. The values for phosphorus and arsenic dopants are reported, since the devices studied in this thesis are based on these dopants. We can note that the donor state of arsenic is situated deeper in the band gap, therefore the Mott transition occurs at higher concentration in Si:As compared to the Si:P. The broadening of the dopant band D_{dop} can be approximated by a Gaussian distribution function:

$$D_{dop}(E, N_{dop}) = \frac{N_{dop}b}{\sqrt{2\pi}\delta}exp\left[\frac{-(E - E_{dop})^2}{2\delta^2}\right] \tag{2.2}$$

where δ is the half-width of the dopant DOS and b is the fraction of bound states.

$$\delta = rN_{dop}^{1/2}(1 - e^{-s/N_{dop}}), \ b = \frac{1}{1 + (N_{dop}/N_b)^d}. \tag{2.3}$$

 Figures 2.1(a) and 2.2(a) show the simulated dopants band for different impurities concentrations in the case of phosphorus and arsenic respectively. It has been calculated using equations 2.1, 2.2 and 2.3. It is clear from the simulation that increasing the number of dopants atoms, the dopant band forms, widens and moves toward the

conduction band edge (E_c) considered at $E = 0$ meV in the plot. It is also visible in figures 2.1(b) and 2.2(b) the variation of E_{dop} as a function of the number of dopants, confirming the merging with the conduction band at high concentrations. Finally figures 2.1(c) and 2.2(c) show in details the broadening of the dopants band δ.
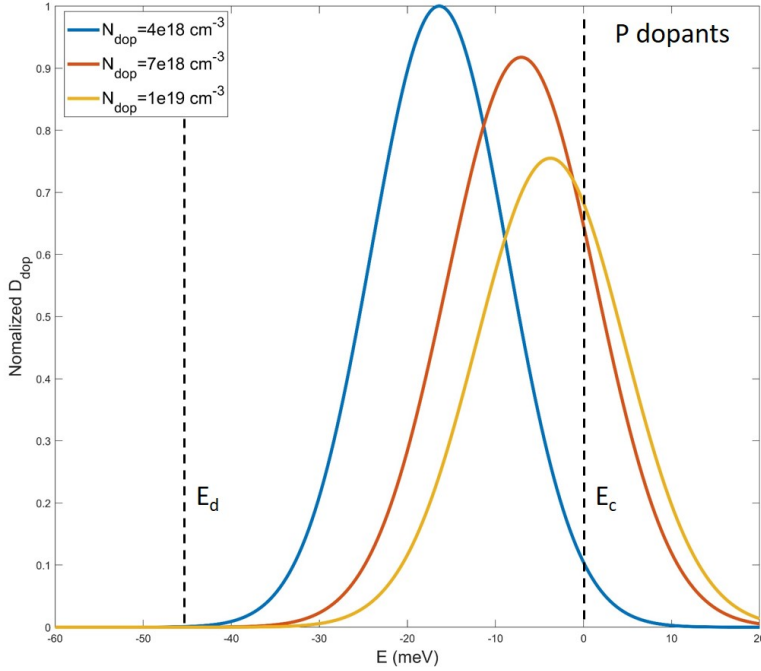
(a)
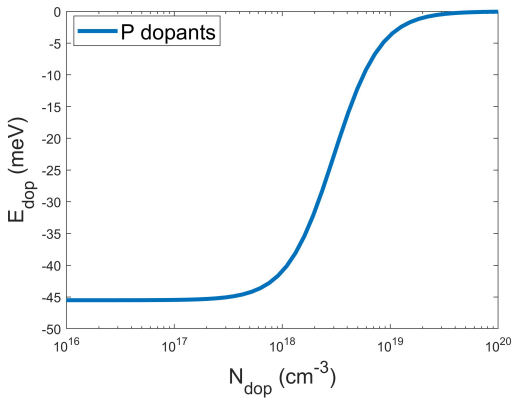
(b)
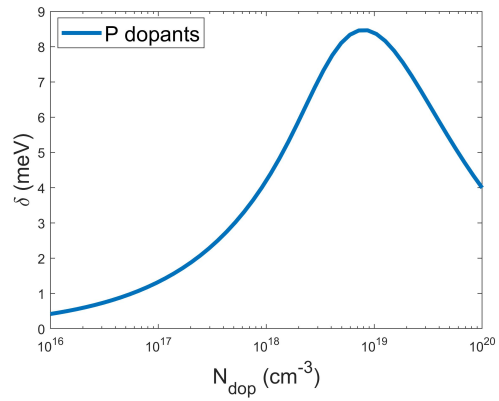
(c)

Figure 2.1: Phosphorus dopants: (a) dopants band for different impurities concentrations, (b) dopants band energy peak and (c) broadening of the dopants band as a function of the number of dopants.

An important parameter, that we will extract in the charge transport analysis, is the activation energy (E_{act}), intended as the energy to promote an electron from the dopant state to the conduction band. A first estimation of this value can be

(a)

(b)

(c)
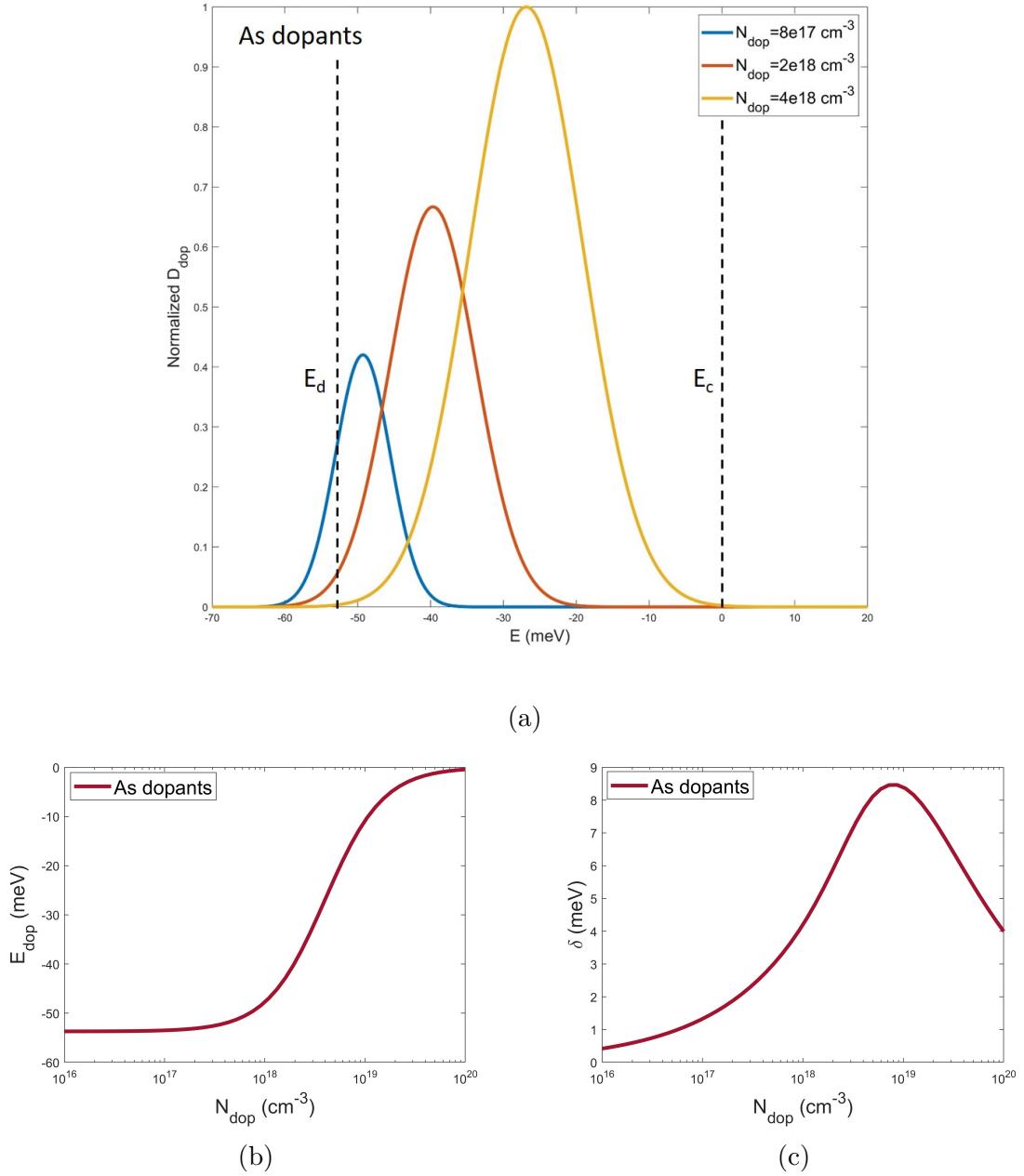
Figure 2.2: Arsenic dopants: (a) dopants band for different impurities concentrations, (b) dopants band energy peak and (c) broadening of the dopants band as a function of the number of dopants.

obtained using equation 2.1 that considers the doping level. Increasing the doping concentration the activation energy is reduced, as we saw before. However, higher activation energies are usually found experimentally in real silicon based devices. Some corrections in this case need to be considered, due for example to the dielectric mismatch with an oxide and quantum confinement possibly present in nanoscale devices. It has been measured in fact([56][57]), an increased activation energy for electrons close to the Si/SiO_2 interface. In this position, electrons feel a decreased dielectric screening and consequently a stronger electron confinement. The energy correction (ΔE) has been estimated by Pierre *et al.* in [58] for a dopant located at a distance z (nm) from the interface:

$$\Delta E \approx \frac{1}{4\pi\epsilon_0}\frac{e^2}{2z}\frac{\epsilon_{Si}-\epsilon_{SiO_2}}{\epsilon_{Si}(\epsilon_{Si}+\epsilon_{SiO_2})} \approx \frac{30.5(meV)}{z(nm)} \tag{2.4}$$

ϵ_0, ϵ_{Si} and ϵ_{SiO_2} are the dielectric constants of free space, silicon and silicon oxide respectively. A large correction is observed when dopants are very close to the interface ($z < 1\ nm$), resulting in the so-called dielectric confinements. At dopant concentration close to the critical one, a further correction have to be considered. A divergence of the silicon dielectric constant is in fact observed as N_{dop} approaches N_C. In figure 2.3 we report this behavior in the case of arsenic dopants. This divergence, usually referred to as dielectric anomaly, can be expressed by [59]:

$$\epsilon_{Si} = \epsilon_{Si_0} + \frac{4\pi N_{dop}\alpha_D}{1 - 4\pi N_{dop}\alpha_D/3\epsilon_{Si_0}}. \tag{2.5}$$

In this equation ϵ_{Si_0} is the dielectric constant in pure silicon estimated as 11.47,
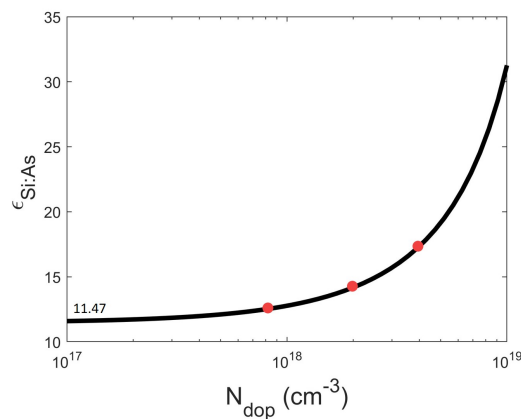
Figure 2.3: Dielectric anomaly for arsenic doped silicon. The red dots mark the nominal arsenic concentration in our DNPUs (Chapter 4).

N_{dop} is the number of impurities and α_D is the donor polarizability ($\alpha_D = 1\times10^{-5}\text{Å}^3$ for arsenic [60] [61]). Donor deactivation, resulting in increased ionization energy, has been also observed in nanoscale devices [56], due to both quantum and dielectric

confinement. This behavior has been predicted and calculated by Diarra *et al.* [57] for silicon nanowires, doped with phosphorus and arsenic donors. The nanowires surrounding is also important, since especially in nanoscale structures dielectric confinement becomes predominant. Finally, a deionization of dopants has been observed also in heavily doped silicon nanofilms [62]. In this work, Tanaka *et al.* evaluated E_{dop} as a function of the dopant concentration in silicon-on-insulator (SOI) FETs. Their results show a further increase in the activation energy when the device layer thickness is reduced below 10 nm. Considerations made before about dielectric mismatch and quantum confinement increasing E_{dop}, and high doping level decreasing it, are still valid. The further increase in the activation energy is attributed to the suppression of metal insulator transition in highly doped nanoscale SOI. The reason is to be found in the limited overlapping of the dopants potential in the confined direction of the SOI, resulting in the suppression of the impurity band formation.

2.2 Charge transport

In this section, we will introduce the temperature dependence of charge transport in doped semiconductors. The different charge transport mechanisms are here presented with the formalism used to describe transport in the dopant network processing units (Chapter 4).

In semiconductors, the intrinsic carrier concentrations of electrons (n) and holes (h) depend exponentially on the temperature, following:

$$n = p = \frac{(2\pi\sqrt{m_e m_h}k_B T)^{3/2}}{4\pi^3 \hbar^3} exp(-E_g/2k_B T) \tag{2.6}$$

where m_e and m_h are the masses of electrons and holes, and E_g is the semiconductor energy gap. The thermal activation of carriers across the band gap determines an intrinsic electrical conductivity in semiconductors at high temperatures. Due to the large values of the energy gap, the intrinsic carrier concentration decreases very rapidly with temperature. At sufficiently low temperatures the intrinsic carrier concentration becomes less than the one related to the impurities. The electrical conductivity is now referred to as extrinsic since it is determined by the concentration and nature of impurities. As seen in the previous section, shallow donors have ionization energies much smaller than the semiconductor energy gap. There exists therefore a temperature range, called the saturation range, in which all the impurities are ionized. The carrier concentration in the conduction band is temperature independent in this range. The band conductivity can be expressed as $\sigma = en\mu_e$, where e, n and μ_e are respectively the electron charge, concentration, and mobil-

ity. The temperature dependence of the conductivity is determined by that of the mobility. A further decrease in temperature leads to a gradual freezing-out of the impurities electrons that are recaptured on the donors levels, eventually leading to the hopping conductivity. In this situation, the main contribution to the electrical conductivity comes from electrons hopping between impurity states, without any excursion to the conduction band. We will now see more in detail the expressions for the electrical conductivity in the different temperature ranges, and the associated transport mechanisms.

Figure 2.4 shows a typical sequence of transport mechanisms becoming dominant in different temperature ranges. The variation of the density of state is also depicted on an appropriate scale. At high temperatures, electrons are thermally activated
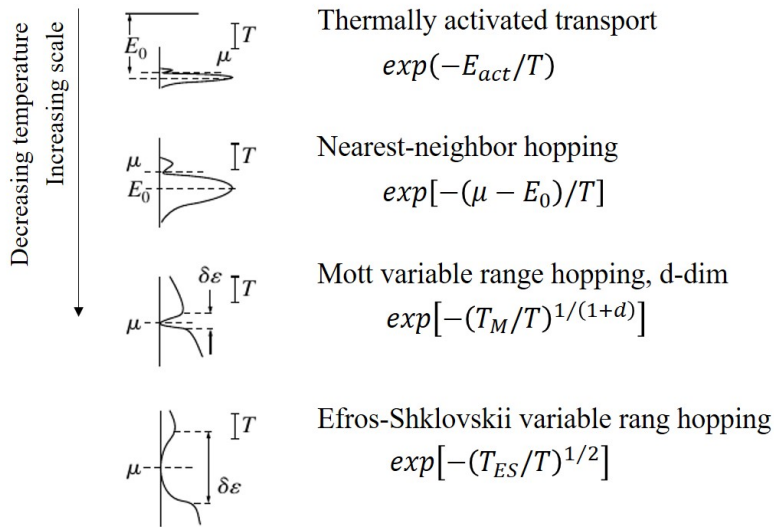
Figure 2.4: Changes of the hopping-conductivity mechanisms with lowering of the temperature. Figure is adapted from [63].

from the impurity levels to the conduction band. E_0 represents the energy difference between the minimum of the conduction band and the energy of the donors level, which we already discussed in section 2.1. We referred to this value as activation energy (E_{act}) in the previous section and we will keep this notation. The exponential decay of the conductance (σ) over the inverse temperature is the typical Arrhenius behavior for thermally activated mechanisms (equation 2.7). The electrical response of the semiconductor in this regime is linear.

$$\sigma = \sigma_0 \exp(-E_{act}/T) \tag{2.7}$$

Lowering the temperature we enter the hopping regime. The temperature at which this transition takes place depends on the dopant concentration: the higher the doping level the lower the cross-over temperature. To describe hopping conductivity it is useful to recall that at sufficient low temperature and dopants concentration,

electrons wave functions are localized on the donor states. The exponential tails of the wave function can overlap between neighbor donors, resulting in a finite probability of carrier transition from an occupied state to a free one. Let us consider an electron hopping from a site i to a site j. The energies of the donor states are practically all different. Therefore the hopping event is associated with a gain or loss of energy $\epsilon_{ij} = \epsilon_i - \epsilon_j$, meaning emission or absorption of a phonon. The transition probability can be expressed as:

$$1/\tau_{ij} \propto F(\varphi_{ij}, f_i, f_j)|\langle \psi_j | e^{iqr} | \psi_i \rangle|^2 \tag{2.8}$$

where ψ and e^{iqr} are respectively the donors and phonon wave functions. The function F represents the probability of having an empty level ϵ_j, an occupied one ϵ_i, and a phonon ϵ_{ij}. It depends on the Fermi (f_i) and Bose (φ_{ij}) distribution function, respectively for electrons and phonons:

$$f_i = \frac{1}{e^{(\epsilon_i - \mu)/k_B T} + 1}, \ \varphi_{ij} = \frac{1}{e^{\epsilon_{ij}/k_B T} - 1} \tag{2.9}$$

The obtained transition rate is:

$$\Gamma_{ij} = \frac{1}{\tau_{ij}} = exp\left(-\frac{2r_{ij}}{a_B} - \frac{\epsilon_{ij}}{k_B T}\right) \tag{2.10}$$

If we connect every donor with a fictitious resistance R_{ij} inversely proportional to the transition rate, we obtain the Abrahams-Miller equation modeling a random network of resistors:

$$R_{ij} = R_0 exp(2r_{ij}/a_B + \epsilon_{ij}/k_B T) \tag{2.11}$$

Following the Abrahams and Miller formalism [64], the problem of calculating the hopping conductivity can be reduced to the resolution of a percolation problem in a resistances network. It is possible to note that equation 2.11 is composed by two terms: a spatial and an energy one. At high temperature the latter is small, therefore the physical distance between donors is the dominant factor in the hopping probability. Transitions between sites located far away are less likely to happen, since the resistance increase exponentially. Lowering the temperature instead, the energy difference between the two sites becomes more important.

The simplest hopping transition happens between nearest neighbour states. The energy of these sites is most probably in the vicinity of the maximum of the density of states, that corresponds to the donor ionization energy E_0. Moreover, it is necessary to hop from an occupied site to a free one. Therefore only transition with energy $\epsilon_{ij} = |(\mu - E_0)|$ are allowed, where μ is the Fermi level. The resulting behavior of

the conductivity is:

$$\sigma = \sigma_0 \exp[-(\mu - E_0)/T)]$$ (2.12)

A further decrease in temperature such that $k_B T \ll |(\mu - E_0)|$, leads to a number of empty sites among the nearest neighbors that is too small. It is more convenient now for carriers to hop between states further away, but closer in energy. Therefore nearest neighbor hopping is now replaced by variable range hopping. The term 'variable' is related to the fact that the average hopping length is no more limited to the nearest neighbor, but can be larger varying with the temperature. It is possible to observe two different variable range hopping mechanisms, described by the Mott law and the Efros-Shklovskii law.

The Mott model [65] assumes that the donors states involved in charge transport are located in a small energy region in the vicinity of the Fermi level ($\mu \pm \varepsilon$). The density of states close to the Fermi level is considered constant (g_μ). The number of states in this energy region is then $N(\varepsilon) = g_\mu \varepsilon$, with an average distance of $\overline{r}_{ij} \approx [N(\varepsilon)]^{-1/d}$, considering a d-dimensional system. We can then express u_{ij} as:

$$u_{ij} = \frac{2}{g_\mu^{1/d} a_B \varepsilon^{1/d}} + \frac{\varepsilon}{T}$$ (2.13)

Minimizing this equation is possible to obtain the average energy difference in the hopping transition as:

$$\varepsilon \approx (T^d T_M)^{1/(d+1)}, \ T_M \approx (g_\mu a_B^d)^{-1}$$ (2.14)

whereas the average hopping length is

$$\overline{r} \approx a_B (T_M/T)^{1/d}.$$ (2.15)

Finally, the conductivity can be expressed as follow:

$$\sigma = \sigma_0 \exp[-(T_M/T)^{1/(d+1)}]$$ (2.16)

where T_M is the Mott temperature and d indicates the system's dimension. Therefore the temperature dependence is different in 2-dimensional ($T^{1/3}$) and 3-dimensional systems ($T^{1/4}$).

The Efros-Shklovskii model takes into account interactions between localized electrons, that results in the formation of the so called Coulomb gap in the density of states. The density of states in fact vanishes at the Fermi level [66][67]. The density

of states in the vicinity ε of the Fermi level can be expressed as:

$$g(\varepsilon) \propto \left(\frac{\kappa}{e^2}\right)^d |\varepsilon|^{d-1}, \ g(0) = 0 \tag{2.17}$$

where d is the space dimension and κ is the dielectric constant of the surrounding. Considering an energy interval $\mu \pm \varepsilon$, the number of states is now:

$$N(\varepsilon) \propto \left(\frac{\kappa\varepsilon}{e^2}\right)^d . \tag{2.18}$$

The average distance between donor states does not depend on the dimension d:

$$\overline{r}_{ij} \approx [N(\varepsilon)]^{-1/d} \approx \frac{\kappa\varepsilon}{e^2}. \tag{2.19}$$

As before we can derive:

$$u_{ij} = \frac{2}{\kappa a_B \varepsilon} + \frac{\varepsilon}{T} \tag{2.20}$$

and obtain the average change in energy and the average length of the hopping transition:

$$\varepsilon \approx (T T_{ES})^{1/2}, \ \overline{r} \approx a_B (T_{ES}/T)^{1/2}. \tag{2.21}$$

Finally, the conductivity varies with temperature following this equation:

$$\sigma = \sigma_0 \exp[-(T_{ES}/T)^{1/2}], \ T_{ES} \approx e^2/\kappa a_B \tag{2.22}$$

In the case of Efros-Shklovskii variable range hopping therefore, the conductivity temperature dependence does not depend on the system dimension.

To summarize, we present in the following figure 2.5 a schematic representation of the different charge transport mechanisms introduced in this section.
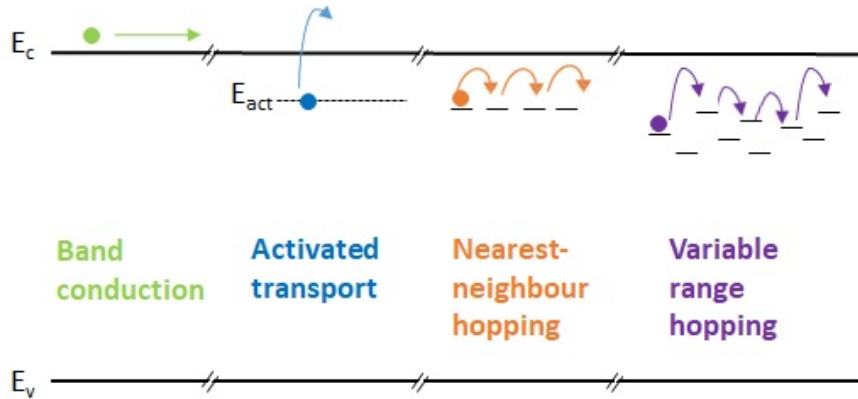
Figure 2.5: Schematic representation of the different charge transport mechanisms.

2.3 Spin properties

Shallow levels in semiconductors can be investigated with magnetic resonance techniques [68] [69] [70]. We introduce here the main spin properties of shallow donors in silicon. The electrons spin can be described by the following spin Hamiltonian:

$$H_S = H_{ZE} + H_{SO} + H_{HF} + H_{SS} \qquad (2.23)$$

The first term is the electron spin Zeeman contribution. It describes the interaction of an electron spin with an applied magnetic field ($\mathbf{B}$). It can be expressed by:

$$H_{ZE} = \mu_B g_e \mathbf{B} \cdot \mathbf{S} \qquad (2.24)$$

where $\mu_B = e\hbar/2m_e$ is the electronic Bohr magneton, $\mathbf{S}$ is the electron spin angular momentum operator and g_e is the Landé g factor of the electron, which due to the magnetic moment anomaly is not 2, but 2.0023193.... The orbital angular momentum, $\mathbf{L}$, of a non-degenerate electronic ground state is quenched (L=0). However, the interaction between the ground state (G) and excited states (n) admixes orbital angular momentum from the excited states into the ground state leading to:

$$H_Z = \mu_B \mathbf{B}(\mathbf{L} + g_e \mathbf{S}) \qquad (2.25)$$

The second term in the spin Hamiltonian is the spin-orbit coupling given by:

$$H_{SO} = \lambda \mathbf{L} \cdot \mathbf{S} \qquad (2.26)$$

where λ the spin orbit coupling constant.
The sum of the electronic Zeeman term, including the orbital angular momentum, and of the spin orbit coupling leads to the g-matrix $\mathbf{g}$

$$H_Z + H_{SO} = \mu_B \mathbf{B} \cdot \mathbf{g} \cdot \mathbf{S} \qquad (2.27)$$

where

$$\mathbf{g} = g_e \mathbf{1} + 2\lambda \mathbf{\Lambda} \qquad (2.28)$$

with

$$\mathbf{\Lambda} \equiv -\sum_{n \neq G} \frac{<G|\hat{L}|n><n|\hat{L}|G>}{E_n^{(0)} - E_G^{(0)}} \qquad (2.29)$$

The g-matrix is a measure of the contribution of the spin and orbital motion of the electron to its total angular momentum. It is an important parameter, also in experiments, because it is a fingerprint of the detected paramagnetic species and of

the point symmetry of the defect, as we will see better in chapter 3. It is generally anisotropic in crystals, and hence can be represented by a 3x3 matrix.

Electrons can also interact with the local magnetic field produced by the magnetic moments of the atom nuclei. This interaction between the electron spin and the nearby nuclear spin $\mathbf{I}$ is called hyperfine interaction and represents the third term in the spin Hamiltonian:

$$H_{HF} = \mathbf{S} \cdot \mathbf{A} \cdot \mathbf{I}. \tag{2.30}$$

$\mathbf{A}$ is the hyperfine coupling tensor, describing the interaction strengths due to isotropic (contact) and anisotropic (dipolar) contributions. Different donor species have different hyperfine coupling, resulting in different hyperfine splitting of the spin levels. For substitutional donors in silicon, $\mathbf{A}$ is dominated by the isotropic Fermi contact hyperfine interaction: $A = \frac{2\mu_0}{3} g\mu_B g_n \mu_n |\psi(r_i)|^2$. In the expression of A, μ_0 is the vacuum permeability, g_n is the nuclear g-factor, μ_n is the nuclear Bohr magneton, and $\psi(r_i)$ is the wavefunction at the nuclear site.

The last term in the Hamiltonian, H_{SS}, describes the spin-spin interaction resulting from the influence of nearby electrons. There can be two types of interactions: the dipole-dipole interaction expressed by the $\mathbf{D}$ tensor, and the exchange interaction expressed by the exchange integral $\mathbf{J}$ given by the overlap of the wave functions. $\mathbf{S}_1$ and $\mathbf{S}_2$ represent spin angular momentum operator for two nearby electrons.

$$H_{SS,D} = \mathbf{S}_1 \cdot \mathbf{D} \cdot \mathbf{S}_2 \quad H_{SS,J} = \mathbf{S}_1 \cdot \mathbf{J} \cdot \mathbf{S}_2 \tag{2.31}$$

For shallow donors in silicon, the most important contributions to the spin Hamiltonian are the Zeeman, spin-orbit, and hyperfine interactions. Figure 2.6 shows the splitting of the energy levels for an electron with spin $S = 1/2$ and a donor nucleus with nuclear spin $I = 1/2$ with isotropic interaction, in external magnetic field $\mathbf{B} = B\hat{z}$. These levels are the resulting eigenvalues of the first-order spin Hamiltonian:

$$H = H_Z + H_{SO} + H_{HF} = \mu_B \mathbf{S} \cdot \mathbf{g} \cdot \mathbf{B} + \mathbf{S} \cdot \mathbf{A} \cdot \mathbf{I}. \tag{2.32}$$

A magnetic field $B \neq 0$ brakes the degeneracy of the spin state, due to the Zeeman effect. The resulting energy levels has spin state $m_s = +1/2$ and $m_s = -1/2$, and energy $E = \pm 1/2 g\mu_B B$. A further splitting is obtained considering the hyperfine coupling $A \neq 0$, and the resulting nuclear spin state $m_i = +1/2$ and $m_i = -1/2$. Transitions between these energy levels are possible only when the Pauli exclusion principle is respected, meaning all the transitions with $\Delta m_s = \pm 1$ and $\Delta m_i = 0$. These transitions are indicated in figure 2.6, together with the resulting electron paramagnetic resonance (EPR) spectrum. We will introduce the experimental technique and all the details in the next chapter 3, here we just want to point out few
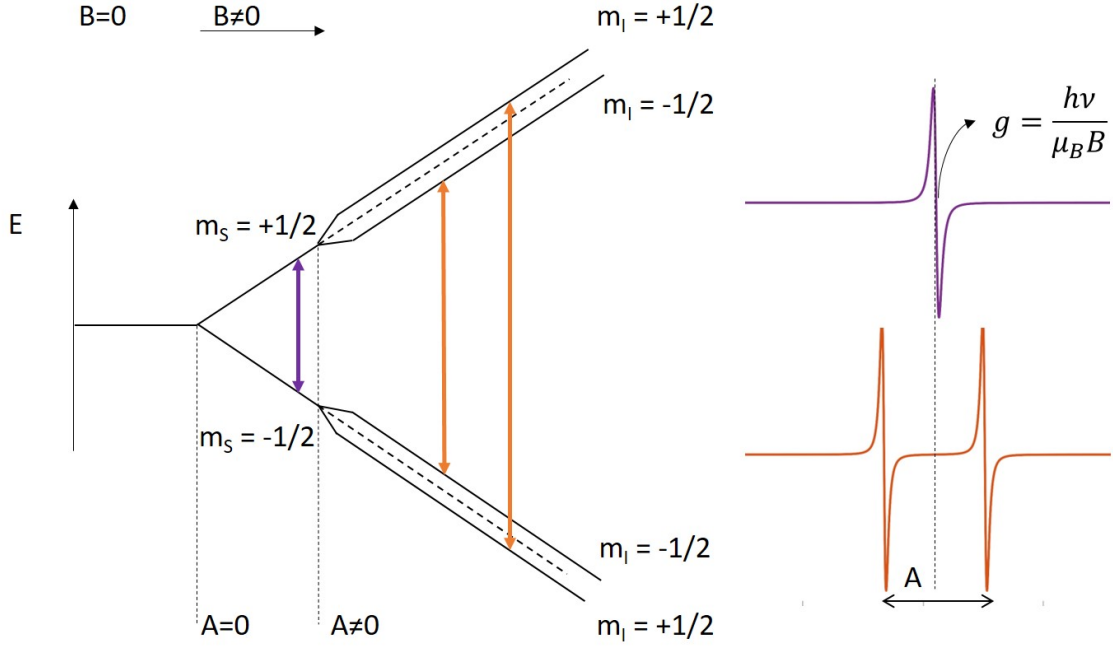
Figure 2.6: Energy levels and allowed spin transitions for a S=1/2 and I=1/2 system. The resulting EPR signals are also shown in absence (purple) and presence (orange) of hyperfine interaction A.

aspects. The splitting between the hyperfine lines is equal to $a_H = \frac{A}{g\mu_B}$ and it is specific for the detected donor. Also the number of hyperfine lines depends on the nuclear spin I, following the general rule $2I + 1$. For example in the case of arsenic donors, the expected hyperfine lines are four, since $I = 3/2$. Moreover, the hyperfine coupling depends on the dopant concentration. At concentration below the Mott transition, when electrons are localized on the donor states, it is possible to observe well defined and separate hyperfine lines. For high doping level instead, when clusters of donors form, the hyperfine lines collapse into one at the g-value of the specific donor. Information about the effective donor concentration can therefore be extracted from the presence or absence of the hyperfine lines.

Finally, in table 2.2 we report some parameters for the donors studied in this thesis, phosphorus and arsenic. The most abundant isotope, g-factors, nuclear spin, expected hyperfine lines, and hyperfine coupling, are listed below.

Donor	g-factor	I	HF lines	A [MHz]	A [mT]
^{31}P	1.99850 ± 0.0001	$1/2$	2	117.53 ± 0.02	4.2
^{75}As	1.99837 ± 0.0001	$3/2$	4	198.36 ± 0.02	7.1

Table 2.2: Spin parameters for phosphorus and arsenic donors. Values are from [71].

2.4 Spin dependent transport

In this section we will introduce spin dependent transport in silicon, focusing in particular on those transport mechanisms that involve shallow donors. The main mechanisms are illustrated schematically in figure 2.7, where D represents the donor levels, while I generally refers to defects at the silicon/oxide interface. The arrows indicate the possible transport mechanisms. Shallow donors at low temperatures have two charge states: the neutral D^0 single occupied, and doubly occupied D^- state. The doubly occupied state exists stable only in the ground state, the singlet state, where the two electrons have opposite spin. The triplet state, in which electrons have the same spin, is the excited state. Defects at and near the interface between silicon and the native or grown oxide on top of it typically generate a distribution of mid-gap states, that can also contribute to spin dependent transport. Examples of these defects are the silicons dangling bonds, such as P_b centers and E' centers [72], [73], [74]. P_b centers are formed by an unpaired valence electron of a silicon atom at the Si/SiO_2 interface. E' centers refer to the silicon dangling bond at an oxygen vacancy in the SiO_2 [75] near the interface.

(a) Spin dependent recombination

(b) Spin dependent trapping

(c) Spin dependent hopping

(d) Spin dependent scattering
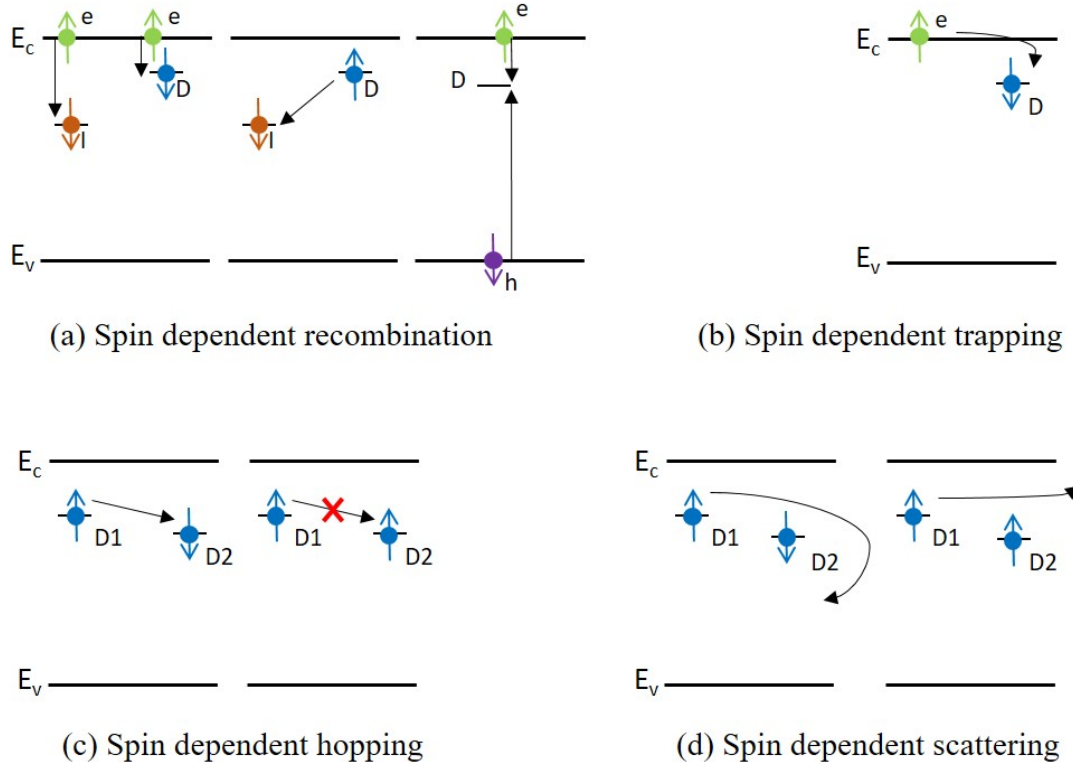
Figure 2.7: Schematic representation of the possible spin dependent transport mechanisms. D represents the donor states, while I generally refers to defects at the silicon/oxide interface.

Spin dependent recombination (figure 2.7 (a)) is one of the most studied mechanisms,

described for the first time by Lepine [76]. It can be easily detected in the variation of the photocurrent or current of a $p-n$ junction [77] [78] [79] [80] [81]. In the first case, the recombination between electrons and holes photogenerated in the conduction and valence band respectively is detected. The second case instead concerns the carriers recombination in the depletion region of the junction, without the need of photogeneration. The donor levels can act as recombination centers, capturing an electron from the conduction band and a hole from the valence band. The recombination is greatly enhanced if carriers can first be captured by a mid-gap defect state, and then recombine with another carrier on the donor state. Recombination on these defect states is also possible. In general, a variation in the recombination rate will produce a variation in the photoconductivity of the device under study, or in the $p-n$ junction's current. Therefore it is possible to identify the recombination centers that promote/hinder a spin dependent process increasing/decreasing its recombination rate. The schematic in figure 2.7(a) shows, in order, the recombination of conduction electrons and an interface defect, the recombination of conduction electrons and a donor, the recombination between donors and interface defects, and finally the recombination of photogenerated electrons and holes at a localized donor center. D^0 states can also act as trapping centers. A nearby conduction electron can be captured only if a singlet state is formed. Therefore we referred to this mechanism as spin dependent trapping. A schematic representation of the trapping mechanisms is depicted in figure 2.7 (b). Trapping mechanisms can also be an intermediate step for spin dependent recombination [82]. Spin dependent transport is also possible with electrons tunneling or hopping between localized donor states. The spin dependence is due to the spin Coulomb blockade. An electron can tunnel only onto a donor state with opposite spin, otherwise the transition is not allowed, and therefore blocked. An example of allowed/blocked hopping transition between donor states is schematically represented in figure 2.7(c). Finally, spin dependent scattering can also happen between mobile carriers and paramagnetic centers as depicted in figure 2.7(d) [83] [84]. Also in this case, the relative spin state of the species undergoing scattering, will affect the scattering rates and therefore the sample conductivity. For example, an increased scattering rate will reduce the sample conductivity.

Experimental Techniques

In this chapter, we will introduce the experimental techniques and setups that have been used to characterize the devices. The work presented in this thesis is mainly carried out at the MSNS laboratory (*Materials and Spectroscopy for Nanoelectronics and Spintronics*), in the Department of Material Science at the University of Milano-Bicocca. I also performed a part of the DNPU's characterization in the Nanoelectronics group's laboratory at the University of Twente (The Netherlands) during my research period abroad.

3.1   Electrical characterization

For the electrical characterization of our devices, a Keithley 4200A-SCS (Semiconductor Characterization System) Parameter Analyzer was used. This integrated parameter analyzer allows a full electrical characterization of semiconductor devices or materials. Our parameter analyzer has four DC I-V Source Measure Units (SMU), an AC Impedance Capacitance-Voltage Unit (CVU) and an I-V/C-V Multi-Switch Module that enables easy and fast switching between I-V and C-V measurements, without re-cabling or lifting the probe tips.
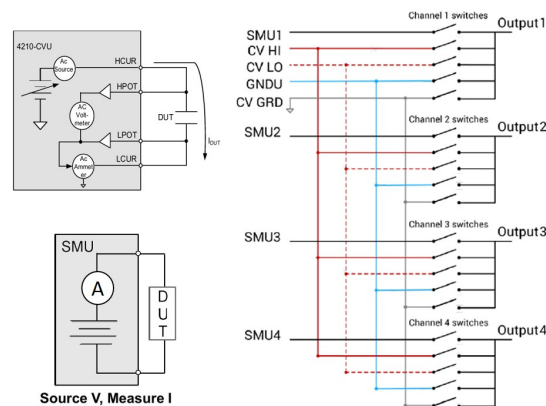
Figure 3.1: Connection schematic of the SMU, CVU and the CVIV module.

An SMU is a single instrument that can source current or voltage and measure both current and voltage. It is essentially a voltage or current source in series with a

current meter, connected in parallel with a voltage meter. We employ the 4200 medium power SMU with 4200-PA preamplifier that greatly enhances the resolution. The device under test (DUT) is then connected to the SMU with 4200-TRX-2 ultra low noise triax cables. SMUs with preamps are capable of exceptionally low current measurements, with a resolution of 10^{-17} A, making the 4200A-SCS the ideal analyzer to characterize nanoscale devices. The main characteristics of the SMU, including the preamp, are reported in table 3.1, in the source voltage-measure current configuration. The measurement accuracy depends on the selected current range. In the case of nanoscale devices, such as the DNPUs characterized in this thesis, we are interested in low current values, mainly below 1 μA. The accuracy is expressed as $\pm$ gain error plus an offset error. The first one, $\%rdg$, is calculated as a percentage of the reading values, while the second, *amps*, is a constant value that depends on the measure range.

Current Range	Resolution	Accuracy $\pm(\%rdg + amps)$
100 mA	100 nA	$0.045\% + 3\mu A$
10 mA	10 nA	$0.037\% + 300nA$
1 mA	1 nA	$0.035\% + 30nA$
100μ A	100 pA	$0.033\% + 3nA$
10μA	10 pA	$0.050\% + 600pA$
1μA	1 pA	$0.050\% + 100pA$
100 nA	100 fA	$0.050\% + 30pA$
10 nA	10 fA	$0.050\% + 1pA$
1 nA	1 fA	$0.050\% + 100fA$
100 pA	300 aA	$0.100\% + 30fA$
10 pA	100 aA	$0.500\% + 15fA$
1 pA	10 aA	$1.000\% + 10fA$

Table 3.1: SMU resolution and accuracy for different current ranges. The SMU is considered to be in the source voltage-measure current configuration.

C-V characterizations are performed with 4210-CVU Capacitance Voltage Units. The CVU is a multi-frequency (1 kHz to 10 MHz) impedance measurement module, that allows capacitance-voltage (C-V), capacitance-frequency (C-f) and capacitance-time (C-t) characterization. The CVU measures the DUT's impedance sourcing an AC voltage across the device and measuring the resulting AC current and phase. The AC voltage range is 100 mV rms (root mean square), while the AC current ranges are $1\mu A$, $30\mu A$, and $1mA$. The capacitance is then calculated from the

impedance and the test frequency:

$$C_{DUT} = \frac{I_{DUT}}{2\pi f V_{AC}}$$

The capacitance accuracy is given for specific capacitance values depending on the test frequency. An example compatible with our measurements is shown in Table 3.2 [1]. The measurement accuracy of the 4210-CVU is specified up to 100 nF, capacitance

Frequency	Measured C	Accuracy
1 MHz	1 pF	±1.17%
	10 pF	±0.19%
	100 pF	±0.10%
	1 nF	±0.09%

Table 3.2: CVU accuracy at a fixed test frequency, for different measured capacitance values.

values above this value can be measured but are not calibrated. Also the minimum capacitance that can be measured by the 4210-CVU is difficult to define because many variables in the test system need to be considered, such as test frequency, ac drive voltage, cables, device factors and correction. For example considering a test frequency of 1 MHz test and 30 mV rms drive voltage, the measurement accuracy of a 1 pF capacitor is ±0.38%. The CVU is supplied with four CA-447A SMA to SMA cables, 1.5 m long with 100 ohms impedance. Connecting together HCUR/HPOT and LCUR/LPOT, the two cables in parallel result in 50 ohms which is the standard for high frequency sourcing and measuring applications. SMUs and CVU are connected to the 4200A-CVIV Multi-Switch Module, where we can define up to four channels. The CVIV allows to switch effortlessly between I-V and C-V measurements. The same impedance during I-V and C-V tests can be maintained by keeping the probe tips on the same DUT terminals. SMUs and CVUs can be moved around on the device remotely, allowing a more stable setup configuration and reliable measurements. All the operations with the 4200-SCS are driven by Clarius (version 1.10.1), a GUI-based (graphical user interface) software that allows to configure and run the measurements, and to analyze the results. For a room temperature characterization, our devices are measured in the probe station shown in figure 3.2, using the four probe tips to contact the electrodes. A C-6 probe station from Everbeing Int'l Corp. is used, with four EB-050 micropositioners holding a 5 μm diameter tungsten tip. For a temperature dependent characterization, the devices are placed in a Leybold flow cryostat. Both liquid nitrogen and liquid

---

[1]Integration time: 1 s. Test signal level: 30 mV rms. All specifications apply at 23°C ±5°C, within one year of calibration, after 30 minutes of warm up.
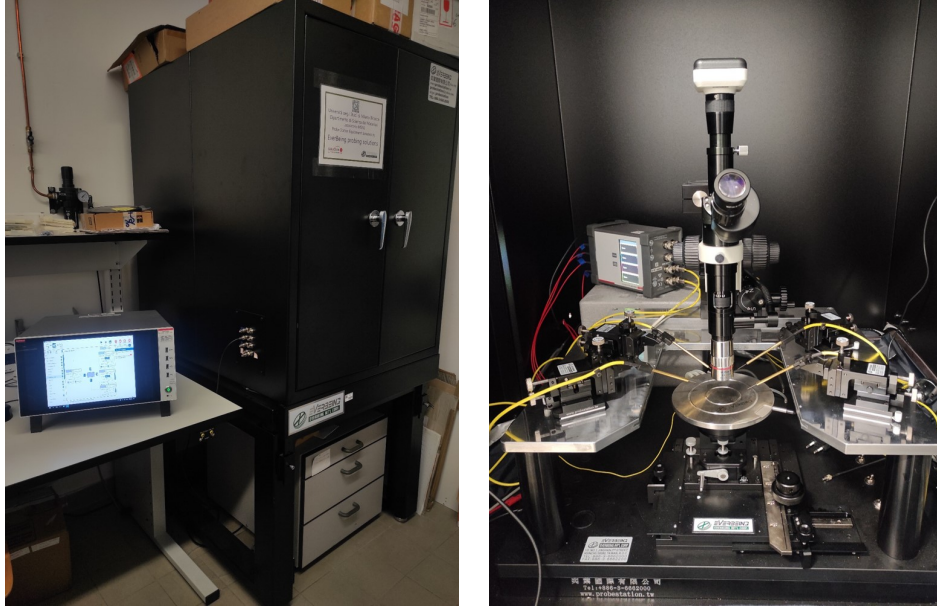
Figure 3.2: (Left) 4200A-SCS Parameter Analyzer running the Claurius software and connected to the probe station in the shielding box. (Right) Probe station: the DUT is allocated on the chuck and contacted with the probe tips, connected to the four channels of the CVIV switch.

helium can be used to cool down the system reaching the temperature respectively of 77 K or 5 K. The setup is shown in figure 3.3. A transfer line (Oxford Instrument Nanoscience LLT series) is used to get the cooling liquid from a dewar to the cryostat. A quartz window in the cryostat allows to access the samples. We exploited it to perform photocurrent experiments on the DNPUs, testing the response to different light colors. This window, together with a mounted sample, is shown in Figure 3.3. It is also visible how samples are connected. A TopLine TO-8 header, also in figure 3.3 is used as sample holder. The device under investigation is glued to the sample holder, then the electrodes are wire bonded[2] to up to 12 pins. The pins' legs are then connected to cables that come out of the cryostat in a 9 positions d-sub connector. A custom made box allows to re-separate the d-sub into eight coaxial cables. In this way, we can access eight different electrodes and easily switch between them from outside the cryostat, without changing the connection on the samples. However, with the 4200A-SCS Parameter Analyzer we can only measure up to four electrodes simultaneously.

---

[2]I would like to thank prof. Mario Zannoni and prof. Elena Ferri (Department of Physics "*Giuseppe Occhialini*" at the University of Milano-Bicocca), to let me use their wire-bonder (model: tpt HB16).

Figure 3.3: Leybold flow cryostat for electrical characterization of the devices at low temperature. An optical window allows to illuminate the device under investigation. On the right: a bonded DNPU.

3.1.1 Switch setup

In this section, I will introduce the setup I used to characterize the DNPUs at the University of Twente, the Netherlands. A schematic of the setup is shown in Figure 3.4. Up to eight DNPUs can be allocated simultaneously on a custom PCB (printed circuit board) and wire bonded with aluminum wires. The PCB is mounted on a dipstick, that is inserted in the dewar filled with liquid nitrogen. This configuration is useful to perform an electrical characterization at the fixed temperature of 77 K. Since the DNPUs operate in the hopping regime, this temperature is sufficiently low for most of the dopants concentration studied. The dipstick contains all the flat cables that connect the PCB to the junction box at the top of it. The junction box regulates the connection to the external electronics. An I/V converter is also placed on the PCB, to convert the small current coming from the DNPU into a voltage signal. A feedback resistance of 10 MΩ is used to tune the ratio current/voltage. An external power supply provides the $\pm 5V$ for the operational amplifier. Finally, input voltage and output current can be controlled and measured with the National Instruments modules. Input voltages are generated by NI 9264 analog output module. The DNPU's current output converted into voltage, is then detected by the NI 9202 voltage input module. Finally, the NI 9472 digital module controls the digital input/output. This setup has 8 DAC and 1 ADC channels, and electronic switches to define the device to which these channels are connected. The possibility to switch from device to device and to easily control all the electrodes, makes this setup versatile for a fast characterization of multiple devices. The modules are controlled by

Python codes SkyNEt and Brainspy (https://github.com/BraiNEdarwin). I mainly worked with SkyNEt, writing the codes necessary to analyze the DNPU's electrical response in different configurations. Brainspy was used to perform Boolean logic gates and ring classification with the DNPUs.
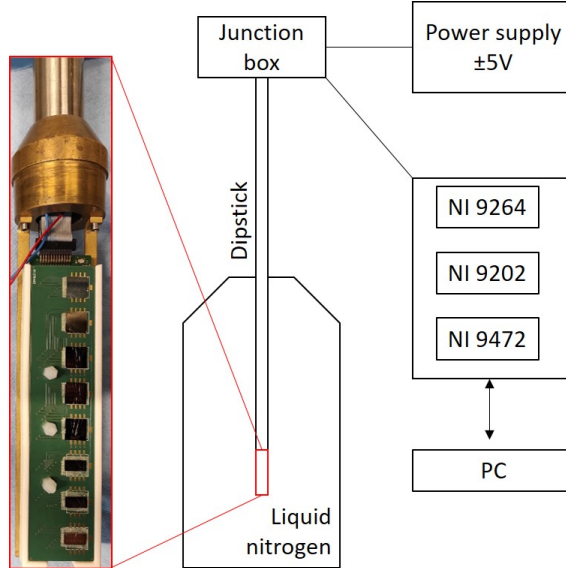
Figure 3.4: Schematic of the *switch* set up at the University of Twente, The Netherlands. The PCB is also shown, with eight DNPUs bonded on it.

3.2 Electron spin resonance spectroscopy

Electron spin resonance spectroscopy is a useful technique to address the paramagnetic states in materials. In semiconductors especially, it can be used to investigate dopants, both shallow and deep, and defects centers. In Chapter 2 we introduced the main spin properties, necessary to understand the spin resonance experiments. In this section, we will focus on the experimental apparatus and technique, employed in this thesis work. We will first focus on the conventional electron paramagnetic resonance experiments (EPR). Then we will proceed with an introduction to the electrically detected magnetic resonance technique (EDMR), important in the investigation of spin dependent transport mechanisms.

3.2.1 EPR

As already introduced, the presence of a magnetic field causes the splitting of the energy levels of the spin states $\pm 1/2$, due to the electron Zeeman effect. The energy level separation (ΔE) is proportional to the applied magnetic field B_0, following equation 3.1. A resonant absorption occurs when an incident radiation is sent with an energy that matches this ΔE [85].

Continuous wave EPR (cw-EPR) experiments are performed using a fixed microwave source at a given frequency $\nu_{\mu w}$ and sweeping the magnetic field. The resonant condition is thus achieved when:

$$h\nu_{\mu w} = \Delta E = g\mu_B B_0. \tag{3.1}$$

We operate with microwaves at a fixed frequency in the X band, typically $\nu_{\mu w} \approx 9.4\,GHz$. For electrons with g-factor ≈ 2, the resulting resonant magnetic field (B_0) is about 335 mT. In Figure 3.5 a schematic of the conventional cw-EPR spectrometer is shown, with its main components. We employed a Varian E15 EPR spectrometer. The sample is placed in a resonant cavity, which admits microwaves through an iris.
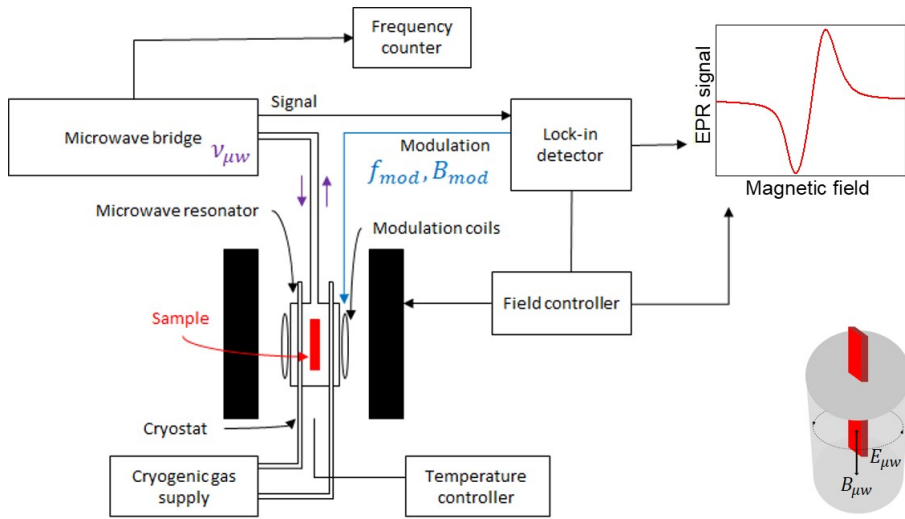
Figure 3.5: Block schematic of the EPR spectrometer showing the main components. A schematic of the X-band cylindrical TE_{011} microwave resonators is also displayed: $E_{\mu w}$ and $B_{\mu w}$ are the microwave electric and magnetic fields, respectively.

We employ a Bruker super high-Q cylindrical cavity (EF4122sHQ), that resonates in the X-band. Cavities are designed to place the sample in the microwave electric field minimum and the magnetic field maximum, in order to achieve the highest sensitivity. The cavity is in between electromagnets that apply a static magnetic field up to 1 T, with a minimum step of 0.01 mT. For low temperature measurements, the cavity is placed in a flow cryostat (Oxford instrument ESR900). Using liquid helium we could perform EPR/EDMR measurements down to 4.2 K. Microwave source, a klystron, and detector are placed in the microwave bridge. Microwaves are sent down to the cavity passing through a variable attenuator, that controls their power. In our measurements, microwave power between 0.5 mW and 190 mW has been used. The detector then measures the radiation reflected back from the sample in the cavity. The change in the amount of radiation is due to microwave absorption of the sample in resonant condition. The detector is a Schottky diode, that converts the microwave

power into electrical current. The signal is then fed into the detection system for amplification and processing. To enhance the sensitivity of the spectrometer phase sensitive detection is used, with a dual phase lock-in amplifier (Stanford Research SR830 DSP). A small ac magnetic field modulation B_{mod} is superimposed to the field B_0. The typical modulation frequency (f_{mod}) for EPR measurements is of about 100 kHz. The detection then is only sensitive to signals with the same frequency and phase as the field modulation, allowing to filter out any other signals, such as noise and electrical interference. In order to enhance the signal, without distorting it, the modulation amplitude needs to be smaller than the expected linewidths of the resonance lines. The detected signal is the first derivative of the resonance absorption with respect to the magnetic field [69]. The detected g-factors are calibrated with the reference DPPH ($\alpha, \alpha' - diphenyl - \beta - picryl\ hydrazyl$) signal ($g = 2.0036$).

3.2.2 EDMR

Electrically detected magnetic resonance is a modification of the conventional EPR technique first introduced by Lepine in 1972 [76][81] [83]. It is based on the measure of the variation of the sample electrical conductivity in resonant condition, instead of monitoring its microwave absorption. The sensitivity is therefore enhanced since we are no longer limited by detection diode sensitivity. Moreover, the conductivity is independent of the sample size, enabling also the investigation of nanoscale devices. All these features make the EDMR a suitable technique to investigate spin dependent transport mechanisms in electronic devices. The paramagnetic centers that are involved in spin dependent transport can be detected and identified with their g-factors. Also, information about the transport mechanisms can be extracted considering the signal phase. Different EDMR experiments can be performed aimed at identifying specific spin dependent transport mechanisms. For instance, when spin dependent recombination processes are investigated, EDMR is performed monitoring the device's photocurrent. Illuminating the sample, carriers are photogenerated in the conduction/valence band and their recombination with interface defects or dopants can be investigated. Another possible way consists in studying the spin dependency of recombination/generation processes in the depletion region of a $p - n$ junction. EDMR can therefore be performed on an inversely polarized junction, without the need of carrier photogeneration [77]. EDMR measurements can be performed also simply monitoring the current through the device under test. In this configuration spin dependent scattering mechanisms can be identified. Signals of the paramagnetic centers involved in the scattering process will be detected in the EMDR spectrum. An increase in the measured current in resonant conditions corresponds to a reduction of the scattering rate and vice versa. The basic
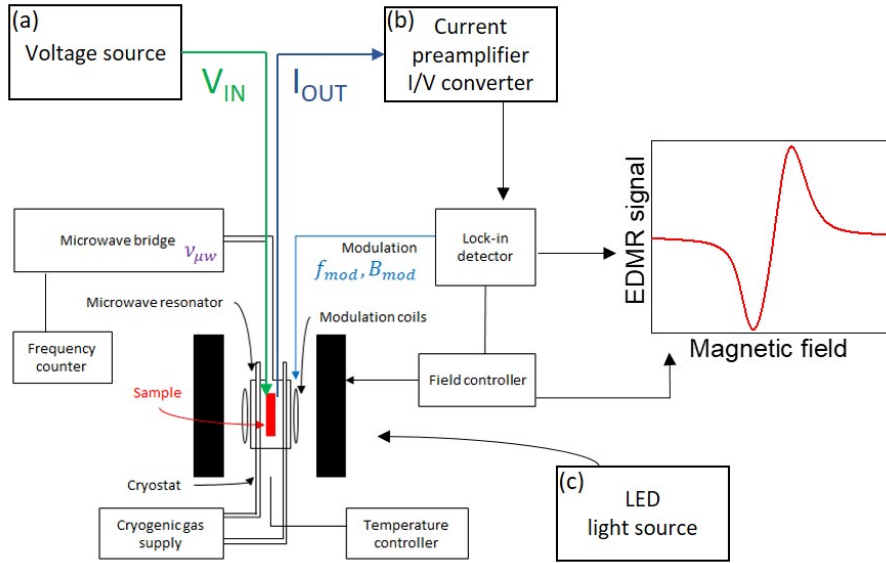
Figure 3.6: Schematic of the EDMR set-up. Here we highlight the components that are specific for EDMR measurements: (a) Voltage source. (b) current preamplifier. (c) light source.

of the EPR spectrometer remains the same, with a fixed microwave source and a scan of the magnetic field. The modulation frequencies used are now below 10 kHz, to ensure that the measured signals are not attenuated by parasitic RC delay in the measurement set-up. Typically in our experiments we use a modulation frequency of 5 kHz. The microwave power is 190 mW, the highest possible, in order to increase the signal intensity. In a EDMR experiment the samples need to be electrically connected to the bias and detection circuitry. A constant voltage bias is applied to the sample with a HP 4140B pA Meter / DC Voltage Source. The output current is then fed into a low noise current preamplifier (Stanford Research System, Model SR570), converted into a voltage signal and sent to the lock-in (Figure 3.6). In our experiment, unless otherwise stated, we monitor the sample's photocurrent. The studied devices are therefore illuminated with a blue or red led. Standard two electrode devices are mounted on a quartz tube and connected to the circuitry with coaxial cables. In the case of the DNPUs (see section 4.5) a customized PCB is employed to connect all the eight electrodes together with the back gate. A schematic is presented in Figure 3.7. The PCB terminates with a d-sub connector, connected to the box introduced in the previous section. Also for EDMR measurements we want the possibility to choose the combination of electrodes, without re-bonding the DNPU.
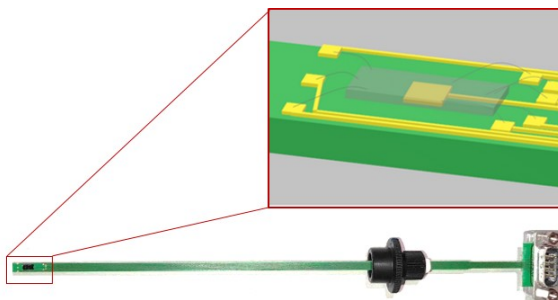
Figure 3.7: Custom made PCB to perform EDMR on nanoscale devices. Up to eight electrodes can be connected simultaneously, together with a back contact.
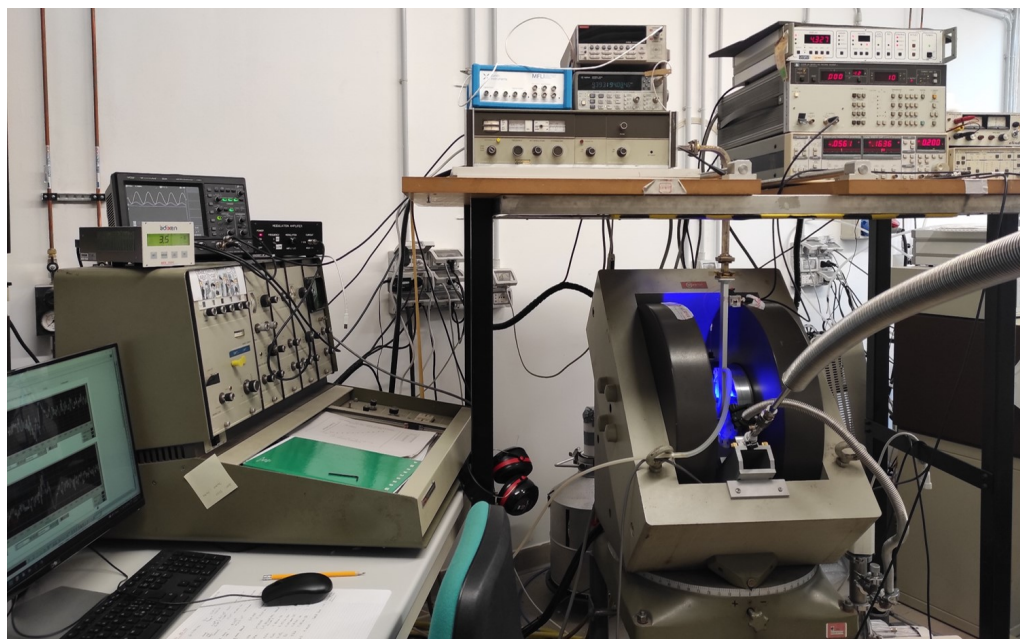
Figure 3.8: Picture of the EPR/EDMR set-up in the MSNS laboratory at the University of Milano-Bicocca.

3.2.3   EPR/EDMR Data fitting

EPR and EDMR data are then analyzed in order to extract the g-factors and lineshape of the detected paramagnetic centers. The measured spectra are fitted using the MATLAB toolbox EasySpin (version 5.2.35) [86]. The function *pepper*, specific for cw-EPR, is employed. EPR/EDMR signals are fitted considering a normalized Lorentzian absorption lineshape centred at x_0:

$$f_L(x) = \frac{2}{\pi\sqrt{3}\Gamma}\left[1 + \frac{4}{3}\left(\frac{x - x_0}{\Gamma}\right)^2\right]^{-1} \tag{3.2}$$

In particular, for our measurements we used the first derivative:

$$\frac{df_L}{dx} = -\frac{16}{\pi 3\sqrt{3}}\frac{x - x_0}{\Gamma^3}\left[1 + \frac{4}{3}\left(\frac{x - x_0}{\Gamma}\right)^2\right]^{-2} \tag{3.3}$$

Γ represents the peak-to-peak distance and it's related to the FWHM (full width at half height) via $\Gamma = FWHM/\sqrt{3}$. Applied to our experimental data, x_0 corresponds to the resonant field converted then to the g-factor, while Γ is the signal linewidth in mT. Also the signal intensity, intended as absolute weight (not relative), can be extracted by the fitting procedure. Finally the RMSD (root mean square deviation) is given describing the deviation of the experimental from the simulated spectrum. RMSD close to zero indicates a good fitting.

4 Dopant Network Processing Units

The *Dopant Network Precessing Units* (DNPU) are nanoscale devices designed and fabricated by the nanoelectronics group, leaded by Prof. Wilfred G. van der Wiel at the Center for Brain-Inspired Nano Systems (BRAINS), University of Twente (The Netherlands). During my Ph.D. I had the possibility to spend seven months in the nanoelectronics group, in the framework of the collaboration between Prof. Marco Fanciulli and Prof. Wilfred G. van der Wiel. In this period I was introduced to the DNPUs, their working mechanism and computational capability.

The DNPU consists on a network of randomly distributed acceptors or donors in silicon with an active area of 300 nm diameter, surrounded by eight electrodes. The DNPUs have been recently proposed [51] as a promising scalable platform for in materia computing, thanks to their ability to perform non-linear projection intrinsically. The non linearity is given by the hopping nature of charge transport in the dopant network. At sufficient low temperature and dopants concentration, carriers are localized and hop from dopant atom to dopant atom. Applying voltages to the electrodes then, allows to modify the response of the DNPU, resulting in a more complex non-linearity. In a typical experiment, two electrodes are used to send a voltage input, one electrode is used to measure the current output and the remaining ones are used to apply control voltages. The control voltages allow to electrostatically tune the potential landscape of the dopant network and to produce the desired output. It has been demonstrated that the DNPUs can be reconfigured through artificial evolution to solve all the different Boolean logic gates. In Figure 4.1 we report an example of a DNPU solving the XOR gate. The combination of control voltages that results in the correct output is found with genetic algorithms. The XOR gate is an important benchmark, because it demonstrates the DNPU's capability to solve linear inseparable classification problems. According to Cover's theorem [87], linearly inseparable classification problems can transform into linearly separable problems when non-linearly and sparsely mapped to a higher dimensional space. In the DNPU case, the high dimensional feature space is given by the dopant network potentials. The non linear projection is the result of the tunable hopping

behavior. It has also been demonstrated [88] that a single DNPU has a capacity
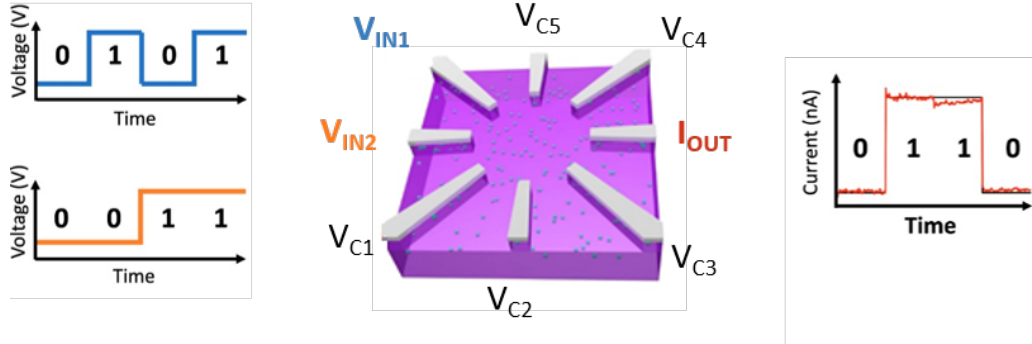
Figure 4.1: Example of a DNPU solving the XOR logic gate, showing the working mechanisms. Electrodes e_1 and e_2 are used to send an input voltage, in particular all the possible combinations of 0 and 1 over time. An electrode e_{out} is grounded and measures the output current. All the remaining electrodes applied control voltages. The right combination of controls results in the desired output current. The black line in the output is the target (XNOR) and the red line is the measured current.

comparable to that of a small neural network, with one hidden layer. A deep-learning approach has been used to realize different functionalities in a fast and fully automated way, without experimental parameters optimization. The multi-dimensional input-output characteristic of the DNPU can be emulated by a deep neural network (DNN) model. The DNN is trained and then the desired functionality is then searched in it, by using gradient descent on the control parameters of the DNN. Finally the functionality is verified by applying the corresponding control voltages to the physical device. With this method, they were able to find all of the Boolean functionalities almost two orders of magnitude faster than before, with the evolutionary algorithm approach. Furthermore, ring classification and a 2×2 pixel feature mapping functionality have been demonstrated.

It is then possible to move from a single to a multi-node framework, by training and implementing a feed-forward DNPU network. A network with five nodes (DNPU) can achieve an accuracy of 94% on a linearly inseparable binary classification task, while the accuracy for a single DNPU was 77%. Furthermore, simulations show that an MNIST (*Modified National Institute of Standards and Technology* database) classifier with only 10 DNPU nodes achieves over 96% test accuracy, making the DNPU a promising candidate for nodes in hardware neural network emulators. Finally, a recent work [89] introduces the DNPU as tunable extreme learning machine, performing formant-based vowel recognition.

In the framework of this collaboration, we carried out a parallel work aimed at investigating the physical properties of the DNPU more in depth. A full comprehension of the network's behavior could lead to an enlarged knowledge of the DNPU computational capability. A new physical property, properly optimized, could ex-

tend the device's functionalities. We followed two new research lines. The first one regards the study of the DNPU's photoconductivity. The DNPU's electrical behavior is studied in response to light sources with different wavelengths. I started this research in Twente, then we expanded it in Milan, showing that a static magnetic field has an impact on the photoconductivity. The second one wants to incorporate the spin physics of the dopants. Therefore spin dependent transport in the dopant network is investigated. If the spin properties are involved, then we could speculate on how to manipulate them to enhance the complexity of the DNPU's behavior. It could be in principle possible to perform not only an electrostatical tuning of the potential landscape of the network, but also a magnetic tuning. Further work and discussion are in progress to explore more spin functionalities in the DNPU and to understand how to exploit them from a computational point of view.

In this chapter, I will report my investigations on the DNPU based on arsenic dopants. First I will show the main aspects of the DNPU's fabrication, that was carried out at the University of Twente by Dr. Bram van de Ven. Second, an analysis of the charge transport mechanisms is presented, together with a characterization of the electrical tunability of the network. Then we will see how the DNPU's response can be affected by external stimuli, such as illumination or/and the presence of a static magnetic field. Finally we investigated spin dependent transport mechanisms, performing electrically detected magnetic resonance on the DNPU.

4.1 Design and Fabrication

The fabrication of the DNPU was carried out by Dr. Bram van de Ven at the University of Twente (The Netherlands). The full procedure and all the details can be found in his Ph.D. thesis [89]. Here for clarity, I report only the main fabrication steps and concepts, that are necessary for picturing the DNPU and for understanding the working mechanism. I will describe the fabrication of Si:As DNPU, since the results presented in this thesis are obtained with these dopants. Arsenic DNPU are fabricated using a one-side polished p-type Si(100) wafer ($\rho = 5.00 - 10.00\Omega cm$). The background doping reduces the implantation depth, forcing the dopants closer to the surface. This facilitated the fabrication process, without interfering in the network conductance. 300 nm of SiO_2 are grown on the wafer with dry oxidation. Then photolitography is used to define the implantation regions of $26 \times 60\mu m^2$. After etching these regions, dry oxidation is used to grow 25 nm of SiO_2. The oxide layer allows to obtain the highest implantation concentration at the surface, that is needed in order to achieve an ohmic contact with the metal electrodes. Ion implantation is then performed at 35 keV with 1×10^{14} atoms/cm^3. To incorporate
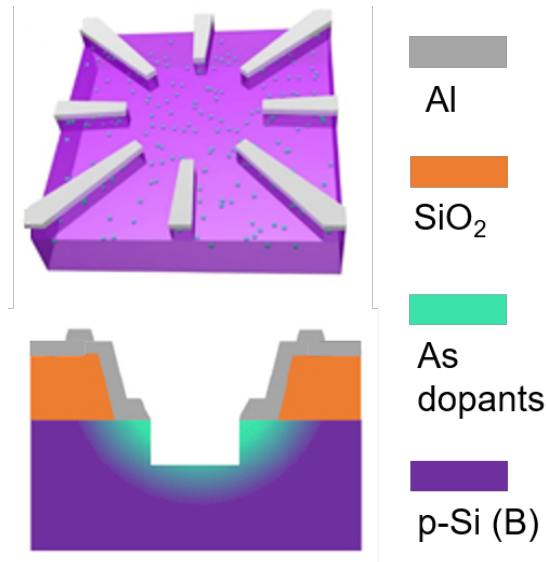
Figure 4.2: Schematic of a Si:As dopant network processing units.

the dopants into the Si lattice, rapid thermal annealing is performed (1050 °C for 7s), followed by etching to expose the highly doped silicon surface. Finally markers for electron-beam lithography (EBL) are made with a combination of sputtering and lift-off. After that, the wafer is diced in chips of $1 \times 1 cm^2$ on which the nanoscale processing is made. Metal electrodes to contact the DNPU are made by EBL, electron beam evaporation, and lift-off, with cleaning procedures and etching steps in between. The resulting structure is composed by eight electrodes, approximately 50 nm wide, evenly spaced on a circle with a diameter of 300 nm. The electrodes are made of 25 nm of aluminum. The final step in the DNPU's fabrication is to remove the excess layer of doped silicon using reactive ion etching (RIE). The duration of this process, consequently the etching depth, depends on the desired concentration. Typically for the arsenic DNPU, 1-3 minutes are sufficient to reach a concentration of 10^{17} atoms/cm³. DNPUs with this surface concentration typically operate in the hopping regime, at the liquid nitrogen temperature. Reaching the correct concentration is the main limiting factor in the yield of the DNPU, making the final RIE the most delicate and crucial step. At the end of the fabrication process, 45 chips can be obtained from a 4-inch wafer, each with 16 DNPUs. The process described is reliable and could be in principle applied to a variety of hosts and dopants. The only requirement is that a proper dopant concentration, resulting in a non linear conduction, is found.

Figure 4.3 shows the doping profile resulting from the arsenic atoms implantation in the B-doped substrate. Two profiles are actually here compared. The first one, in black, is the result of the implantation process simulation performed by Dr. Lucia Zullino (STMicroeletronics) with Sentaurus Device. The second one, in red, is the doping profile extracted from ToF-SIMS measurement of the implanted region,

performed by Dr. Michele Perego (IMM-CNR). It is clearly visible in the plot the matching between the two profiles. The DNPUs investigated for this thesis work, have an etching depth of 25 nm, 30 nm, and 35 nm. Assuming that these values are correct, the corresponding dopant concentrations at the surface are approximately 4×10^{18} atoms/cm^3, 2×10^{18} atoms/cm^3, and 8×10^{17} atoms/cm^3 respectively. We already mentioned that the final etching step is the most critical one. Therefore we would like to remind that these concentrations must be taken as nominal. Looking at the doping profile, small variations in the etching depth especially in the region around 30 nm, result in significantly different dopants concentration.
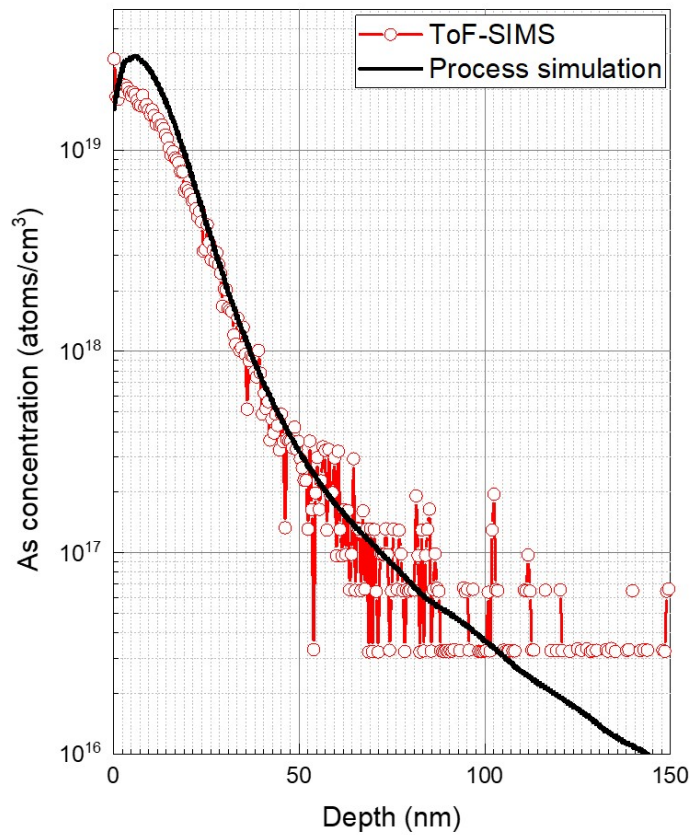
Figure 4.3: Arsenic doping profile resulting from the Sentaurus Device process simulation and TOF-SIMS measurements.

4.2 Charge transport

As introduced before, the non linear response of the DNPU is a fundamental feature for in materia-computing. The ability to perform non linear projection intrinsically is exploited to solve different classification problems. The non linearity is obtained when the DNPU operates in the hopping regime, meaning at sufficient low temperature and low concentration of dopants. To identify the hopping regime in the DNPUs
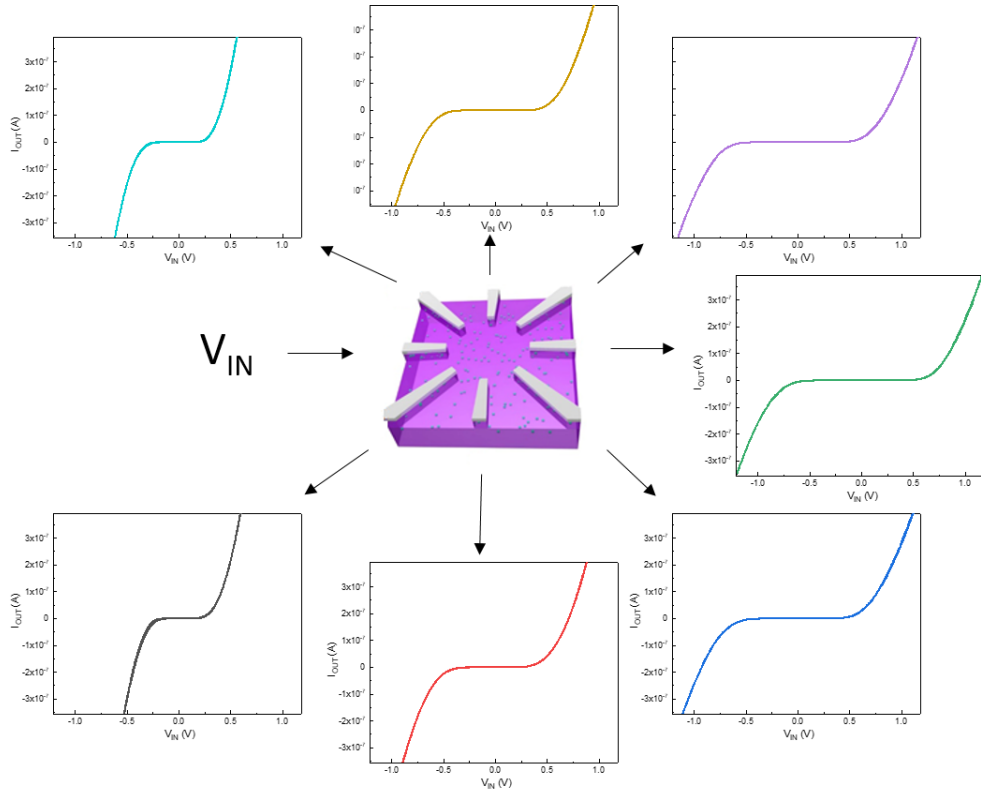
Figure 4.4: Typical non linear I-V characteristics of a DNPU at 77K. An electrode is used to apply an input voltage and the output current at the other seven electrodes is shown.

investigated in this thesis, we analyzed their electrical behaviour in different temperature regimes. I-V measurements were taken between opposite electrodes, while cooling the DNPU down to 5K or 70K. To analyze the charge transport mechanisms involved we extracted the value of the zero-bias conductance and we evaluated it as a function of the temperature. Following the study reported in Chapter 1, the conductance behavior allows to determine the dominant charge transport mechanism in the different temperature ranges. Data and analysis will be presented in the following sections, divided by dopants concentration for clarity. In the final section we will present a comparison between the different analyzed DNPUs.

Another characteristic aspect of the DNPU is the possibility to electrostatically tune the potential landscape of the dopants network. Applying the right control voltage at one or more of the electrodes, allows to tune the DNPU's response and to produce the desired output. This results in a more complex non linearity, showing for example negative differential resistance (NDR). An example is shown in figure 4.5, for both arsenic and boron dopant network. The different doping requires opposite control voltages. The presence of NDR region is fundamental to solve linearly inseparable classification problems, such as the XNOR logic gate. So NDR can be seen as a first and necessary evidence of the DNPU tunability. We investigated how NDR can be obtained and influenced by the control voltages. Also temperature plays an important role. Depending on the dopant concentration, NDR can be observed below a different temperature and evolve with it. This effect relates the presence of the NDR to the non linear nature of hopping charge transport mechanism. In the following section I will report also on the NDR's characterization.
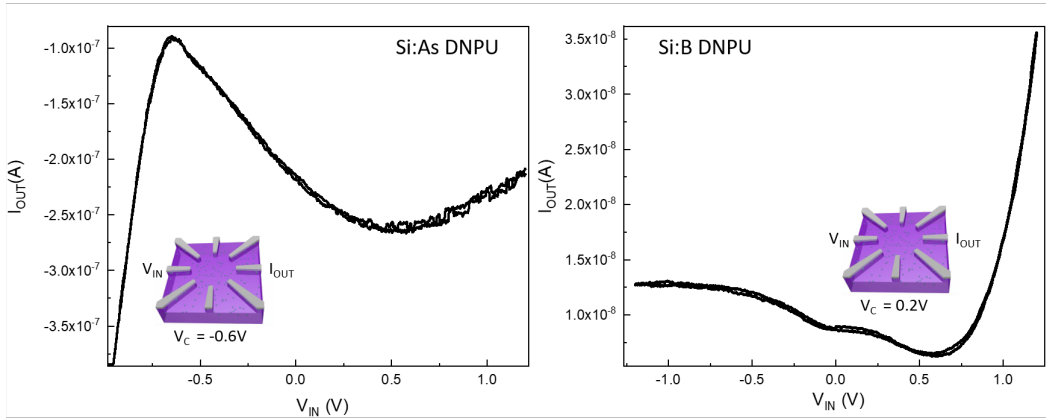
Figure 4.5: I-V characteristic of arsenic and boron DNPUs showing negative differential resistance at 77K. A schematic of the DNPU displays the role of the different electrodes.

Concentration: 4×10^{18} atoms/cm^3

The first DNPU investigated has a nominal dopant concentration at the surface of 4×10^{18} atoms/cm^3. Due to the high concentration, to analyze charge transport we need to cool the DNPU down to 5 K. In figure 4.6a, the I-Vs taken between opposite electrodes are shown as a function of the temperature. At high temperatures the DNPU has a linear response. The linearity is then progressively lost decreasing the temperature, meaning that there is a transition from band conduction regime to the hopping regime. At low temperature we found the highly resistive and non linear response expected.

Considering the zero-bias conductance as a function of the inverse temperature, the different transport regimes can be identified. The fitting of the data is reported in figure 4.6b. The conductance shows two different behaviors in two distinct temperature regimes. At high temperature we obtain an Arrhenius plot, with the logarithm of the conductance that depends linearly with the inverse of the temperature. Therefore the dominant charge transport mechanism is thermally activated. The extracted activation energy is of $(66 \pm 2)meV$, obtained fitting the data with equation 2.7. This value is consistent with the expected value for arsenic dopants in bulk silicon $(53.7meV)$ if we consider the correction due to dopants deactivation. More details will be given later in section 4.2. At lower temperature we enter in a transition region, probably characterized by nearest neighbour hopping. Below 50 K then, we enter in the variable range hopping regime. Carriers hop from an occupied dopant state to a free one. The dopant level needs to be close enough in energy and not necessarily in space, so hopping between dopants far in distance is now possible. As introduced before, variable range hopping can be described with Mott or Efros-Schlovkii models characterized by different temperature dependence of the conductance. Distinguishing between a temperature dependence that scales with the power 1/2 or 1/3 is not straightforward with experimental conductance data. Both models can indeed fit our data quite well. Fitting the data with equation 2.22, the Efros-Schlovskii temperature can be extracted. We obtain $T_{ES} \approx 1150K$. In the case of Mott VRH, we can conclude that we are observing 2D transport consistent with the geometry of the DNPU and we could extracte a $T_M = 27000K$, similar to values reported in literature for similar nanodevices [51].
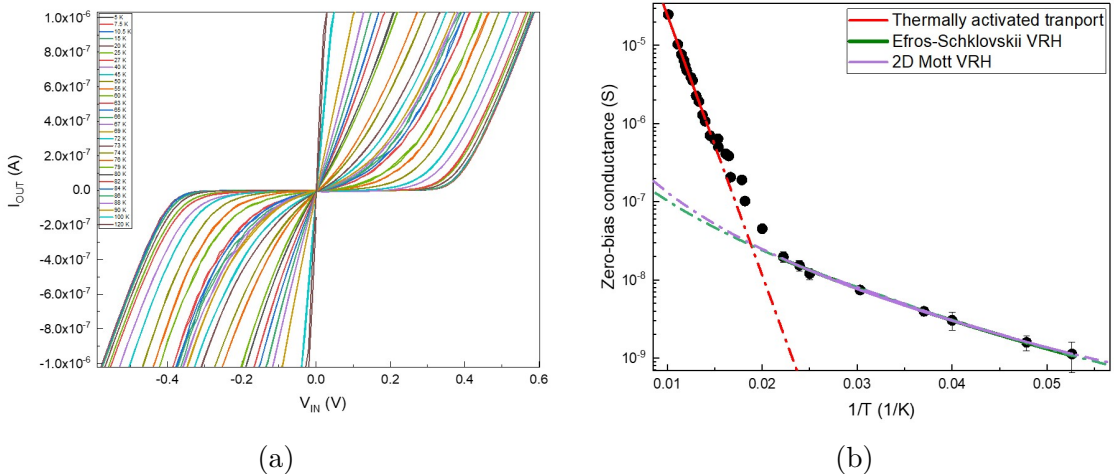
Figure 4.6: (a) I-V characteristics measured between opposite electrodes of the DNPU, varying the temperature. (b) Zero-bias conductance as a function of the inverse temperature, showing the fitting models of the different charge transport mechanisms.

For this DNPU we observe negative differential resistance in a temperature range

between 70 K and 5 K. In figure 4.7a we report the NDR obtained varying the control voltages from -0.2 V to -0.49 V, at a temperature of 5 K. The electrode next to the output is used as control electrode. This particular electrode is the one that affects most the output current. To better visualized the NDR region, the same data are reported in the 2D plot in figure 4.7b. In this way, it is easily possible to evaluate the influence of both input and control voltages. The color map refers to the derivative of the output current with respect to the input voltage (dI/dV). The blue region, where the derivative is negative, identifies the combination of input and control voltages resulting in a NDR in the output current.

Figure 4.8 shows the dependence of the NDR on the temperature. It is visible in the plots how temperature has an effect on the NDR shape and intensity. We will return to this point later, in section 4.2.

(a)   (b)
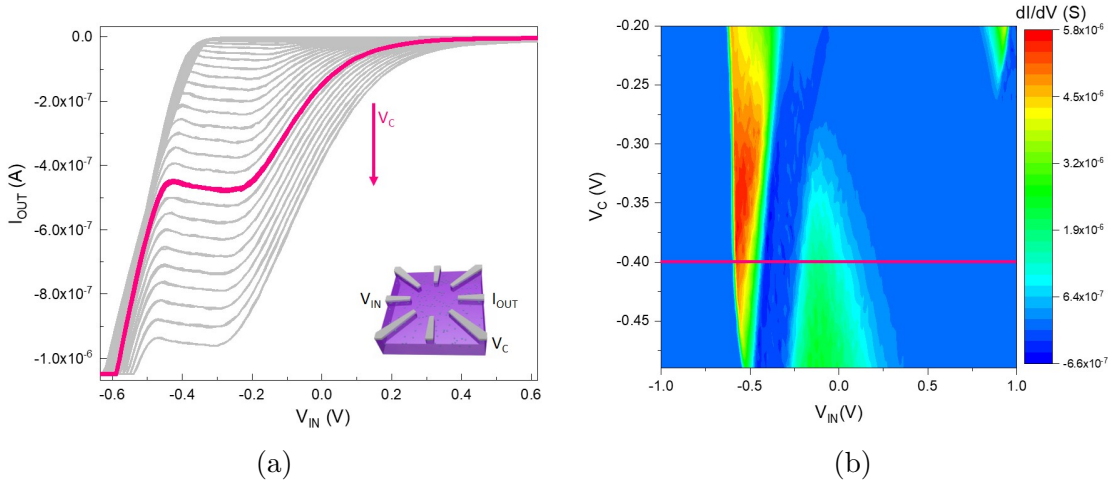
Figure 4.7: (a) I-V showing negative differential resistance, measured for different control voltages. (b) 2D colour map of the derivative of the output current with respect to the input voltage.
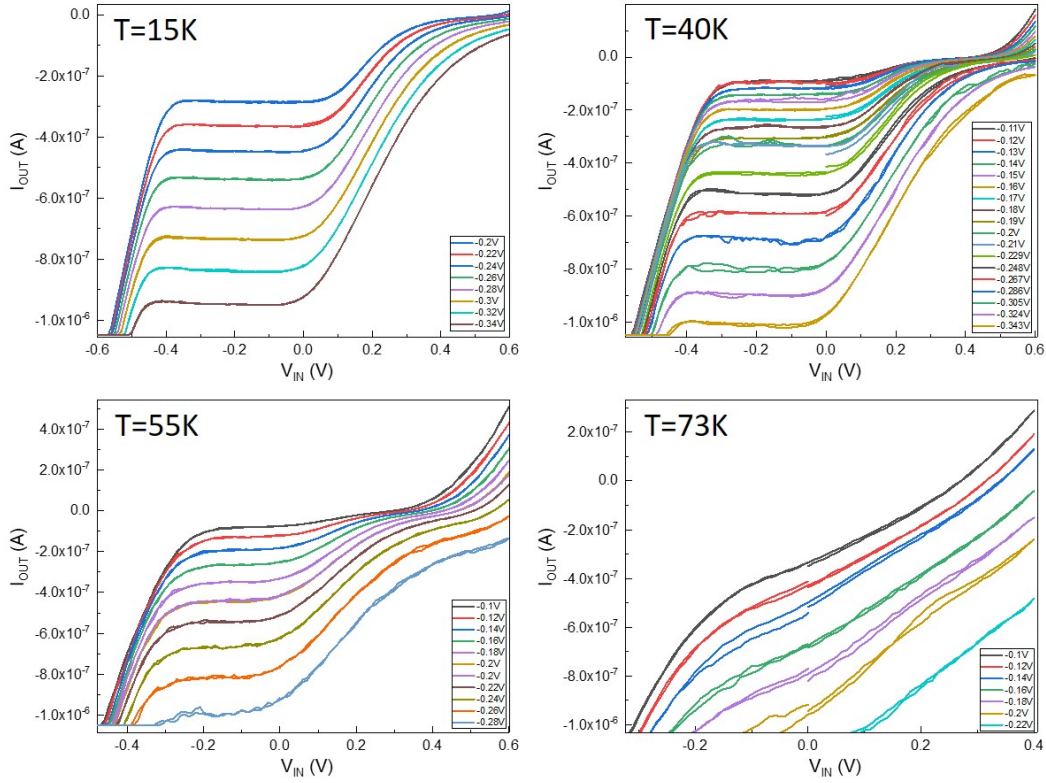
Figure 4.8: Behavior of the NDR regions varying the temperature.

Concentration: 8×10^{17} atoms/cm³

The operation temperature of the DNPU can be increased if the doping level is lower. In the DNPU with nominal arsenic concentration of 8×10^{17} cm^{-3} it is possible to enter the hopping regime at a much higher temperature compared to the previous case. In figure 4.9a the variation of the I-V characteristic is shown, varying the temperature from room temperature to 70 K. It is possible to note that even at room temperature the DNPU's response is not completely linear. Analyzing the behavior of the zero-bias conductance as a function of the inverse temperature, we can notice that band conduction is dominant for temperatures above 225K. An activation energy of 120 meV can be extracted from the fit. In this case, the extrapolated value is higher than the expected one, also considering the proper correction due to compensation and dielectric mismatch. However in nanoscale devices, there could also be an effect of dopant deactivation [56]. Dopants near the silicon surface feel a decreased dielectric screening that leads to stronger electron confinement and larger ionization energies. Also in [51], when investigating charge transport in Si:B DNPU, they found an activation energy three times larger than the value of boron in bulk silicon. Below a temperature of 120K, hopping transport becomes dominant resulting in the non-linear electrical response. Again we are

observing variable range hopping and the best describing model cannot be derived from the available data. An Efros-Schlovskii temperature of $T_{ES} \approx 1800K$ and a Mott temperature of $T_M \approx 24000K$ can be extrapolated. The low conductivity
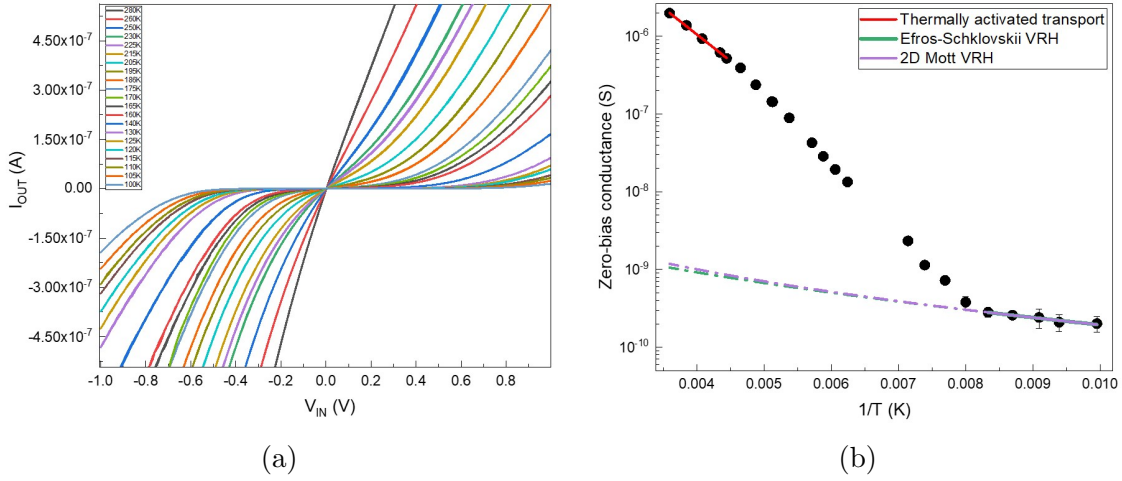
Figure 4.9: (a) I-V characteristics measured between opposite electrodes of the DNPU, varying the temperature. (b) Zero-bias conductance as a function of the inverse temperature, showing the fitting models of the different charge transport mechanisms.
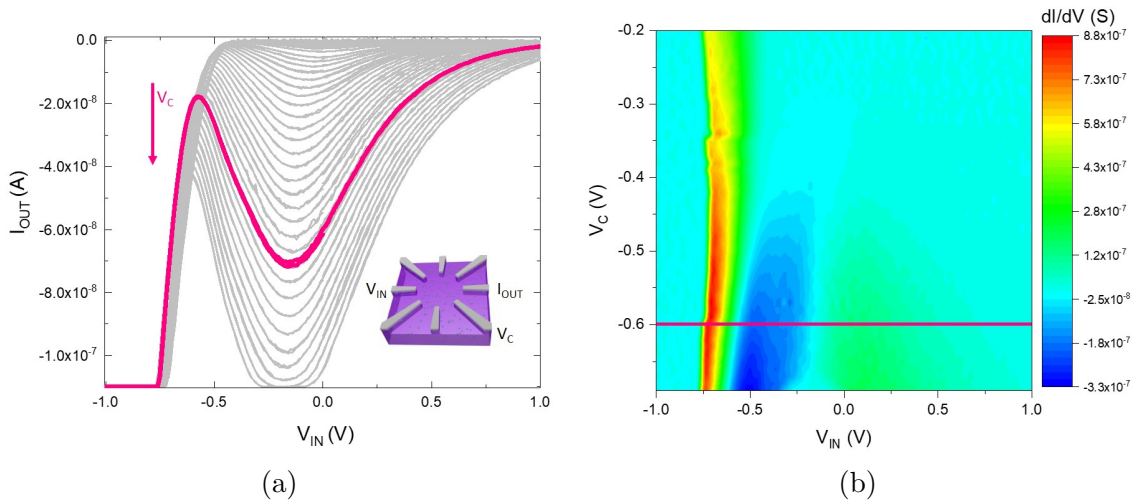
Figure 4.10: (a) I-V showing negative differential resistance, measured for different control voltages. (b) 2D colour map of the derivative of the output current with respect to the input voltage.

of this DNPU makes the NDR more visible. Figure 4.10a shows how the NDR is more pronounced increasing the negative value of the control voltage from 0 V to -0.7 V. Considering the 2D plot on the right, the blue region, where the derivative is negative, spans a range of different input and control voltages. To better understand the mechanism causing negative differential resistance, we analyzed the currents flowing in the dopant network. Let us consider the three electrodes configuration

presented in figure 4.11a. A voltage sweep is applied to one electrode (input, red), the opposite electrode is grounded (output, blue) and a third electrode in the middle (control, black) is used to apply a control voltage of $V_C = -0.65V$. The current is measured simultaneously at the three electrodes. The output current, as we expected, shows a complex non linear behaviour with a partial NDR. In the figure we reported also the input current and the output current characterized by different non linearity. Adding the contribution of input and control currents, we obtain the I-V characteristic (purple) shown in figure 4.11b. The output current is also reported in the same plot, to emphasize the similarity. Despite a small offset, probably due to the measurement settings, the measured output current is given by the superposition of currents coming from the input and control electrode. The small discrepancy between the two curves is due to current leaking in the DNPU's substrate, as it will be clear later in section 4.3 (figure 4.19b). We can therefore conclude that the complex behavior measured at the DNPU's output is due to the current contribution of all the electrodes involved. This means that when evolving the DNPU, the control voltages define a potential landscape of the dopant network that results in different current flows: carriers will move in this potential following the allowed paths. The superposition of all the contributions will result in the output current. The presence of the NDR, or more generally complex output behavior, is intrinsically related to the non linearity. The NDR temperature dependence can prove it, we will now see in detail. The same three electrodes configuration is employed, with a fixed voltage of -0.4 V applied to the control voltage. The resulting NDR is shown in figure 4.12a, where the temperature is increased from 70 K to 255 K. Above this last temperature, NDR is no more detectable. As suggested before, this temperature range corresponds to a network response that is 'enough' non linear. Above this temperature the I-V becomes almost linear, therefore is not possible anymore to observe a modification in the output current. To evaluate the variation of the NDR in a more quantitative way, the normalized peak-to-valley current ratio has been calculated and reported in the plot on the right. In the inset the peak/valley are defined as the highest/lowest current level reached. The ratio is then calculated dividing the delta current between peak and valley by the corresponding variation of input voltage. The goal of such normalization is to consider also the temperature dependence of the input voltages at which the NDR is induced. The highest this ratio is, the more pronounced the NDR is. Note that in our case we are dealing with negative currents, therefore the resulting peak-to-valley current ratio is negative. Then, the absolute value is considered. In the plot (4.12b) is visible how the ratio increases with temperature, up to a certain range between 150 K and 200 K. Then the ratio starts to decrease and finally goes to zero above 255 K, where there's no measurable NDR. We can conclude that for a given control voltage, there exists a

temperature range that maximizes the peak-to-valley current ratio and therefore the tunability of the DNPU.
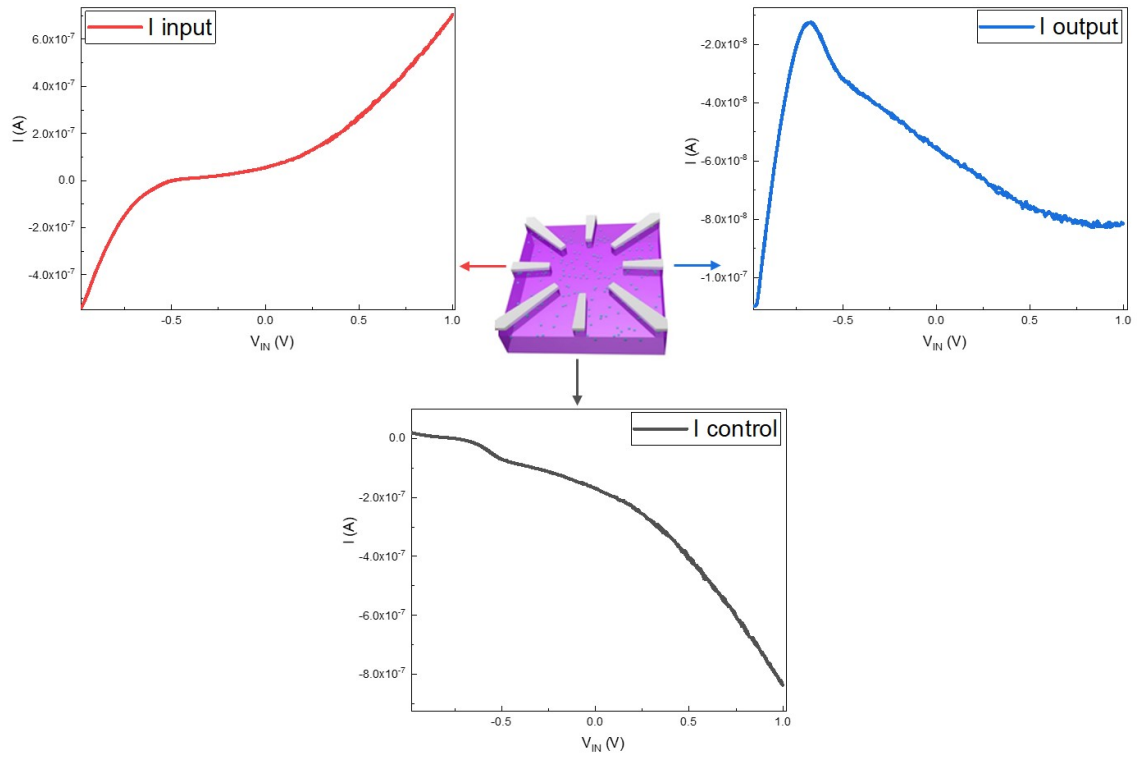
(a)
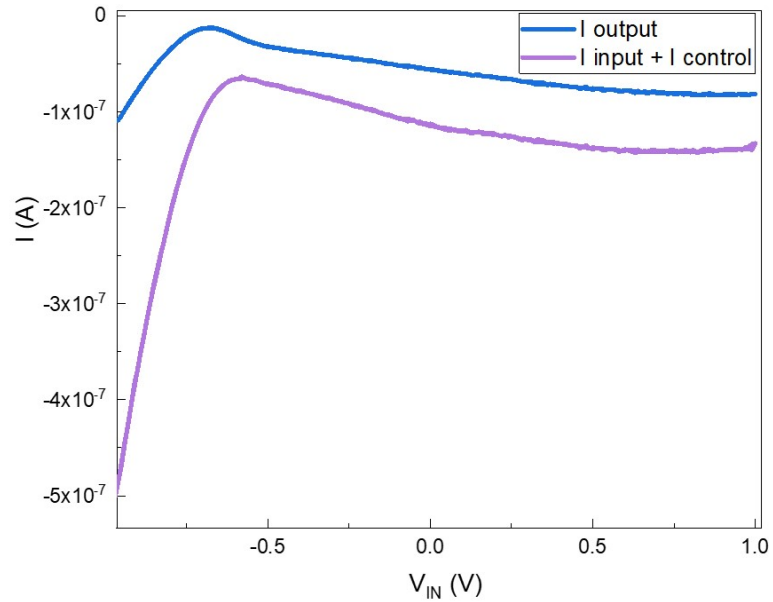
(b)

Figure 4.11: Current analysis performed at 80 K, with a control voltage of -0.65 V: (a) measured currents at the input, control and output electrode, (b) comparison between the output current and the superposition of input and control current.

(a)

(b)
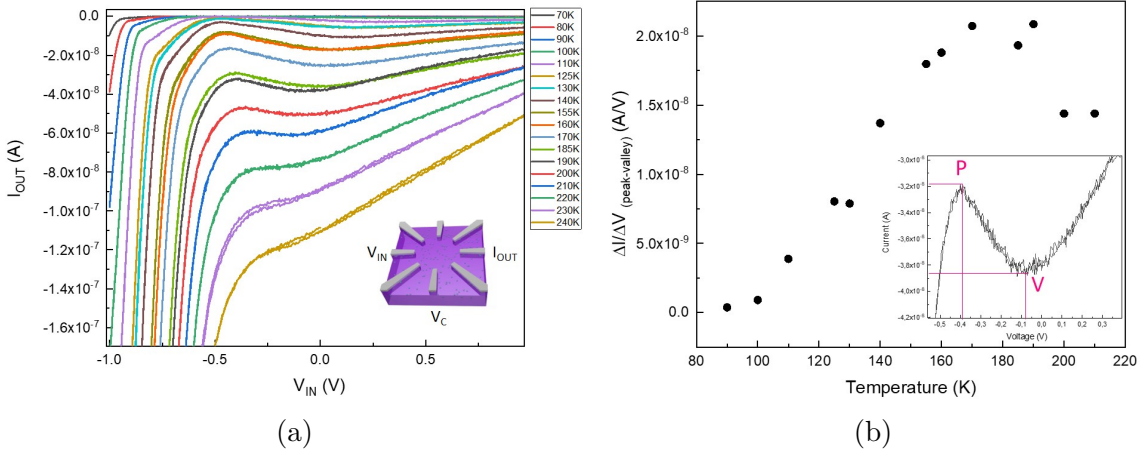
Figure 4.12: (a) Temperature dependence of the I-V characteristics showing NDR. The DNPU's electrode configuration is also shown. (b) Peak-to-valley current ratio as a function of temperature, showing a maximum.

Concentration: 2×10^{18} atoms/cm^3

This intermediate concentration is the typical one used to perform computational tasks with the DNPU. These DNPUs in fact operate conveniently in liquid nitrogen, with results published in [51]. In Figure 4.13a, the I-V characteristics of the DNPU are shown, varying the temperature from room temperature to 6 K. Decreasing the temperature the response is more and more resistive and non linear.

Also in this case we analyzed the behavior of the conductance as a function of the inverse temperature. The zero-bias conductance is presented in figure 4.13b. A thermally activated charge transport mechanism is found to be dominant for temperatures above 240 K. The inset shows the detail of the resulting Arrhenius plot, with the conductance that depends linearly on the inverse temperature. The extracted activation energy is of (77 ± 2) meV. Below a temperature of approximately 110 K, the temperature dependence changes. The DNPU is now operating in the hopping regime. Variable range hopping is the dominant transport mechanism. Again, both Efros-Schlovskii and 2D Mott models can describe the available experimental data. It is possible to extract a $T_{ES} \approx 1600K$ and a $T_M \approx 21000K$. The DNPU response shows negative differential resistance region for negative control voltages, as we can see in figure 4.14a[1]. As before the 2D plot, 4.14b, makes it easier to identify the combination of input and control voltages that results in the NDR.

---

[1]These measurements were performed in the switch setup at the University of Twente.
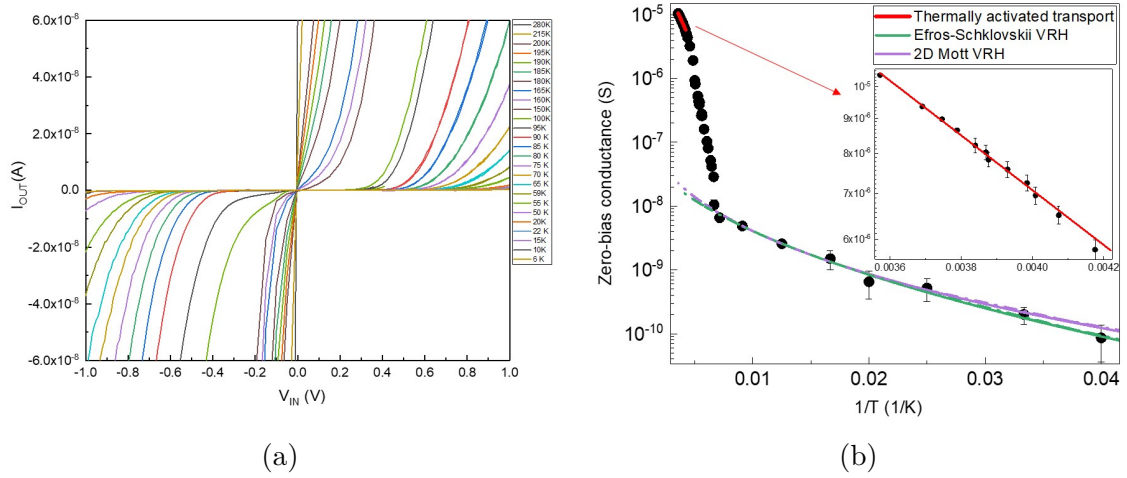
Figure 4.13: (a) I-V characteristics measured between opposite electrodes of the DNPU, varying the temperature. (b) Zero-bias conductance as a function of the inverse temperature, showing the fitting models of the different charge transport mechanisms.
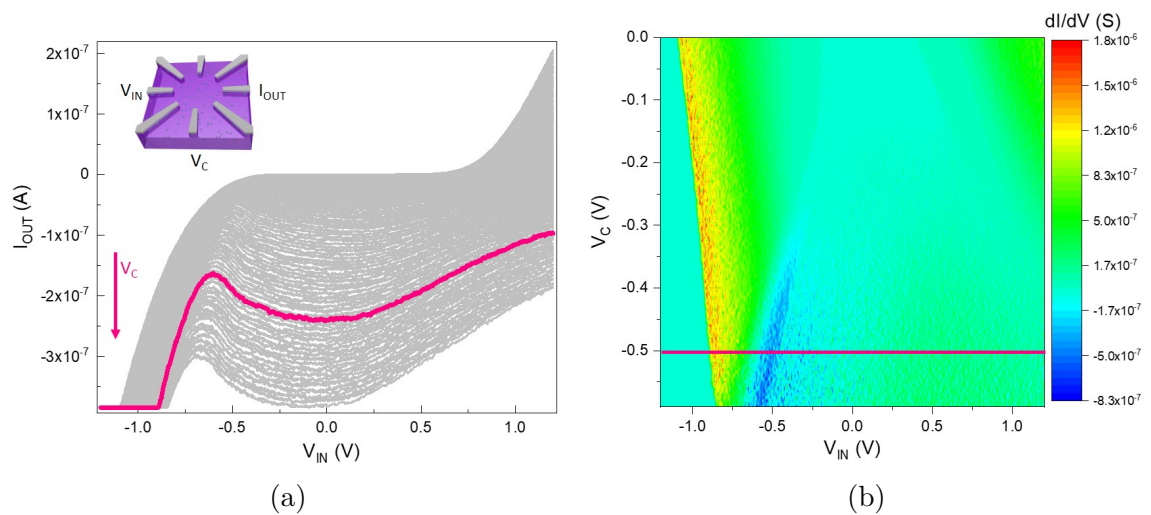
Figure 4.14: (a) I-V showing negative differential resistance, measured for different control voltages. (b) 2D colour map of the derivative of the output current with respect to the input voltage.

Comparison

In this section we report a comparison between the extracted values of activation energy, Mott temperature and Efros-Schlovskii temperature for the three analyzed DNPUs. All the parameters are reported in table 4.1 and the indicated errors are extracted from the fit. We already mentioned that the activation energies extracted

Dopants concentration $(atoms/cm^3)$	Activation energy (meV)	$T_{Efros-Schlovskii}$ (K)	T_{Mott} (K)
4×10^{18}	66 ± 2	1250 ± 70	$(27 \pm 2) \times 10^3$
2×10^{18}	77 ± 2	1600 ± 50	$(21 \pm 2) \times 10^3$
8×10^{17}	120 ± 2	1800 ± 300	$(24 \pm 7) \times 10^3$

Table 4.1: Summary of the extracted values of activation energy, Efros-Schlovskii and Mott temperature for the three analyzed DNPUs.

from the experimental data are higher than the reference value for arsenic dopants in bulk silicon ($E_{dop,0} = 53.7 \ meV$). This discrepancy seems to increase, lowering the concentration of dopants. Following the theoretical discussion of Chapter 2, it is possible to make some corrections to these values, considering the dopants concentration, the dielectric mismatch with the native oxide on top of the DNPU and the silicon dielectric anomaly. First of all, compensation needs to be considered, that is expressed in equation 2.1 from the ratio N_{dop}/N_{ref}. This correction actually reduces E_{dop}, moving the center of the dopant band closer to the conduction band. The opposite effect is due to the decreased dielectric screening seen by dopants close to the Si/SiO_2 interface. This results in a further correction expressed in equation 2.4, that is proportional to the dielectric mismatch and to the distance z from the interface. In the same equation we applied a correction to the silicon dielectric constant, calculated with equation 2.5. This last correction considers that at dopant concentration close to the critical one, the silicon dielectric constant diverges. This correction is important in our case considering the high arsenic concentration, as highlighted in figure 2.3. The result of these corrections is shown in figure 4.15, where the activation energy is plotted as a function of z in nm, for the three different dopants concentrations. It is clear that the activation energy diverges when dopant atoms at the surface are considered ($z < 1 \ nm$). In the case of the DNPUs it is reasonable to believe that transport takes place mainly between dopant atoms closer to the device surface, due to the device structure and to the doping profile. At higher distance from the interface, the dielectric mismatch becomes less important and the activation energy tends to the value of the calculated E_{dop}. The colored bands in the plot indicate the experimental activation energies for the different DNPUs considered the error bars, and the corresponding calculated z. The

extracted values of z for the three different concentrations present a small variation, we believe it is reasonable to consider the average value with its standard deviation. The activation energies are in fact extracted from experimental data with associated uncertainty, and the calculated corrections (equations: 2.1, 2.4, 2.5) are also empirical. We therefore conclude that the donors that participate in the activated charge transport are located at a distance of (0.6 ± 0.2) nm from the device surface, that corresponds to only few atomic layers. Table 4.1 also reports the extracted value of
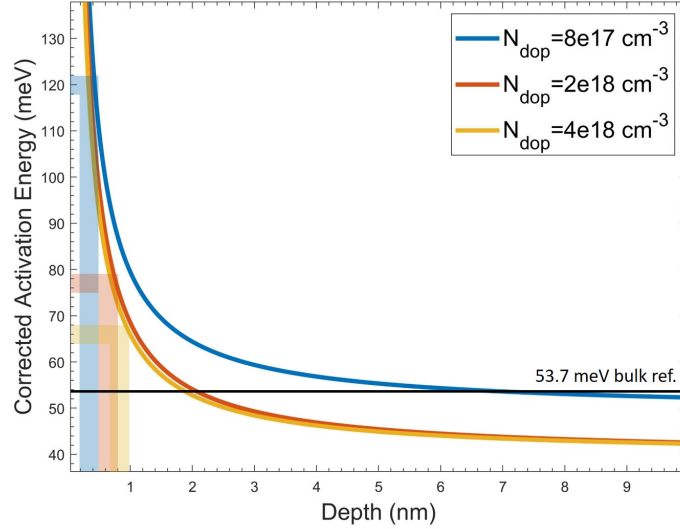
Figure 4.15: Calculated activation energy correction due to dielectric mismatch and dielectric anomaly, as a function of the distance (z) from the interface. The value or $E_{dop,0}$ is also shown as reference.

T_{ES} and T_M. The conductance fitting at these low temperatures is more delicate. First of all, lowering the temperature the DNPUs become more and more resistive. The conductance at low electric field approaches zero and its determination from the experimental data comes with some uncertainty. Secondly, but not less crucial, the two variable range hopping models have a similar temperature dependence. Distinguishing between the power 1/2, for Efros-Schlovskii, and 1/3 for Mott VRH is not always straightforward. It was at least possible to exclude a three dimensional Mott variable range hopping, characterized by a temperature dependence that scales with the power of 1/4. We can therefore confirm a two-dimensional hoping mechanism, as observed in B-doped DNPUs [51]. The extracted Mott temperatures are similar to the values reported in literature in the case of two dimensional variable range hopping [90].

The Efros-Schlovskii temperature (T_{ES}) can be calculated as follow [66]:

$$T_{ES} = \frac{2.8e^2}{4\pi\epsilon\epsilon_0 k_B \xi}, \quad \xi = \xi_0 \left(1 - \frac{N_{dop}}{N_{ref}}\right)^{-1/2}, \quad \xi_0 = \frac{e^2}{8\pi\epsilon_0 \epsilon E_{dop}} \tag{4.1}$$

where ξ is the localization length, that can be estimated from the number of dopants (N_{dop}), and ξ_0 is the effective Bohr radius calculated from the energy position of the dopants level (E_{dop}, eq. 2.1). The other values are constants: e is the electron charge, ϵ_0 and ϵ are the vacuum and silicon dielectric constants and N_{ref} for arsenic dopants can be found in table 2.1. Also in the estimation of the Efros-Schlovskii temperature we consider the corrections due to the high doping level and consequent dielectric anomaly (eq 2.5). The calculated values are $T_{ES} = 1270\ K$, $T_{ES} = 1842\ K$, $T_{ES} = 2197\ K$, for decreasing concentration of dopants in our DNPUs. These calculated temperature are consistent with the values extracted from the data fitting considering the experimental errors.

4.3 Photocurrent and Magnetic Field

In this section we will report the study on the DNPU photoconductivity. The response of the different DNPUs is analyzed under photoexcitation with different wavelengths, red ($\lambda = 632\ nm$) and blue ($\lambda = 450\ nm$). Moreover, we will show the influence of an external magnetic field on the DNPU's photocurrent. This characterization will be helpful in understanding the conditions in which EDMR measurements are performed (section 4.5).

Concentration: 4×10^{18} atoms/cm^3

The characterization of this DNPU photoconductivity is performed at 10 K, in order to have the same condition in which we performed EDMR measurements.
The simplest configuration with only two electrodes is initially considered. The I-V between opposite electrodes is shown in the inset in figure 4.16. As we expected at this very low temperature the DNPU response is highly resistive and non linear. When the device is put under illumination, an increased conductivity is measured. In the figure below, the photocurrent due to a red and a blue light source is shown. Both these energies, respectively 1.96 eV and 2.76 eV, are above the silicon energy gap that is of 1.12 eV. Electron-hole couples are therefore photogenerated in the conduction/valence band, resulting in contribution in the transport. Moreover, dopants can be photo-ionized. We noticed then, that the presence of a static magnetic field
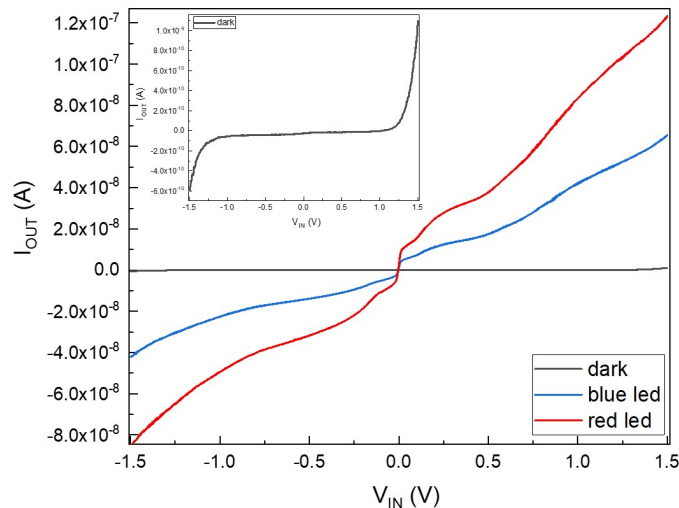
Figure 4.16: Photocurrent measured with a red and a blue light source. The reference I-V in dark is shown in the inset.

has an impact on the photoconductivity, reducing it. The reduction effect increases

(a)   (b)

Figure 4.17: Photocurrent reduction due to the static magnetic field: (a) red light source, (b) blue light source.

with higher magnetic field. The same effect is visible using both red and blue light, as shown in figure 4.17. An higher variation between dark and photocurrent is obtained with the red illumination. An increase of about two orders of magnitude is measured. Since this is important for increasing the EMDR signals, we will mainly show the result using the red light source. Also the effect of the magnetic field seems higher in this case. Considering now a configuration with three electrodes we can induce part of a negative differential resistance, even at this very low temperature. Again, we employed the input voltage - control voltage plot introduced in the previous section, to better visualize the NDR. In figure 4.18 three configurations are presented:

a) NDR for different control voltages at 10 K in dark and relative 2D plot. At this low temperature only part of the NDR is visible. Scanning a larger range of potential, it should be possible to measure again an increase in current. We avoid higher voltages in order to not damage the device.

b) I-V characteristics obtained under illumination with a red led. The NDR in the photocurrent is modified. Multiple bumps in the I-V characteristics are now visible, meaning that illumination results in a more complex DNPU electrical response.

c) Photoconductivity is also in this case reduced by the presence of a static magnetic field. Also the NDR is affected and it is now limited to a small region of input and control voltages.

Finally the influence of the substrate polarization is studied, that will be useful in the EDMR measurements presented later in section 4.5. I-V measurements were taken between two opposite electrodes, while applying a back gate voltage to the substrate.

(a)

(b)

(c)
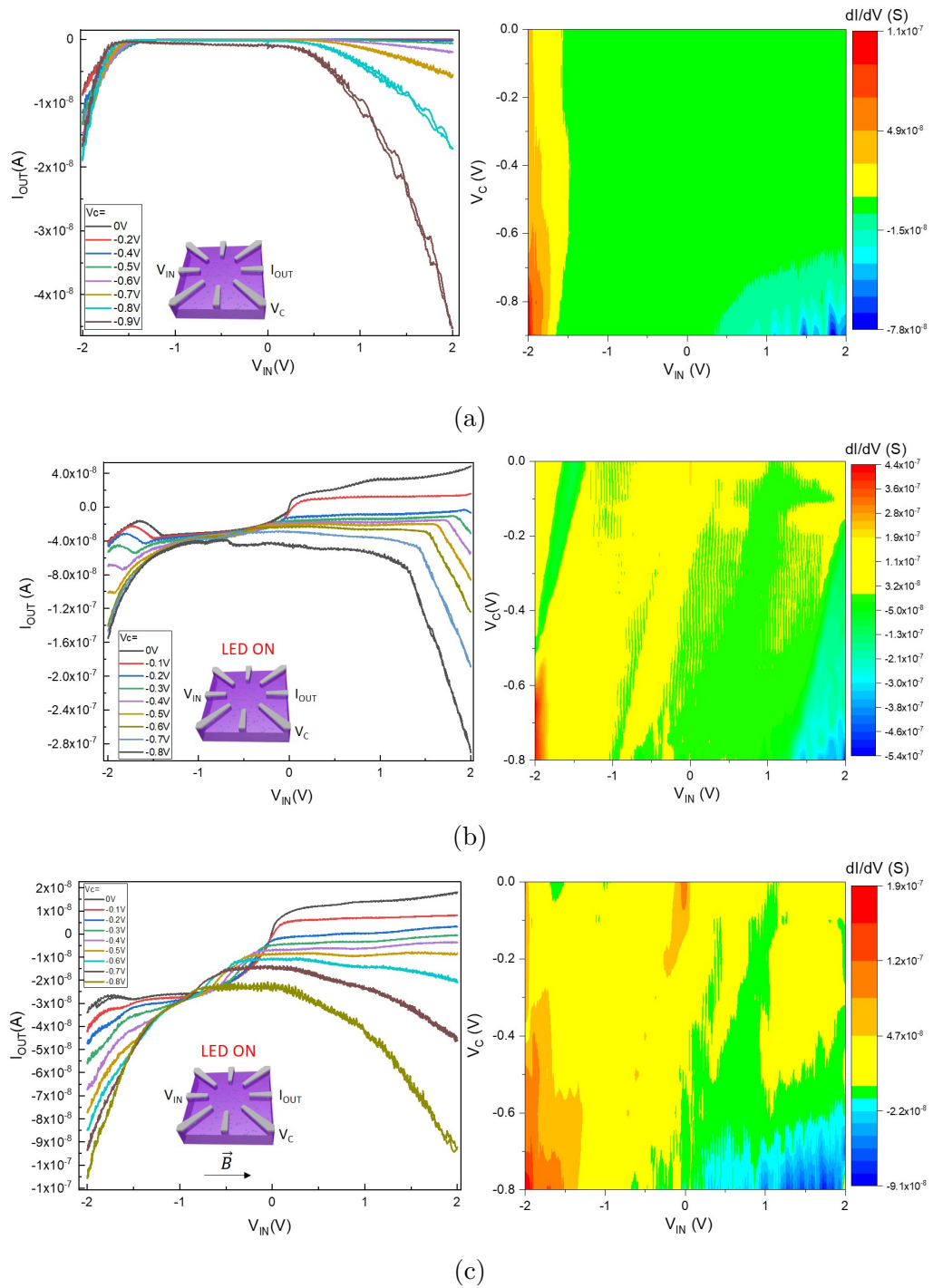
Figure 4.18: NDR for different control voltages at 10 K and relative 2D plots: (a) current in dark, (b) photocurrent, (c) photocurrent with an applied static magnetic field of 335 mT. The insets show the electrodes configuration.

A great variation of the I-V behavior is obtained for $|V_{back}| > 1V$, resulting in the S-shape I-V shown for example in figure 4.19. We report here the analysis of the currents involved. The resulting output is plotted in blue, while the current measured at the input and at the back are in red and black respectively (4.19a). All the currents are measured simultaneously while a voltage sweep is performed at the input electrode, a constant bias of -5V is applied to the substrate and the output electrode is grounded. In figure 4.19b we show the comparison between the measured output current and the superposition of input and back current. In this case, we found a perfect match between the two currents characteristics. We can confirm that the DNPU electrical behaviour is the result of all the current contributions across the dopant network, also considering the substrate in this case. Figure 4.20 reports the behavior of the I-V characteristic for different voltages applied to the substrate, while the DNPU is kept in dark at 10 K. Repeating the measurements while the DNPU is under illumination results in a photocurrent up to four orders of magnitude higher than the dark current. The photocurrent is then reduced by a factor 10, when a static magnetic field of 335 mT is applied. The resulting I-V curves, measured under illumination and with an applied magnetic field, are presented in figure 4.20b. Some examples for different applied back voltages are reported separately in figure 4.21. The black curve refers to the measurement in dark, the red curve to the photocurrent, and the blue one is the I-V measured with the DNPU under illumination and in the presence of a magnetic field of 335 mT. In these examples, the change in conductivity is better visible. Note that the current values are negative, therefore the increase/decrease in conductivity is meant in absolute value. It is also possible to see some photo-induced NDR regions, especially in 4.21c. These NDR are then beveled by the magnetic field. We do not show the current analysis here, but also in these cases the output current is given by the superposition of currents from the input electrode and the substrate.
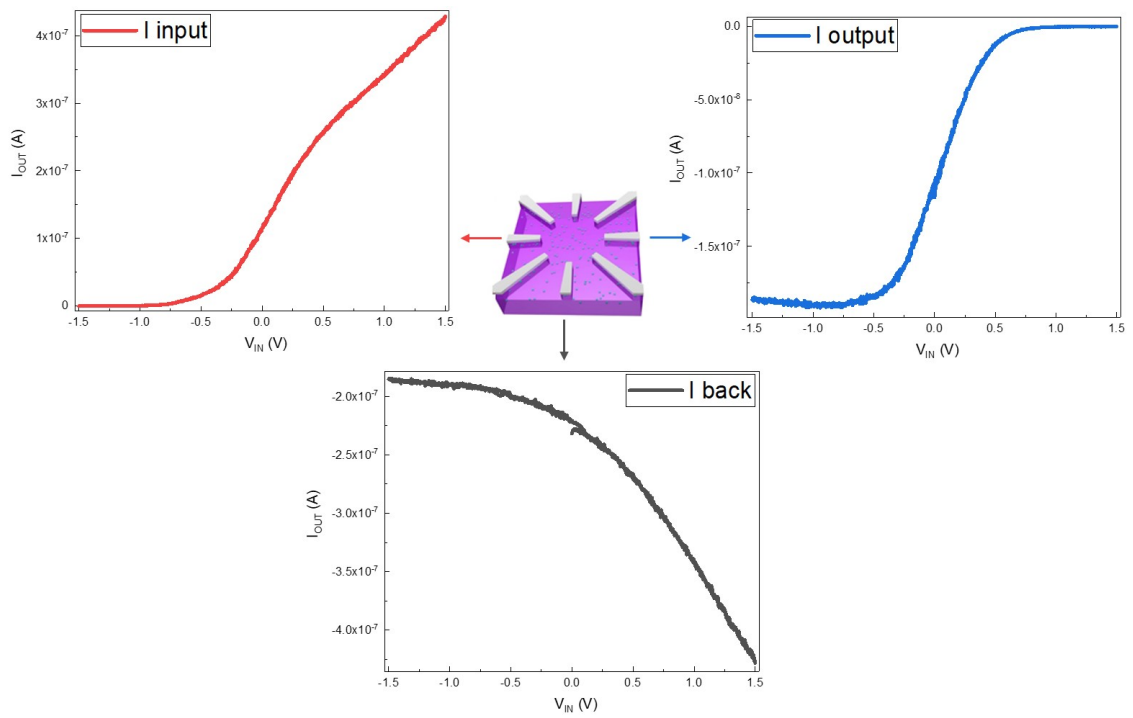
(a)
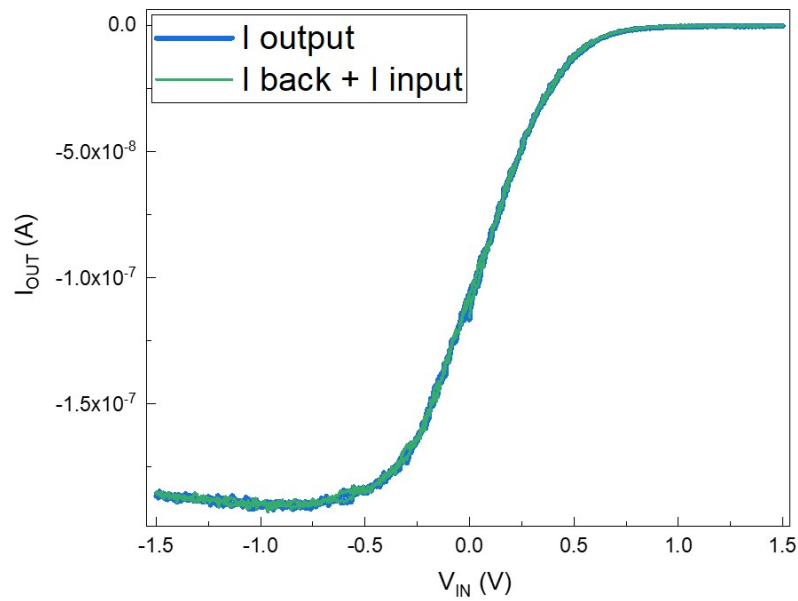
(b)

Figure 4.19: Current analysis performed at 10K, with a back voltage of -5V: (a) measured currents at the input, back and output electrode, (b) comparison between the output current and the superposition of input and back current.
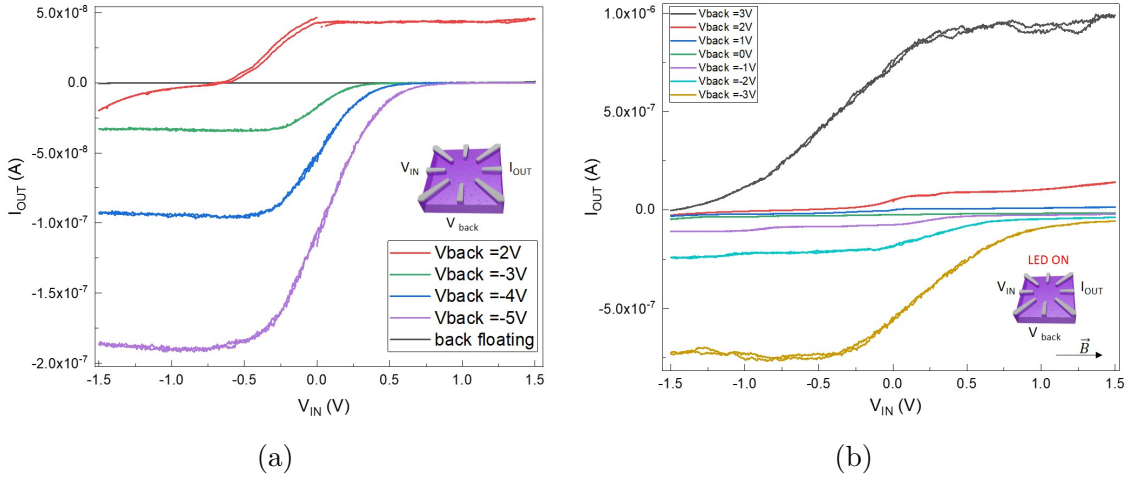
Figure 4.20: (a) I-V characteristics for different back gate voltages (V_{back}) at 10K. (b) Photocurrent with an applied static magnetic field of 335 mT for different back gate voltages.
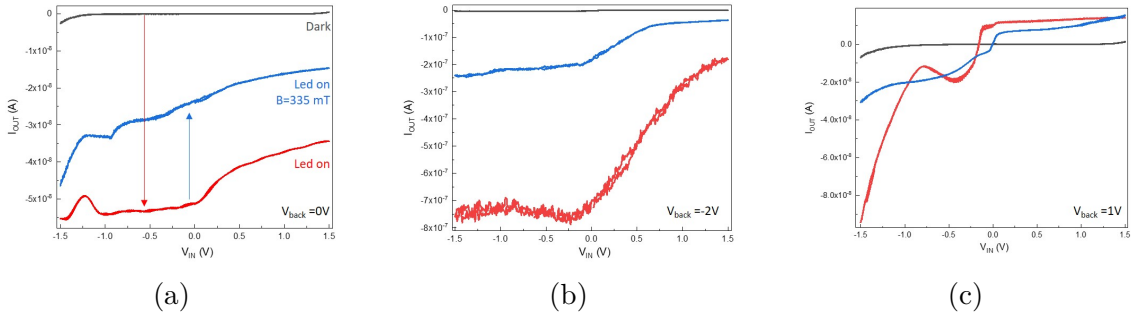
Figure 4.21: Some examples of how the electrical response (black curve) is modified by photoexcitation (red curve) and magnetic field (blue curve), for different back gate voltages: (a) $V_{back} = 0 \ V$ (b) $V_{back} = -2 \ V$ (c) $V_{back} = 1 \ V$.

Concentration: 2×10^{18} atoms/cm^3

The same characterization is performed on the DNPU with intermediate arsenic concentration, always at 10 K. The same behaviour has been detected and we report here only some examples. Figure 4.22 shows the I-V characteristics in a two electrodes configuration. The dark current is presented in the inset. An increase in conductivity of about two orders of magnitude is measured when the DNPU is analyzed under illumination with a red light source. The blue curve then, represents the photocurrent when an applied magnetic field of 335 mT. Also in this DNPU it is possible to measure a conductivity reduction that scales with the magnitude of the magnetic field.

A three electrodes configuration is also studied. The current is measured between opposite electrodes while the substrate is polarized. We found the same behavior of the previous DNPU, with 'S-shape' I-V characteristics. Furthermore, also in this case we could detect some photo-induced NDR region or at least some pecu-
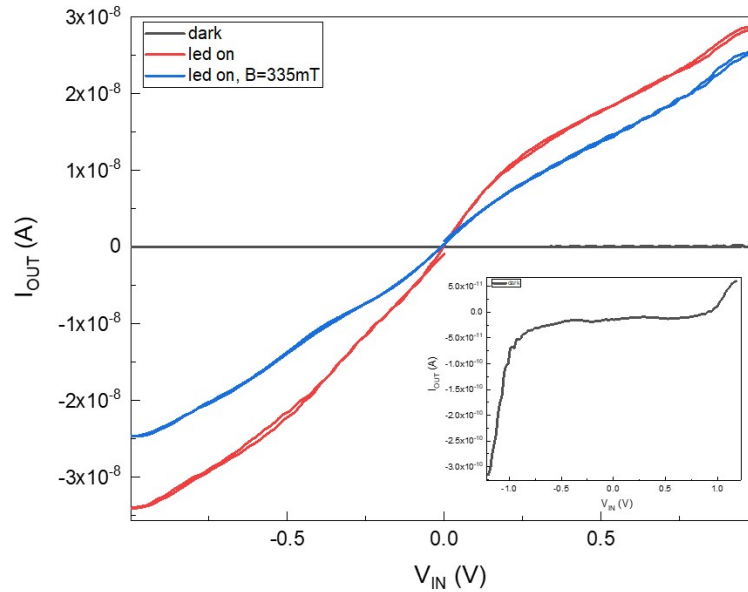
Figure 4.22: Variation of the I-V curves when the DNPU is measured at 10 K, under illumination and with an applied static magnetic field. The inset shows an enlargement of the dark current.

liar bumps in the photocurrent. An example is shown in figure 4.23 for an applied voltage to the device's back of $V_{back} = 1.5\ V$.

Discussion

We showed in this section the DNPU's behaviour in response to external stimuli. In particular the effect of photoexcitation was investigated, together with the application of a static magnetic field. In both the analyzed DNPU The same photocurrent behaviour has been observed in both the analyzed DNPUs. A decrease in photoconductivity is observed when a static magnetic field is applied in non resonant condition. The magnitude of this effect is proportional to the magnetic field and even effects due to small fields can be detected. Few similar examples are reported in literature [91][92]. This phenomenon can be explained by a non resonant spin dependent recombination, using the Kaplan-Solomon-Mott spin pairs model [79][93][94]. Illumination causes the photogeneration of electrons and holes pairs. Recombination is then only possible if *e-h* pair is formed in the singlet state. The application of a magnetic field can produce a mixing of the singlet and triplet pairs, and consequent change in the recombination rate. In our case, an increase in the recombination rate is observed, since the photocurrent is reduced.
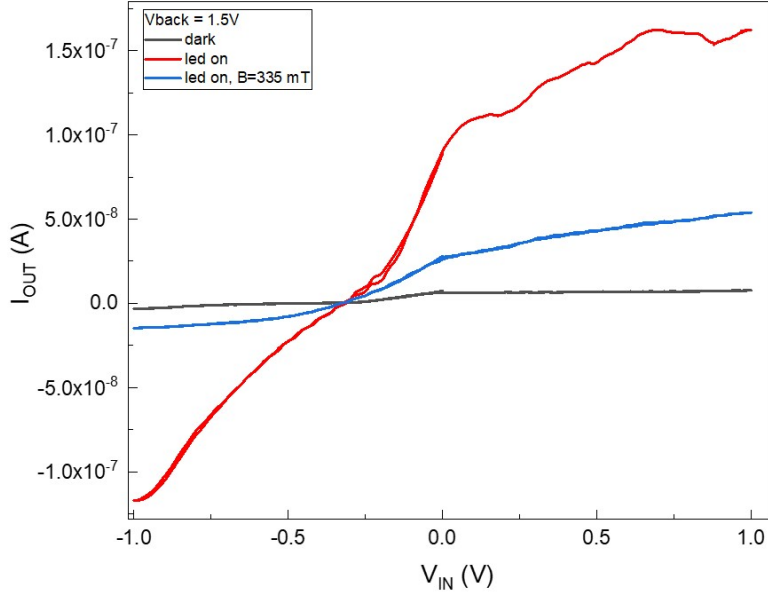
Figure 4.23: Example of an I-V characteristic measured at 10K with a back gate voltage $V_{back} = 1.5\ V$, in dark, under illumination and with an applied static magnetic field.

4.4 Top-Bottom Configuration

An electrical characterization of the top-bottom configuration is here presented. Data shown in the previous section reveals the importance of the substrate, which can be accessed through the back gate. In this section, we will show the DNPU's electrical behavior when investigated in a vertical configuration. One of the eight electrodes is used as input, while the output current is measured at the substrate. In such a way, we are investigating a sort of n^+p junction. The n^+ is due to the arsenic doping, while the p component is the B-doped silicon substrate. It is important to recall that we are not dealing with a common sharp junction. The arsenic concentration follows in fact a doping profile. Moreover, the electrodes at the sample's top may have an influence on currents movement, even if they are kept floating. Figure 4.24 shows the I-V measurements taken at room temperature in a vertical configuration. Different nominal dopant concentrations at the surface of the DNPU are compared. It is possible to note that the measured I-V characteristics do not show the expected diode behavior, especially at high dopant concentrations. Moreover, a high reverse current is detected and it increases with the arsenic concentration. The light doped DNPU is the one that most approaches the I-V characteristic of a $p - n$ junction, even if the leakage current remains high. Its behavior is highlighted in the figure's inset.

67
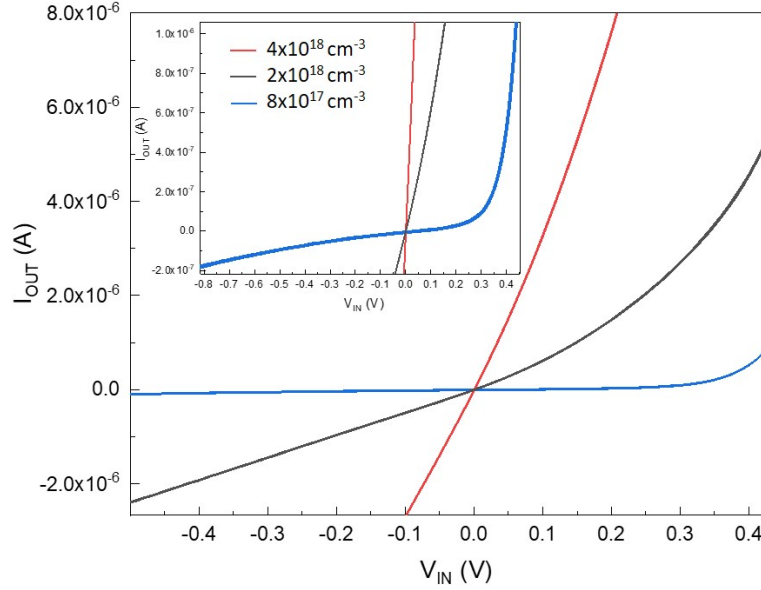
Figure 4.24: I-Vs measurements in a top-bottom configuration for the three analyzed DNPUs. V_{IN} is applied to the p-doped substrate.

Concentration: 4×10^{18} atoms/cm^3

I-V measurements taken at 10 K, between an electrode on the top of the DNPU and the back gate are shown in figure 4.25a. Also in these measurements we can confirm the behavior of the photocurrent, that is strongly reduced in presence of an external magnetic field. In this configuration, however, the magnetic field is perpendicular to the current direction maximising the Hall effect. The inset in the figure shows an enlargement, in a voltage range in which all the I-Vs seem to change behavior. At negative voltages, there seems to be an additional contribution that modifies the output current behavior. This effect is visible in all the DNPUs investigated. Figure 4.25b shows a comparison between low temperature and room temperature top-bottom I-Vs.

Concentration: 2×10^{18} atoms/cm^3

The same top-bottom I-Vs measurements are performed for the DNPU with intermediate dopants concentration. The same considerations can be made in this case. The photocurrent shown in figure 4.26a is strongly asymmetric with respect to the input voltage and it is strongly reduced by the magnetic field. The same 'kneel' in the dark current is present here at $V_{IN} \approx -1.5V$. A comparison between room and low temperature top-bottom I-Vs curve is shown in figure 4.26b, characterized as expected from a strong conduction reduction.

(a)

(b)
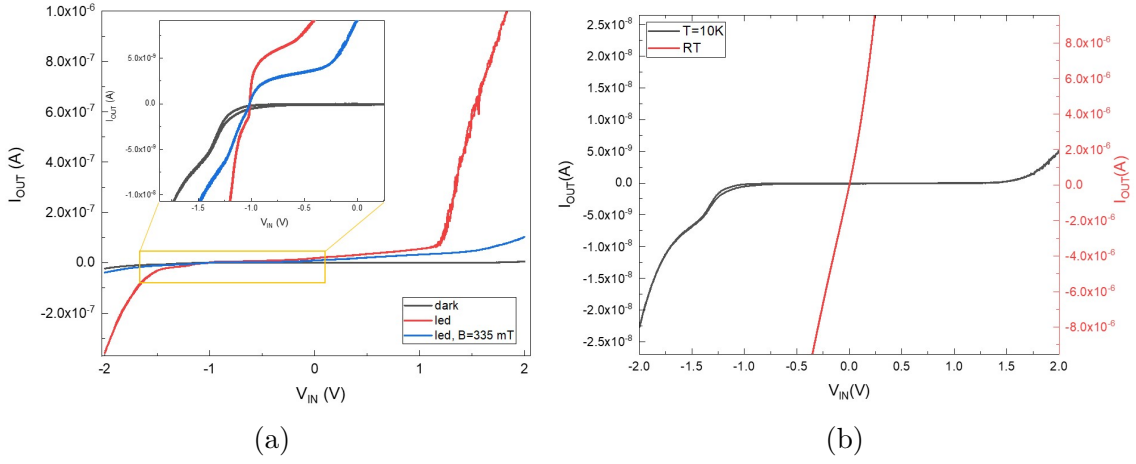
Figure 4.25: Arsenic concentration 4×10^{18} atoms/cm^3: (a) I-V measured in a vertical configuration at 10 K, in dark, under illumination and with an applied static magnetic field. V_{IN} is applied to the top electrode. (b) Comparison between the top-bottom I-V characteristic at room temperature and at 10 K.

(a)

(b)
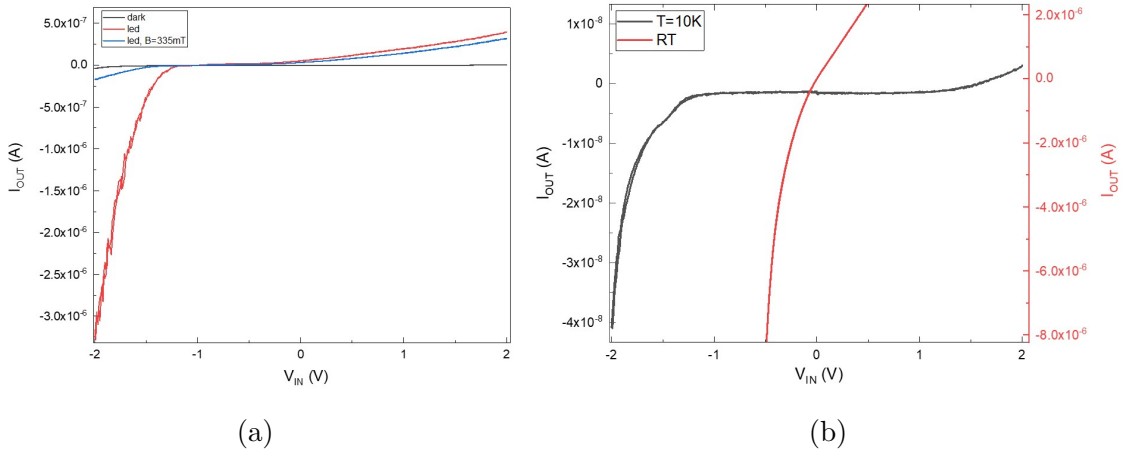
Figure 4.26: Arsenic concentration 2×10^{18} atoms/cm^3: (a) I-V measured in a vertical configuration at 10 K, in dark, under illumination and with an applied static magnetic field. V_{IN} is applied to the top electrode. (b) Comparison between the top-bottom I-V characteristic at room temperature and at 10 K.

Concentration: 8×10^{17} atoms/cm^3

Finally, the same experiments are performed on the least doped DNPU. I-Vs measurements taken at low temperature are shown in figure 4.27a. The same asymmetry and behavior of the photocurrent are measured here. The comparison of the dark current measured at low and at room temperature is displayed in figure 4.27b.
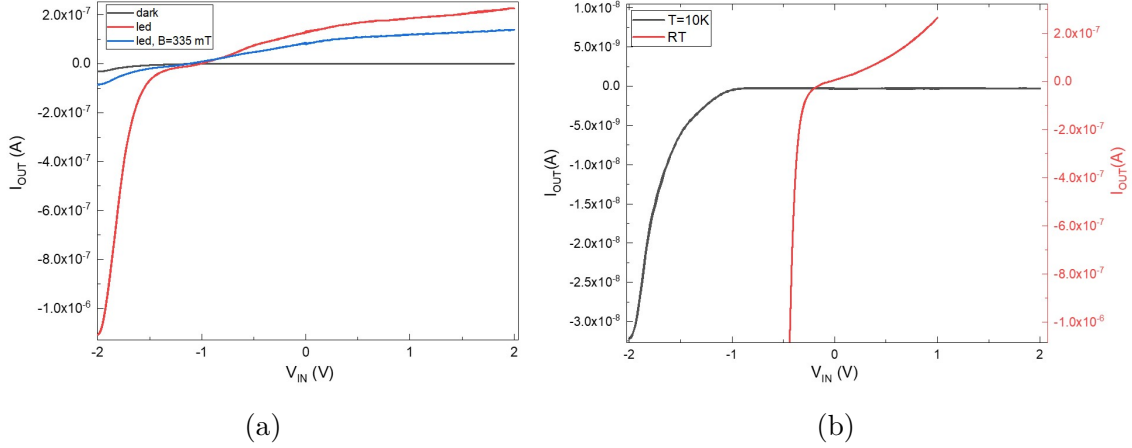
Figure 4.27: Arsenic concentration 8×10^{17} atoms/cm^3: (a) I-V measured in a vertical configuration at 10 K, in dark, under illumination and with an applied static magnetic field. V_{IN} is applied to the top electrode. (b) Comparison between the top-bottom I-V characteristic at room temperature and at 10 K.

The results presented in this and the previous section highlighted the importance of the DNPU's substrate. Further investigations are ongoing to clarify the role of the substrate in charge transport. In particular, we configured a 3-dimensional simulation of the DNPU's structure and electrical behavior with Sentaurus Device, in collaboration with Dr. Lucia Zullino (STMicroelectronics). More details are given in the outlook (Chapter 6) of this thesis.

4.5   Spin dependent transport

In this section, we will report on the analysis of spin dependent transport mechanisms in the dopant network processing units. The results presented here are obtained by performing electrically detected magnetic resonance on three DNPUs, with different dopants concentration. We already mentioned in chapter 3, that EDMR is a powerful technique to investigate the spin properties in nanoscale devices, allowing to identify the paramagnetic centers involved in spin dependent transport. Moreover, information about the spin dependent transport mechanisms can be extracted.

All the EDMR measurements presented in this section, unless otherwise stated, are performed at the fixed microwave frequency of $\approx 9.4 \; GHz$ and microwave power of 190 mW. The magnetic field is modulated at 5 kHz with a modulation amplitude of 0.28 mT. The DNPU is cooled down to 10 K, with liquid helium. Finally, the experiment is performed by monitoring the photocurrent in resonance condition. Therefore the DNPU is put under illumination with a red light source. The choice of red over blue, is due to the higher photocurrent reached in the first case.

Concentration: 4×10^{18} atoms/cm^3

An initial configuration with two electrodes is investigated. An electrode is used as input, with a constant voltage bias of 1 V applied to it. A second electrode, opposite to the first, is used to measure the current output and it is connected to the detection circuitry of the EDMR setup. The resulting EDMR signal is reported in figure 4.28b (black spectrum). The bad signal-to-noise ratio made it difficult to extract information from these measurements, even if a small signal is clearly visible. It is still a quite impressive result, considering that the distance between the electrodes is only 300 nm, meaning that only few dopants are present to be detected. Furthermore, all the electrodes and wires present in the resonant cavity can be a noise source, due to the interaction with the microwaves. It has been demonstrated [95], that the suppression of microwave rectification effects can increase the signal-to-noise ratio up to 15 times. In our case, it was not possible so far to solve this problem. A new DNPU electrodes configuration is in fact needed, meaning a new device fabrication. We should re-think the DNPU geometry in such a way to at least move the bonding wires outside the resonant cavity.

To circumvent this problem, we managed to increase the signal intensity by applying a voltage bias to the back gate in such a way to polarize the DNPU substrate. In the previous section we focused on the DNPU substrate, noting that it is composed by a n^+p junction, even though strong non-idealities are present. Therefore, polarizing the back gate results in a variation of the depletion region of the junction. In

the same figure 4.28b, it is shown an example in which a back gate of -1 V is applied. The new configuration is visible in figure 4.28a, while the resulting spectrum is in red. The measurement is still noisy but now we can start to distinguish a proper signal from the background. The resulting spectra for different voltages
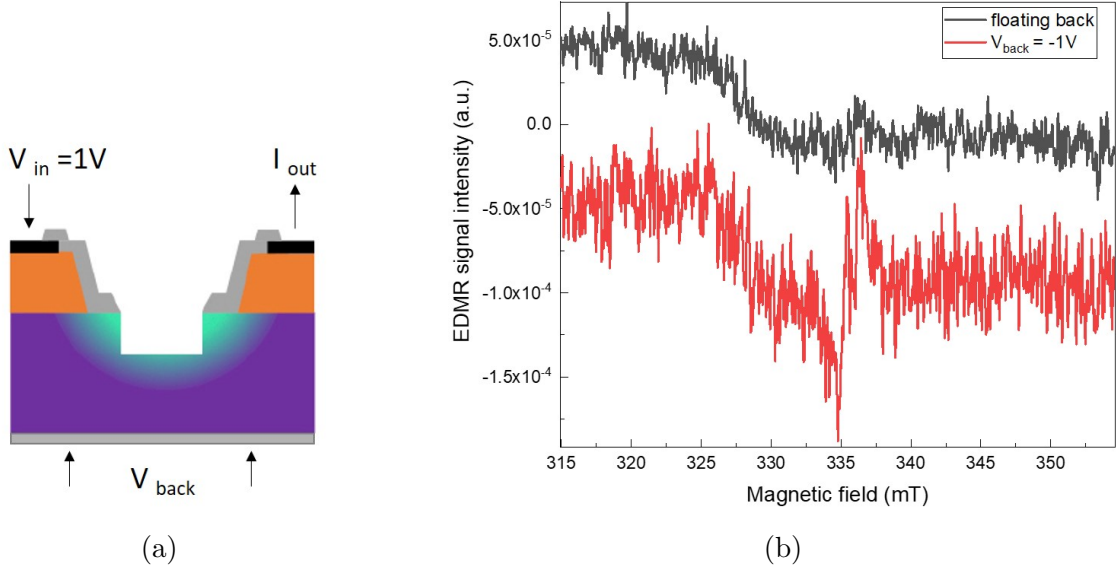
Figure 4.28: (a) Schematic of the electrodes configuration employed for EDMR measurements. Two top electrodes are used as input/output. The back gate is used to apply a constant voltage bias, to polarize the substrate. (b) EDMR spectra without (black) and with (red) the back voltage, measured at 10 K with microwave power of 190 mW.

applied to the back gate are shown in figure 4.29. The signal increases for increasing negative back gate 4.29a. The same happens for positive back gate 4.29b, even if the normalized signal is smaller. It is also possible to notice that changing the polarization of the back, and therefore of the junction, affects the signal phase. However, from the electrical characterization presented before we know that the polarization of the back affects the I-V characteristic. At the input voltage used for EDMR measurements ($V_{IN} = 1V$), the DNPU output current is negative(/positive) for negative(/positive) back voltage. The variation of the EDMR signal phase is therefore due to the variation in the current sign. Considering the absolute value therefore, the output current in resonant condition always increases. To analyze the EDMR spectrum, let us consider the configuration with an applied back gate of -5 V, that results in the highest signal. A negative back gate voltage means that the n^+p junction is in reverse bias. From the fitting of the EDMR spectrum, shown in figure 4.30a, we can extrapolate the g-factors that identify the species involved in spin dependent transport. A g-factor of approximately 1.9983 is found, that corresponds to the arsenic single line. Considering the high dopants concentration in this DNPU, it is reasonable to expect no hyperfine splitting of the arsenic levels.
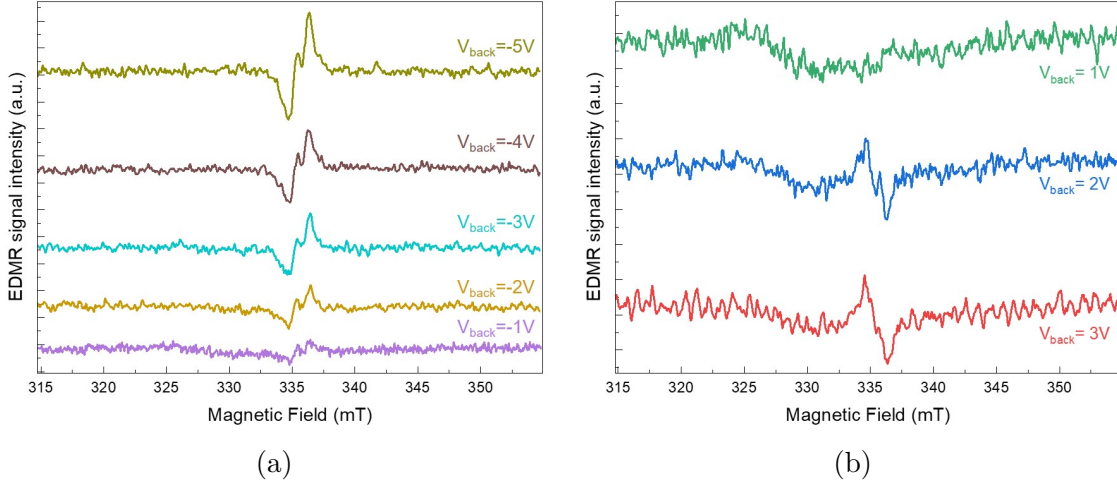
Figure 4.29: (a) Resulting EDMR spectra for different negative back voltages. (b) Resulting EDMR spectra for different positive back voltages. Measurements are performed at 10K, with microwave power of 190 mW.

The four lines have already collapsed into one. The other detected signal comes from the defects at the interface between the doped silicon and the native oxide on top of it. This structure can be fitted with a line centred at approximately $g \approx 2.003$, that could be attribute to the P_b centers [96]. Since we are observing the photocurrent variation, it is therefore possible to conclude that interface defects and clusters of arsenic act as recombination centers. The recombination rate is decreased in resonant condition, resulting in the measured increase in photocurrent (in this case, the current is more negative in resonance). The same lines can be measured with the substrate in forward bias as shown in figure 4.30. Also in this case the observed spin dependent mechanism is recombination via interface defects and dopants, characterized by a reduction of the recombination rate. Another structure, with a g-factor of 2.05(1) and a linewidth of about 8 mT, is now visible due to the weaker signals related to As and P_b. This signal is attributed to a not yet identified background signal from the silicon substrate [97]. So far the measurements were taken in a planar configuration: spin dependent transport through the active region has been investigated, while polarizing the n^+p junction thanks to the back contact. To better understand the role of the substrate, a vertical configuration is now studied, measuring the spin dependent transport through the n^+p junction. The DNPU configuration is presented in figure 4.31a. A constant voltage bias is sourced to one of the DNPU's electrode on the top and the output current is monitored at the back, while sweeping the magnetic field. For positive input voltage at the n^+ region, the junction is in reverse. An EDMR signal can be measured and it increases in intensity with the input voltage. In order to detect a signal while the junction is polarized in forward, a higher V_{IN} is needed that is consistent with the photocurrent asymmetry shown in 4.25a. The resulting EDMR spectra are shown in figure 4.31b.

(a)

(b)
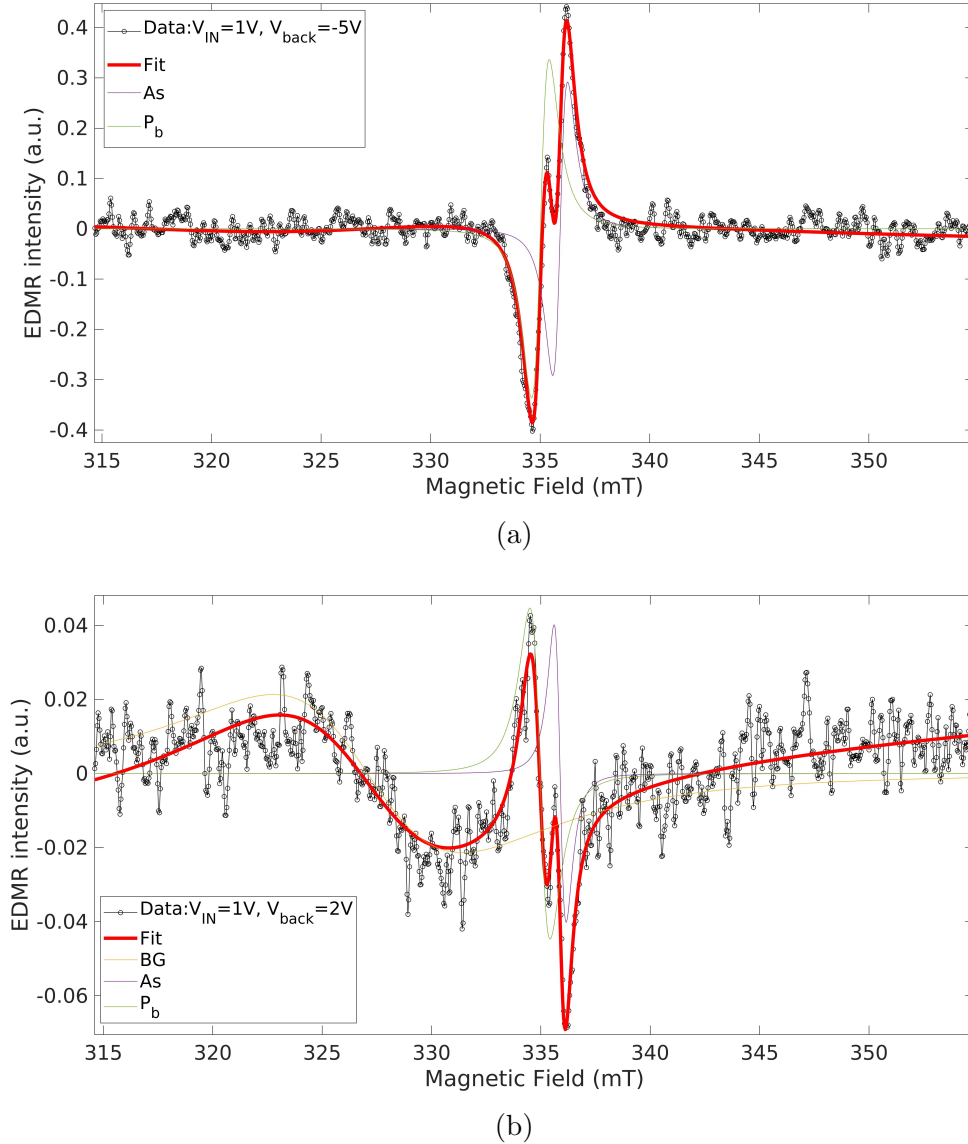
Figure 4.30: Fit of the EDMR signal obtained applying a back gate voltage of $V_{back} = -5\ V$ (a) and $V_{back} = 2\ V$ (b). ($P_{\mu w} = 190\ mW$, T=10 K).

Again fitting the spectrum allow us to extract the g-factors of the species involved 4.32. We found that also in this case, arsenic atoms and defects at the interface act as recombination centers. Considering the signal phase, photocurrent increases in resonance due to a reduced recombination rate. EDMR measurements confirm once more, that the junction in the DNPU substrate does not behave like an ideal $p-n$ junction. No resonant signal is detected monitoring the dark current, opposite to what is expected in the depletion region of a $p-n$ junction [76].

(a)   (b)
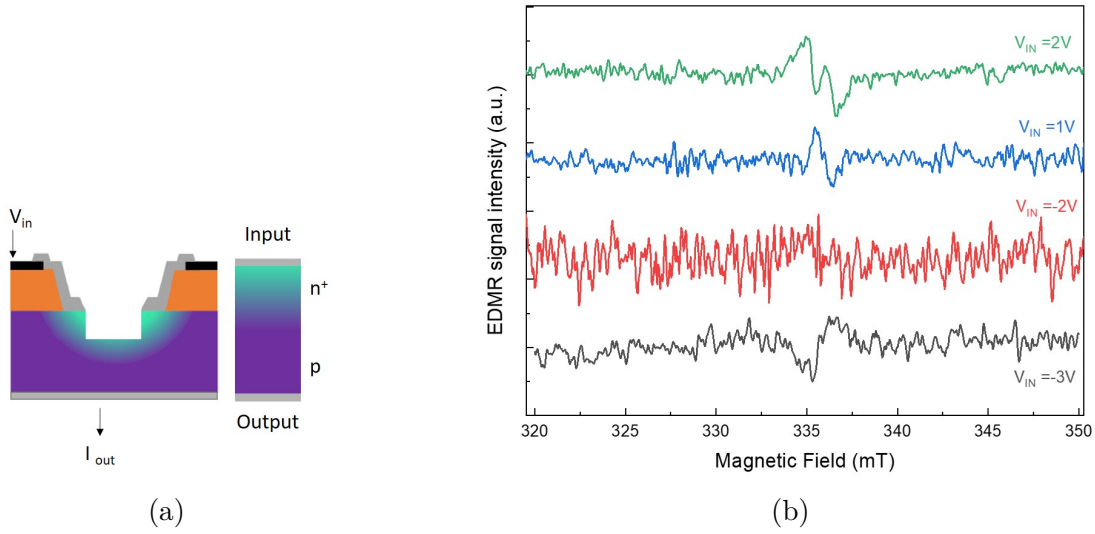
Figure 4.31: (a) Schematic of the electrodes configuration employed for EDMR measurements. One of the electrodes on the top is used as input, while the back gate is used to measure the output current. An ideal representation of the n^+p junction is also shown. (b) EDMR spectra obtained for different input voltages, meaning different junction polarization. Measurements are performed at 10 K, with microwave power of 190 mW.
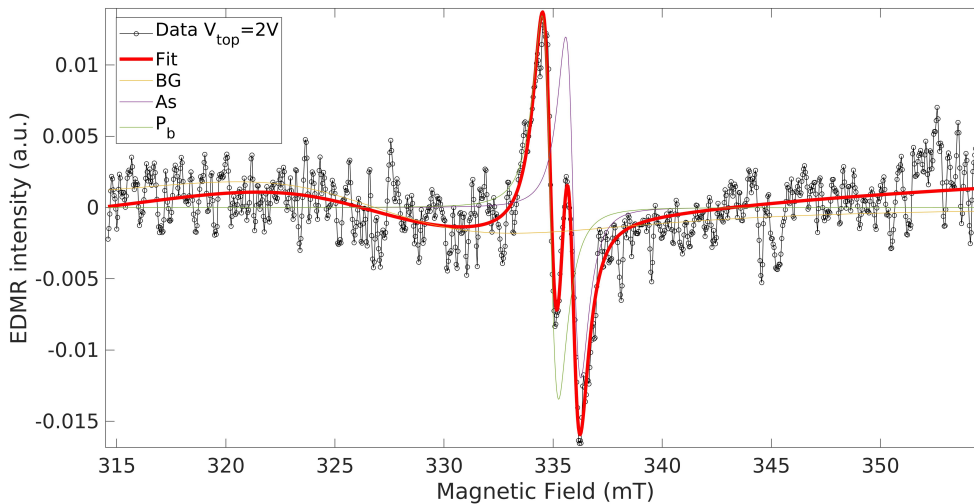
Figure 4.32: Fit of the EDMR signal obtained in a vertical configuration with an input voltage of +2 V. The junction is in reverse bias. ($P_{\mu w} = 190\ mW$, T=10 K).

Finally, a proof-of-concept experiment is performed on this DNPU. The idea is to perform EDMR measurements in the same conditions in which the DNPU can solve the Boolean logic gates. We would like to explore the possibility that the DNPU computational capability might be somehow spin dependent. Therefore we wish to prove whether spin transport mechanisms might be correlated to the dopant network tunability. The starting point is a simplified Boolean logic gates experiment, but there are plenty of different possible configurations. The number and the complexity of experiments can easily be expanded. This experiment does not aim at replicating the Boolean logic gates tasks. We are rather trying to analyze the simplest possible configuration in which the DNPU operates, from a point of view of the spin physics. If we succeed in adding spin dependent functionalities in this simple configuration, then more complex configurations will follow. In order to have a better control of the DNPU's behavior and to reduce the amount of variables, we employ the minimum number of electrodes. We consider a four electrodes configuration: two electrodes are used to send input voltages (V_{IN1} and V_{IN2}), one electrode opposite to the second input is used to measure the output current, and the fourth one, next to the output, is used to apply a control voltage. Figure 4.33 shows the input voltages and output current over time, together with the correspondent EDMR spectra. As input voltages we consider a series of '0' and '1' in order to obtain all the possible combinations. V_{IN1} can be seen as a [0011], while V_{IN2} as [0101]. The logic '1' corresponds to a voltage of 0.5V applied to the DNPU's electrode. A control voltage of 0.9V is applied to the control electrode and the resulting output current is plotted in black in the figure. The green line is a guide for the eye. This measurement is performed with the DNPU under illumination (red light source) and in the presence of a static magnetic field of 335 mT, in order to reproduce the EDMR condition. The output current is negative. Therefore we consider its absolute value and we can define as '0' the low current level and as '1' the high current level. The output current can be represented by a [0101] function. EDMR measurements were then performed in the four different configurations and the resulting spectra are reported in the figure. For clarity: the black spectrum corresponds to inputs '00' and output '0', the red one to inputs '10' and output '1', the blue on to inputs '01' and output '0', and the green to input '11' and output '1'. This means for example that to perform the last measurement (green) a voltage of 0.5 V is applied to both the input electrodes, a voltage of 0.9 V is applied to the control electrode and finally the output electrode is connected to the EDMR detection circuitry. From this experiment, it seems that the detection of an EDMR signal is possible only when the output current is in the '1' state. No signal is instead observed in the output '0' state. It is important to note that the current variation between the '0' and '1' states is very little. We can therefore exclude the possibility that the '0' current is

too low to be detected in a EDMR experiment. However, before drawing any further conclusions this experiment needs to be reproduced and other configurations need to be tested. We should be sure that the detection or not of the EDMR signal is only related to a physical reason. Every possible experimental factor that precludes the signal detection needs to be excluded.
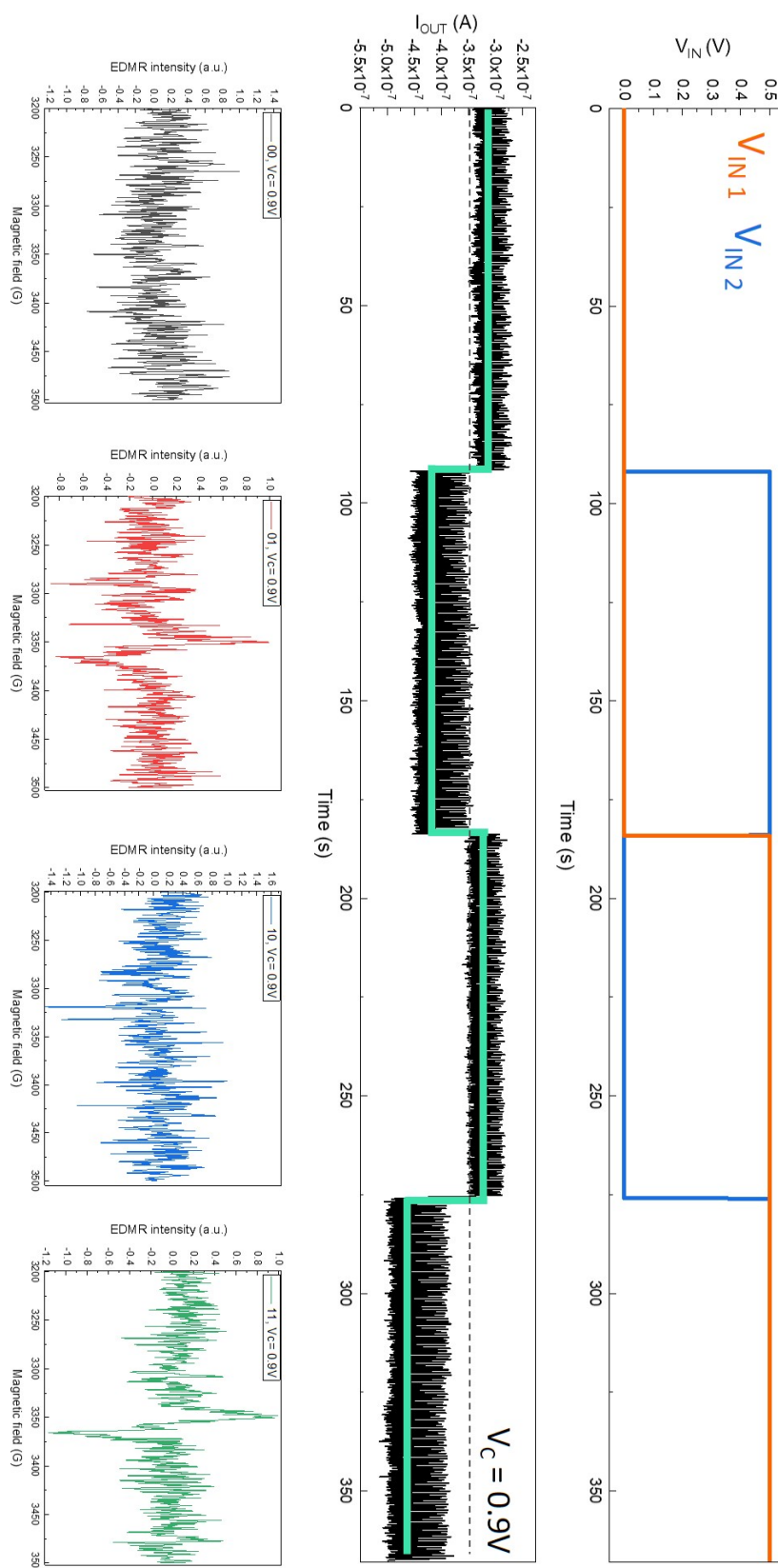
Figure 4.33: Boolean logic gate experiment, from the top: combination of input voltages '0' and '1' over time, correspondent output current when a control voltage is applied, resulting EDMR spectra in the four different combination of inputs.
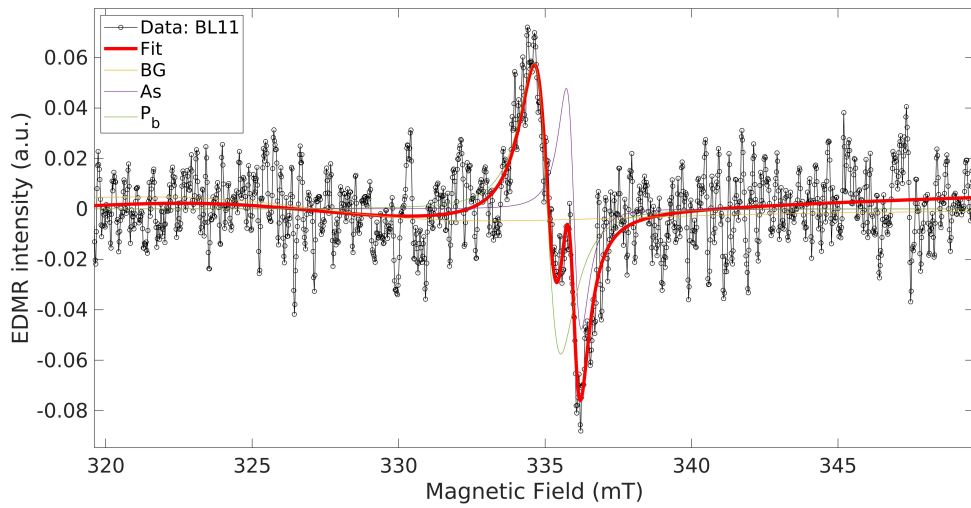
(a)
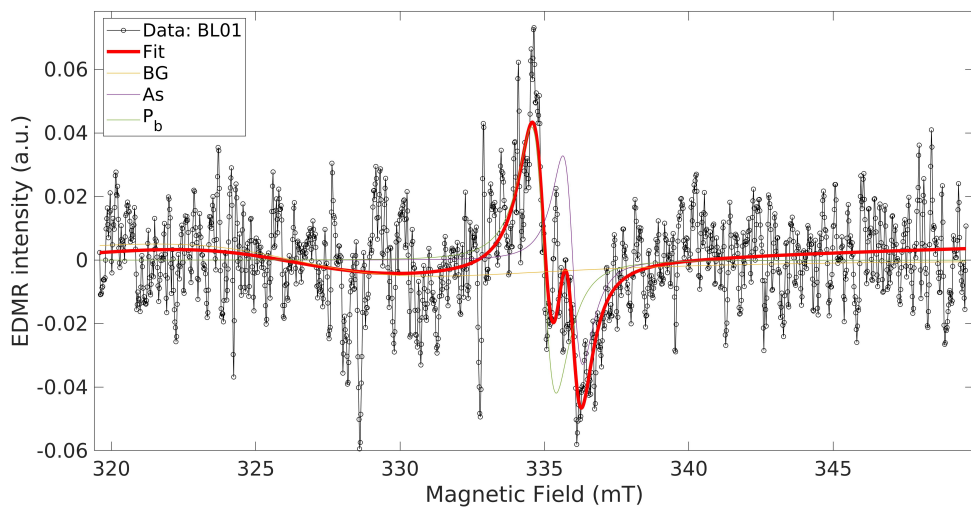
(b)

Figure 4.34: Fit of the EDMR signal obtained in the output '1' state: (a) '11' inputs (b) '01' inputs. ($P_{\mu w} = 190\ mW$, T=10 K).

In the following table 4.2 we summarize the fitting parameters of every configuration in which EDMR measurements were performed and presented above. The RMSD (root mean square deviation) gives an indication of how close the fitting curves are to the experimental data. All the EDMR spectra presented above can be fitted with two lines that we attributed to the arsenic single line and to the P_b centers. In the values of the g-factors and linewidths, the errors on the last digit are given in parenthesis. Besides the first configuration, all the other spectra present a third structure at $g \approx 2.05$. The linewidth of this signal varies around (10 ± 5) mT, with a really high weight (190000) due to the large signal width. Since the weights in the fitting procedure are given as absolute and not relative, we decided to not consider this broad signal intensity. The arsenic and P_b weights are then renormalized over their sum and expressed as percentage of the total signal intensity. It is possible to observe in the table, that the signals are well reproduced in every configuration. Only little variations in g-factors, linewidth, and relative weights are detected, compatible with the experimental uncertainty.

Configuration	RMSD	specie	g-factor	line-width (mT)	weight %
Planar: $V_{IN} = 1\ V$, $V_{back} = -5\ V$	0.02	^{75}As	1.9984(2)	0.64(2)	36
		P_b	2.0036(5)	0.78(5)	64
Planar: $V_{IN} = 1\ V$, $V_{back} = 2\ V$	0.007	^{75}As	1.9984(2)	0.59(2)	31
		P_b	2.0043(5)	0.83(5)	69
Top-bottom: $V_{IN} = 2\ V$	0.0017	^{75}As	1.9983(2)	0.69(2)	46
		P_b	2.0046(5)	0.71(5)	54
Boolean logic 11	0.012	^{75}As	1.9984(2)	0.51(2)	21
		P_b	2.0038(5)	0.91(5)	79
Boolean logic 01	0.013	^{75}As	1.9984(2)	0.69(2)	38
		P_b	2.0043(5)	0.78(5)	62

Table 4.2: Fitting parameters for the EDMR spectra of the DNPU with arsenic concentration of 4×10^{18} atoms/cm^3.

Concentration: 2×10^{18} atoms/cm^3

Spin dependent transport is investigated also in this DNPU. The arsenic concentration is lower than before, but still close to the critical value. Therefore, we do not expect to detect the arsenic hyperfine splitting yet. The results on this DNPU are very similar to the previous case, as we also expected from the consistent electrical behaviour. Also on this DNPU, we performed EDMR measurements applying a voltage to the back. We could confirm that the substrate polarization increases the EDMR signal, otherwise not really distinct from the background noise. Figure 4.35 shows the resulting EDMR spectra obtained with different input voltages and back voltages. The different values are indicated in the plot. Also in this case the current sign needs to be considered in the interpretation of the signal phase. Since also in this case no EDMR signal is detected when the DNPU is in dark, it is possible to conclude that the main spin dependent mechanism observed is recombination. In particular, the photocurrent in absolute value increases in resonant condition due to a decrease in the recombination rate. The top-bottom configuration is also investigated to analyze spin dependent transport through the substrate. The resulting EDMR spectra are presented in figure 4.36. In the plot the applied input voltage to the top electrode is indicated. Also in this case, the EDMR signal is detected only when the measurement is performed under photoexcitation confirming the non-ideality of the junction. Again the opposite phase is in fact due to the change in the photocurrent sign, that is almost symmetric when a static magnetic field is also applied 4.26a.
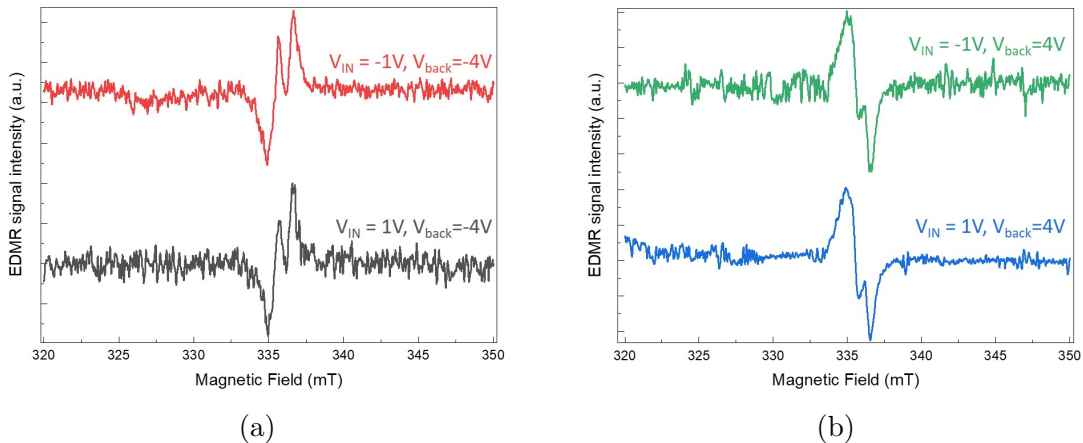
Figure 4.35: (a) EDMR spectra for negative back voltage and different input voltages. (b) EDMR spectra for positive back voltage and different input voltages. Measurements are performed at 10 K, with microwave power of 190 mW.
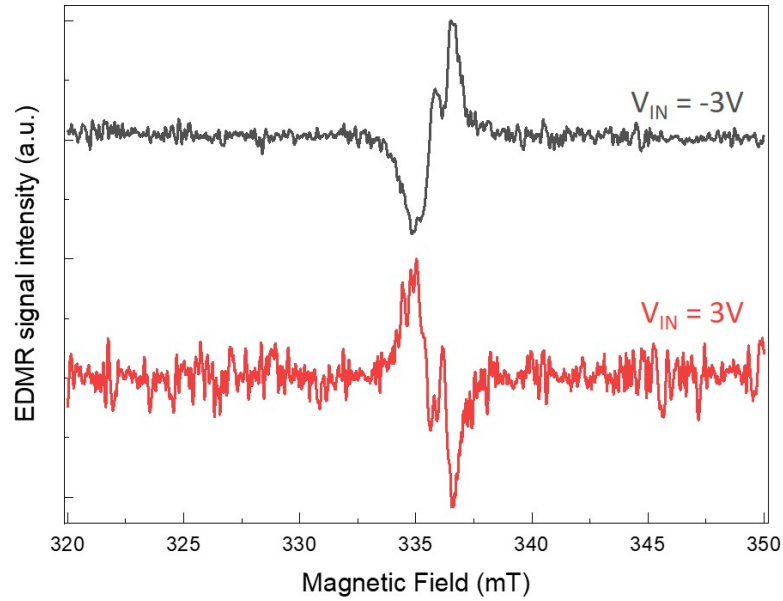
Figure 4.36: EDMR spectra measured in the top-bottom configuration. The input voltage is applied to the top electrode. Measurements are performed at 10 K, with microwave power of 190 mW.

The data fitting are shown below. Figures 4.38 and 4.37 refer to the EDMR measurements performed in a planar configuration with respectively positive and negative voltages applied to the substrate. In figure 4.39 instead the vertical configuration is considered. All the spectra can be fitted with two lines that we attributed to the arsenic dopants ($g \approx 1.9984$) and P_b centers ($g \approx 2.004$), consistent with the previous DNPU.
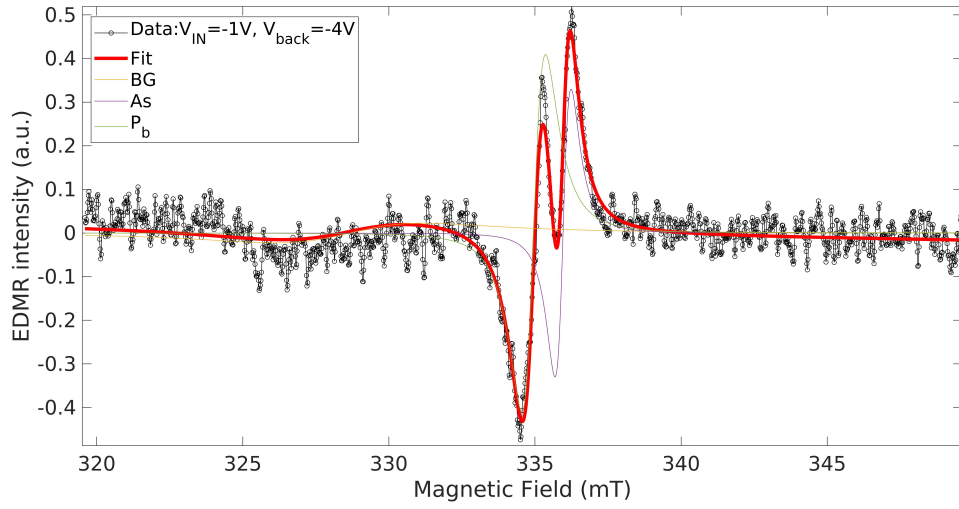
(a)
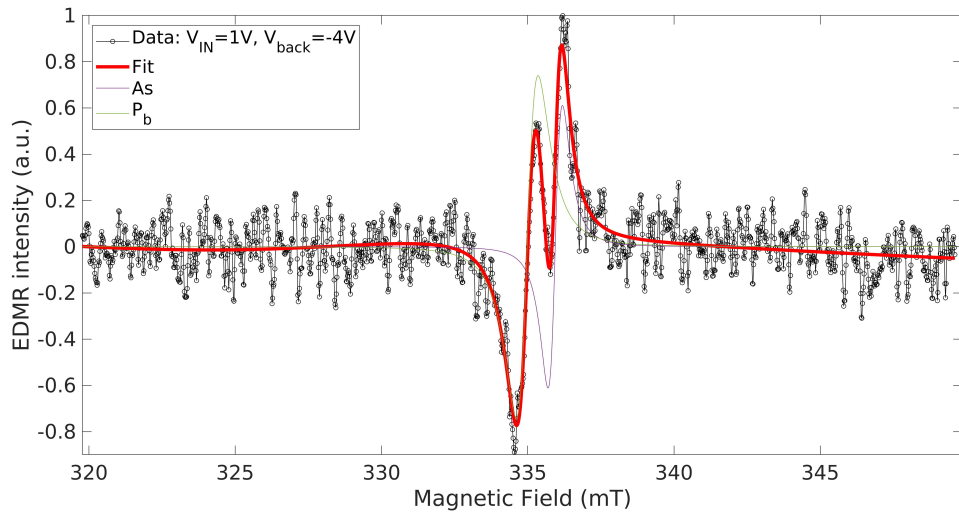
(b)

Figure 4.37: Fit of the EDMR signals obtained applying a back gate voltage of $V_{back} = -4\ V$ and different input voltages. ($P_{\mu w} = 190\ mW$, T=10 K).
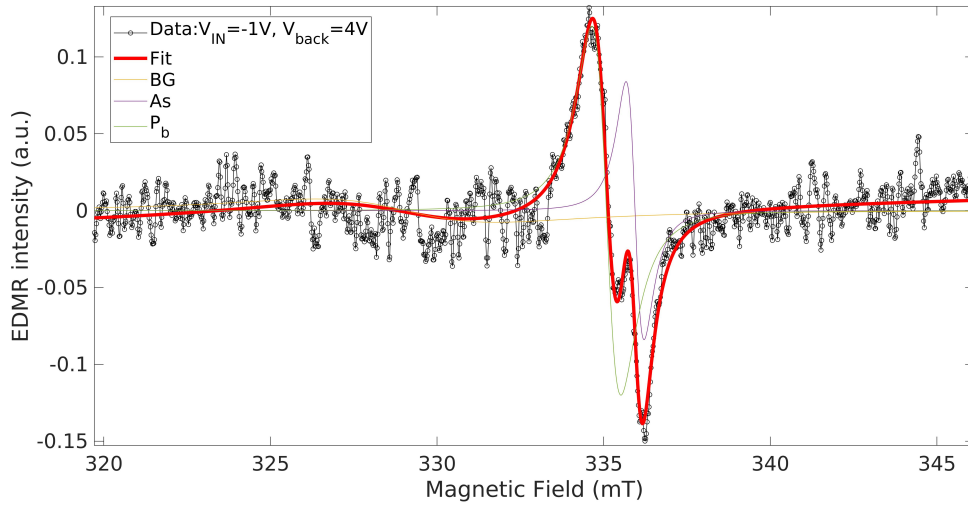
(a)
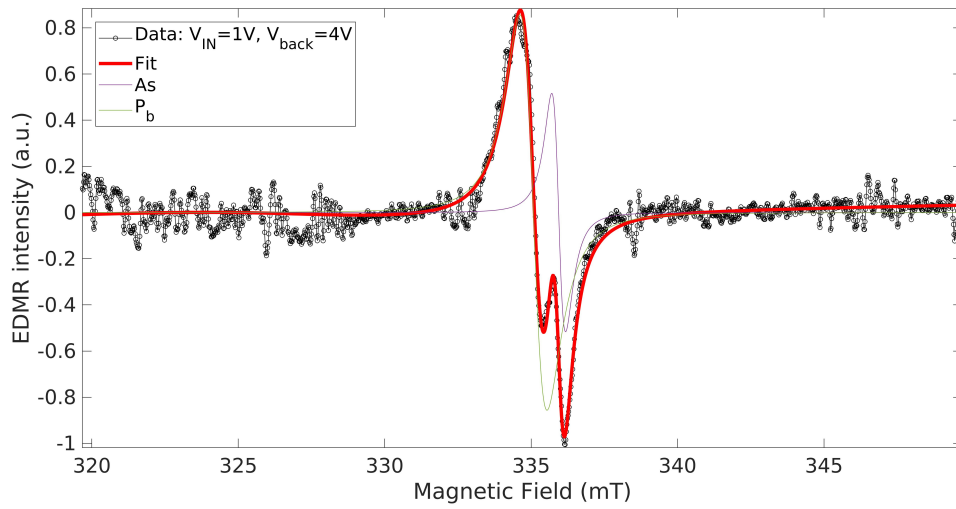
(b)

Figure 4.38: Fit of the EDMR signals obtained applying a back gate voltage of $V_{back} = +4\ V$ and opposite input voltages. ($P_{\mu w} = 190\ mW$, T=10 K).
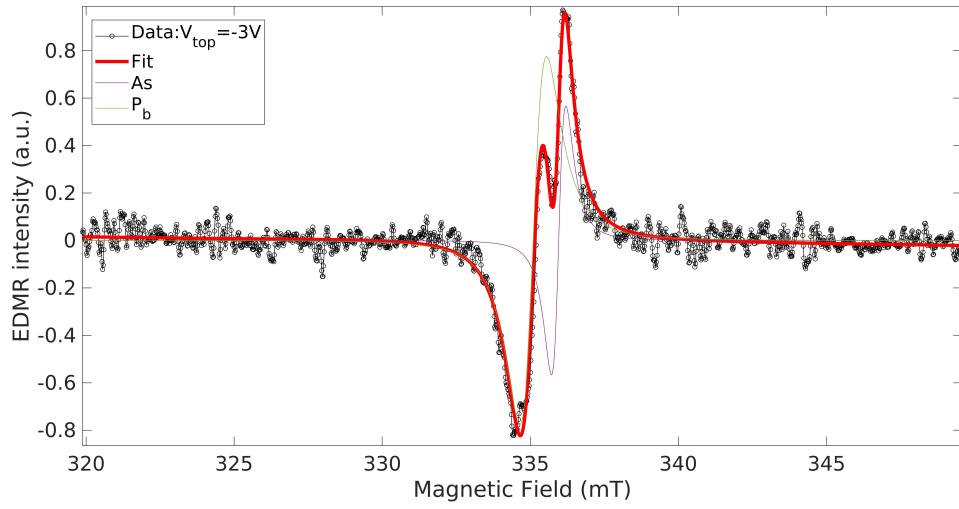
(a)
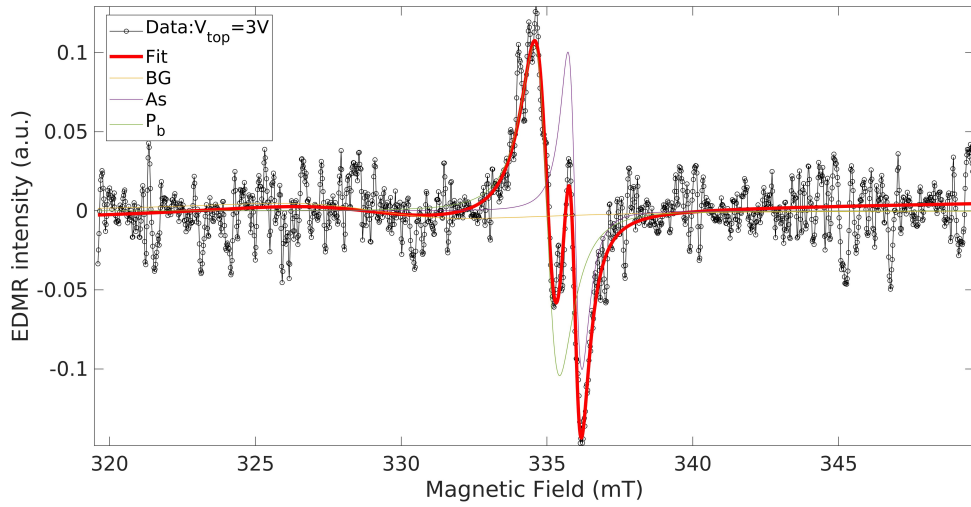
(b)

Figure 4.39: Fit of the EDMR signals obtained in a vertical configuration with an input voltage of (a) $V_{IN} = -3\ V$ and (b) $V_{IN} = 3\ V$. ($P_{\mu w} = 190\ mW$, T=10 K).

In the following table, we listed the fitting parameters of the EDMR spectra shown in this section. Errors and relative weights are indicated as in the previous section. Also in this case a third structure can be considered in the fitting curve, more or less pronounced in the different configurations. It is centered at $g \approx 2.04$ and variable linewidth of approximately (7 ± 5) mT.

Configuration	RMSD	specie	g-factor	linewidth (mT)	weight %
Planar: $V_{IN} = -1\ V$, $V_{back} = -4\ V$	0.04	^{75}As	1.9984(2)	0.53(2)	24
		P_b	2.0043(5)	0.84(5)	76
Planar: $V_{IN} = 1\ V$, $V_{back} = -4\ V$	0.09	^{75}As	1.9984(2)	0.48(2)	25
		P_b	2.0042(5)	0.76(5)	75
Planar: $V_{IN} = -1\ V$, $V_{back} = 4\ V$	0.012	^{75}As	1.9984(2)	0.55(2)	22
		P_b	2.0035(5)	0.87(5)	78
Planar: $V_{IN} = 1\ V$, $V_{back} = 4\ V$	0.06	^{75}As	1.9984(2)	0.47(2)	16
		P_b	2.0036(5)	0.92(5)	84
Top-bottom: $V_{IN} = -3\ V$	0.05	^{75}As	1.9984(2)	0.48(2)	17
		P_b	2.0035(5)	0.90(5)	83
Top-bottom: $V_{IN} = 3\ V$	0.015	^{75}As	1.9984(2)	0.48(2)	20
		P_b	2.0042(5)	0.87(5)	80

Table 4.3: Fitting parameters for the EDMR spectra of DNPU with arsenic concentration of 2×10^{18} atoms/cm^3.

5 Silicon On Insulator

In this chapter I will present the analysis of the spin properties and spin dependent transport mechanisms of a phosphorus doped silicon-on-insulator (SOI) device. The approach is the opposite to that of the previous chapter. The starting point is the study of the material's properties in a simple configuration. The follow-up will be the fabrication of a more complex device, with a working mechanism based on properly tailored physical properties.

This work was carried out in collaboration with Dr. Michele Perego from CNR Institute for Microelectronics and Microsystems Unit of Agrate Brianza (IMM-CNR). Fabrication and a first electrical characterization were performed at IMM-CNR, while the study of the spin properties was carried out at the MSNS laboratory, Department of Material Science at the University of Milano-Bicocca.

| (a) | (b) |
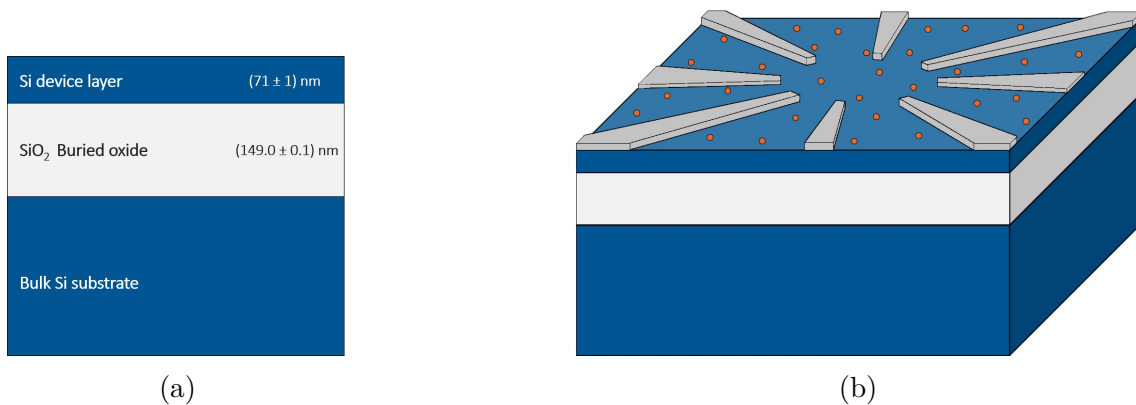
Figure 5.1: Silicon on insulator technology: (a) schematic of a SOI substrate, (b) schematic of a proposal for a SOI-based DNPU.

A schematic of a SOI substrate is depicted in figure 5.1a. It consists in a three layer structure: a thin monocrystalline silicon layer (the device layer), an amorphous SiO_2 layer (the buried oxide, BOX) and finally a bulk silicon substrate. The BOX is usually characterized by low defect density, high thickness uniformity, and high quality of Si/SiO_2 interfaces. The thickness of the device layer and the BOX can be tuned and optimized for specific device operations and especially for device shrinking. When scaling down the device layer thickness below 10 nm, quantum con-

finement in the thickness direction starts to play a role and needs to be considered in the device behavior. Employing SOI technology in semiconductor manufacturing has been proven to provide important advantages [98][99] such as: reduction of parasitic capacitances, improvement of the device performance and operation speed, reduction of operation voltage and power consumption, increased reliability, and finally reduction of undesirable short-channel effects which enables to continue the MOSFET miniaturization into the nanometer region [100] [101].

This chapter is organized as follow. First the main aspects of the SOI devices fabrication are presented. Second, we will analyze the spin properties of the Si:P device layer. For clarity, results will be presented separately for every studied device, each with a different device layer thickness.

5.1 Fabrication

The fabrication of the Si:P SOI devices studied in this thesis was carried out by Andrea Pulici, at the CNR Institute for Microelectronics and Microsystems Unit of Agrate Brianza (IMM-CNR). All the details can be found in his master thesis ([102]). Starting from a conventional SOI substrate, the doping of the silicon layer was performed by grafting of phosphorus end-terminated polymers. This method was proposed by Perego *et al.* in [103], as an effective bottom-up technology for precise monolayer doping. By properly adjusting the molar mass (M_n) of the functional polymers, fine tuning of the dopant dose is achieved. Moreover the self-limiting nature of the grafting process guarantees an accurate and reliable control over the dopants concentration, together with a precise localization of the atoms.

The main steps in the device fabrication and doping process are presented below. The pristine SOI substrate is composed by a buried oxide with a thickness of (149.0 ± 0.1) nm and a device layer of (71 ± 1) nm. The thicknesses were measured via spectroscopic ellipsometry and fitted with a $SiO_2 - Si - SiO_2$ trilayer model. In order to investigate different silicon layer thicknesses, SOI substrates were treated with a "thinning" procedure. Cycles of dry thermal oxidation and subsequent HF-bath, were performed to obtain the desired thickness. A thermal oxide layer was grown onto the surface of the sample via RTP (rapid thermal process) treatment at 1000°C in a oxidizing atmosphere. The formation of the oxide layer consumes up to 44% of the silicon layer. Samples were then dipped into HF solution (1:50) to remove the superficial oxide layer. This "thinning" procedure was repeated multiple times, resulting in substrates with a device layer thickness that varies from 30 nm to 6 nm. ToF-SIMS measurements were also performed after every cycle in order to confirm that the device layer and the Si/SiO_2 interface were not damaged during the process.
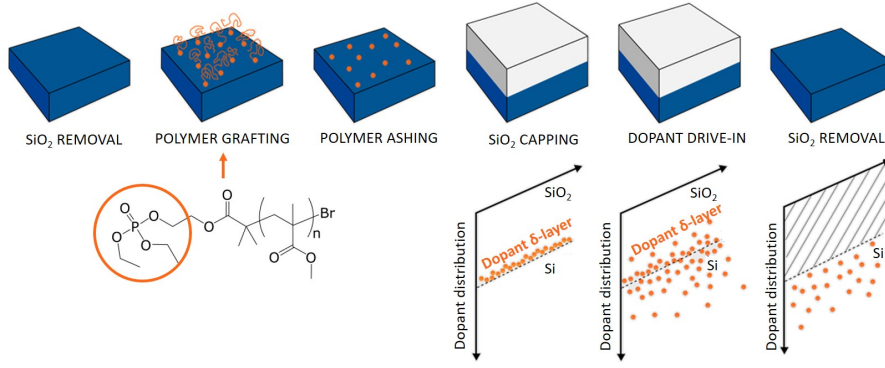
Figure 5.2: Schematic of the doping process, adapted form [103].

A schematic of the doping process is presented in figure 5.2. Phosphorus-terminated polymethil methacrylate (PMMA-P) homopolymers were employed, with molar mass $M_n = 7.5 kg/mol$, polydispersity index $D = 1.14$, degree of polymerization $N = 72$ and gyration radius $R_G = 2.4 nm$. Every polymeric chain carries exactly one phosphorus atom. PMMA-P homopolymers were synthesized and characterized by the chemical industrial group of prof. Michele Laus at University of Piemonte Orientale. The homopolymers were dispersed in toluene (9 mg/mL) and then spin coated on the deglazed substrates for 30 s at 3000 rpm. The resulting film is homogeneous over the sample with a thickness of about 30 nm. To promote the grafting reaction between polymers end-terminated with a dopant-containing moiety and the silicon surface, samples were annealed using RTP for 15 min at 210°C in N_2 atmosphere. The non-grafted chains were washed out by ultrasonic bath in toluene for 5 min. After the grafting-to process, polymeric chains were removed by O_2 plasma hashing (40 W for 5 min) leaving only phosphorus on the surface. The iteration of grafting/ashing cycles allows to increase the dose of P atoms grafted to the silicon surface in a cumulative and stepwise way [104]. Samples were then capped with a 10 nm thick SiO_2 layer deposited by e-beam evaporation, in order to prevent contamination and P outgassing. A δ-layer of phosphorus dopants is therefore embedded at the $SiO_2 - Si$ interface. RTP treatment is then performed in N_2 static atmosphere, in order to diffuse the P atoms into the silicon layer. Finally, the oxide capping layer was removed with a 5 min bath in HF solution. Circular aluminum electrodes (1.2 mm of diameter) were then deposited by thermal evaporation using a shadow mask. The resulting devices are $10 \times 10 \ mm^2$, with four electrodes at the sample corners. Electrical characterization of the samples' resistivity and carrier concentrations were performed measuring the Hall effect in a van der Pauw configuration. Samples were then further diced in a $10 \times 3 \ mm^2$ piece with two electrodes, in order to perform EDMR measurements and investigate spin dependent transport.

Table 5.1 shows the details of the SOI Si:P samples studied in this work. For every device layer thickness the concentration of phosphorus dopant atoms is given. Thicknesses are measured via spectroscopic ellipsometry, as mentioned before. The ToF concentration is the result of the ToF-SIMS measurements performed by Dr. Michele Perego. ToF-SIMS measurements show a flat doping profile, confirming that the SOI device layer is uniformly doped. The extracted concentrations of phosphorus impurities are all above the Mott transition. Hall effects measurements were also performed on the SOI sample by Andrea Pulici. The Hall coefficient can be extracted and consequently the carrier type (n) and the carrier concentration, reported in the following table.

Thickness (nm)	ToF concentration (cm^{-3})	Hall concentration (cm^{-3})
30.12	4.05×10^{18}	3.99×10^{18}
20.92	5.66×10^{18}	4.22×10^{18}
11.35	7.23×10^{18}	1.97×10^{18}
6.00	1.04×10^{19}	3.9×10^{17}

Table 5.1: Parameters of the analyzed SOI samples. The thickness of the device layer, and the phosphorus concentration extracted from the ToF and Hall effect measurements are listed.

5.2 Device layer 30 nm

The first analyzed SOI devices have a silicon layer of approximately 30.12 nm. Two samples were investigated. The first one is a pristine SOI substrate, that has undergone only the "thinning" procedure. The second one, initially identical to the first one, has then been doped with phosphorus atoms following the doping process described in the previous section. Comparing the results of the two devices we aim at distinguishing the role of the SOI substrate and of the phosphorus doping. It is important to recall that the SOI substrate has two silicon/oxide interfaces: one between the device layer and the BOX and the second one with the native oxide on top of the silicon layer. Interface defects coming from both these interfaces may therefore contribute to spin dependent transport, in particular recombination processes. Analyzing the doped sample, we first aim at verifying the efficacy of the doping procedure. Secondly, we investigate how the incorporation of dopants may affect the spin properties of the SOI substrate, introducing for example spin dependent transport mechanisms.

EPR

Electron paramagnetic resonance measurements are first performed on the devices. The microwave source is fixed in the X band ($\approx$ 9.4 GHz) and different microwave power are tested, varying from 1 mW up to 60 mW. The magnetic field is modulated at frequency $f_{mod} = 100$ kHz with an amplitude of 0.1 mT. All the measurements were performed at 4.2 K. EPR spectra for Si:P SOI substrate are shown in figure 5.3a as a function of the microwave power. The measurements were taken keeping the sample in dark. Two signals are clearly visible: a line with $g \approx 1.9985$ related to the phosphorus dopants and a second broad line which we attributed to the interface. A single phosphorus line is consistent with the high concentration of dopants in this sample, and confirms the efficacy of the doping procedure. In figure 5.3b we evaluate the signal intensity as a function of the square root of the microwave power to verify the signal saturation. The intensity is intended as an approximation of the signal integral, estimated as the product between the signal intensity variation (peak to peak) and the correspondent field variation elevated to the second power $\Delta I \times \Delta B^2$. Repeating the measurements with the sample under illumination we can
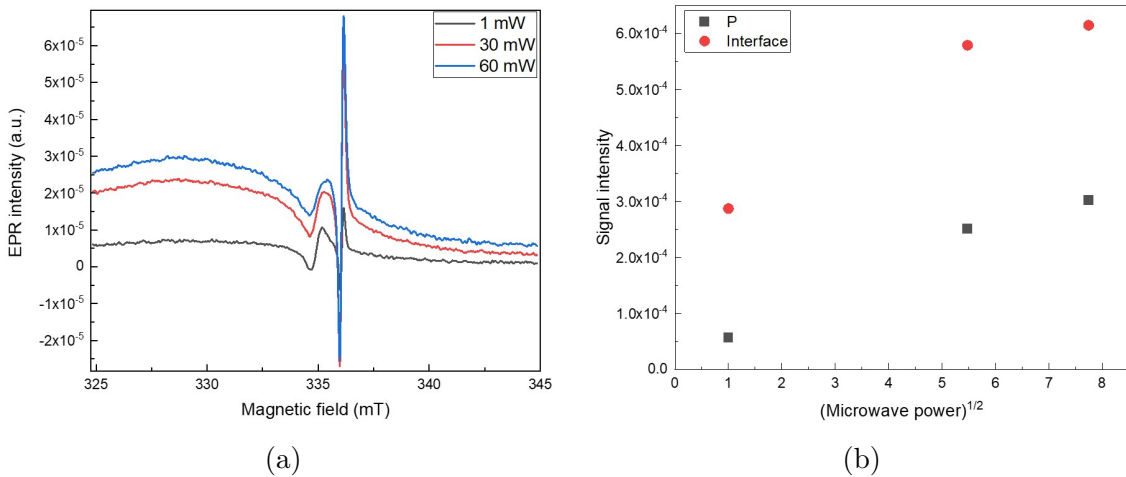
Figure 5.3: (a) EPR spectra of the Si:P SOI sample (30nm) in dark. (b) Microwave power dependence of the signal intensity. Measurements are performed at 4.2 K.

now well distinguish two signals in correspondence of the broad line in dark. This signal is only visible at microwave power greater than 30 mW, as shown in figure 5.4a. Comparing the EPR spectrum taken in dark and under illumination at 60 mW (figure 5.4b) we can see that photoexcitation does not affect the phosphorus signal. To better understand the signal coming from the silicon/silicon oxide interface, we performed EPR measurement on the pristine SOI substrate, without doping. No signal is detected when the sample is in dark. With the substrate under illumination, two EPR signals are observed at microwave power higher than 20 mW. The EPR spectra taken under photoexcitation are presented in figure 5.5a as a function
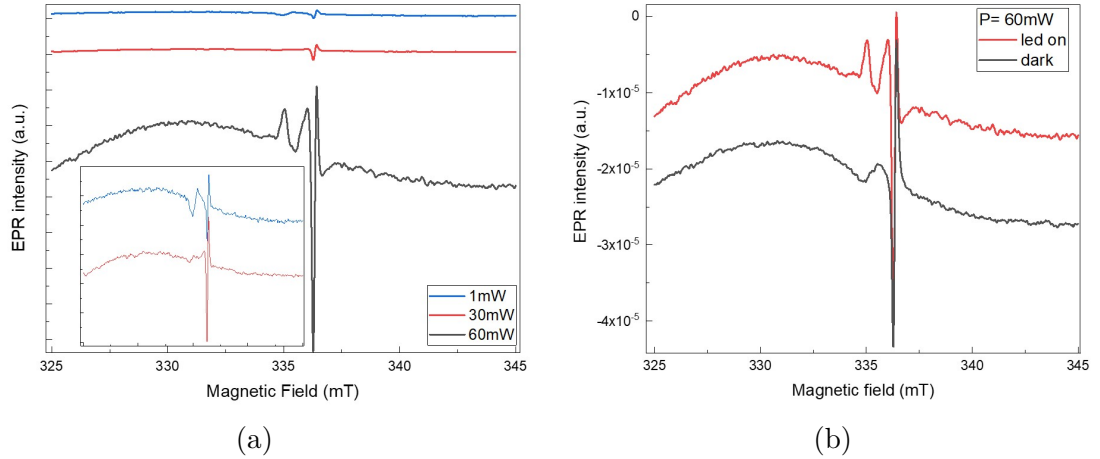
Figure 5.4: (a) EPR spectra of the Si:P SOI sample (30 nm) under illumination. In the inset, the separation of the two signals at 30 mW is shown. (b) Comparison between the dark EPR signal and the photoexcited EPR signal. Measurements are performed at 4.2 K.

of the microwave power. Figure 5.5b shows the intensity as a function of the square root of the microwave power for the two signals. The intensities of both signals increase with microwave power without reaching saturation in the analyzed power range. These EPR signals can be attributed to the conduction electrons ($g \approx 1.999$) and silicon dangling bonds ($g \approx 2.005$), as we will discuss below. Figure 5.6 shows
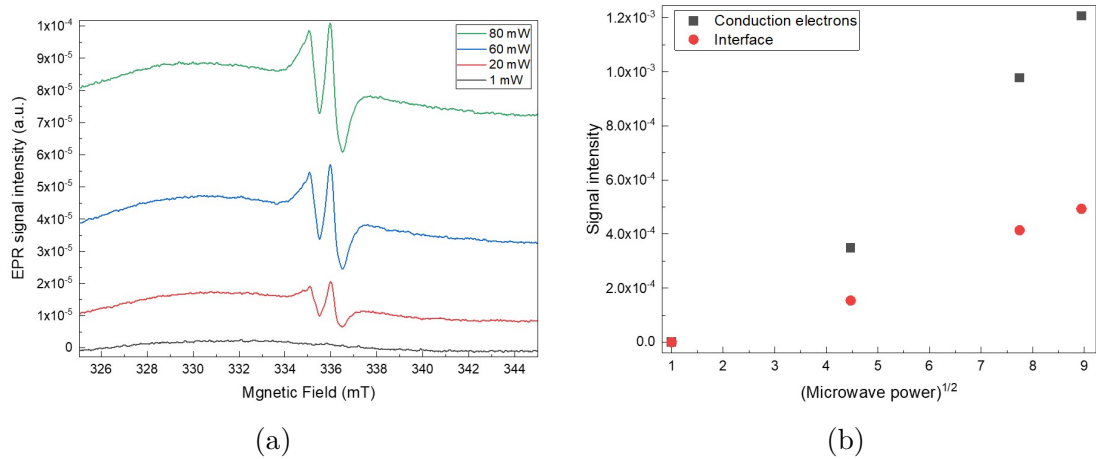
Figure 5.5: (a) EPR spectra of the SOI substrate (30 nm) under illumination. (b) Microwave power dependence of the signal intensity. Measurements are performed at 4.2 K.

the comparison between the EPR spectra of an SOI substrate with (Si:P SOI) and without (SOI) phosphorus implantation. It is also indicated in the plot if the measurement is taken in dark or under illumination (led on, in short). The grey area points out the structures that seem to be related to the SOI substrate, and therefore can be observed in both the samples. All the measurements in this plot are taken at the microwave power of 60 mW.
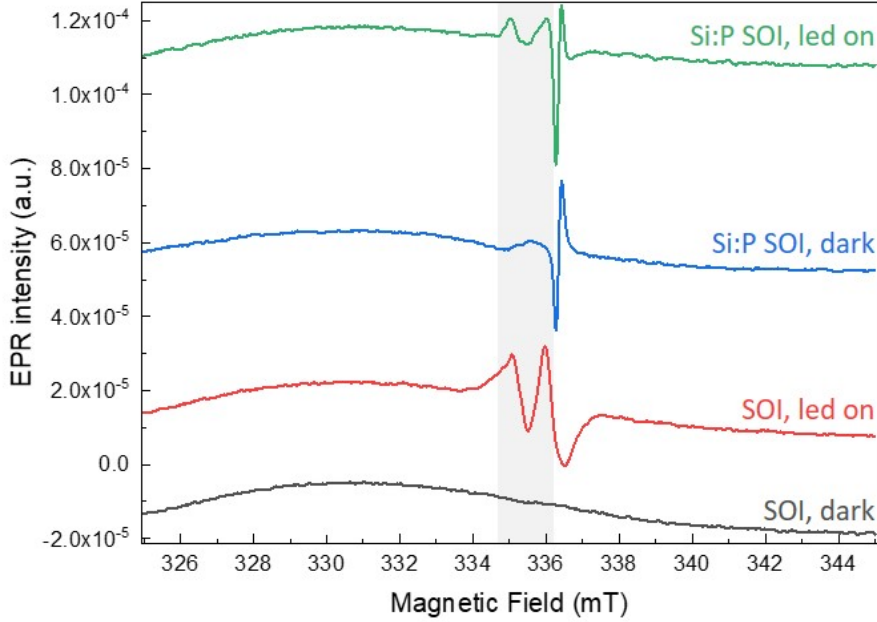
Figure 5.6: Comparison between the EPR signals of the SOI samples with and without phosphorus doping, measured at 4.2 K with microwave power of 60 mW. The grey area highlights the EPR signals present in both the samples.

Data fitting and discussion

In this section we analyzed more in detail the EPR spectra shown before, presenting and discussing the data fitting. Figure 5.7 reports the best obtained fitting of the EPR data, in particular (a) refers to the Si:P SOI sample measured in dark, (b) to the Si:P SOI sample under illumination, and (c) to the SOI substrate under illumination. For clarity the extracted g-factors, linewidth, and weight are listed in the following table 5.2. The experimental errors are given in parentheses.

In all the measurements seen so far it is possible to note the presence of a background signal. We could model it with a EPR line centred at a fixed g-factor of $g \approx 1.998$ and with a varying linewidth of (20 ± 5) mT, to best adapt to the different data sets. The origin and physical meaning of this background is still under discussion. However, it has to be considered to properly fit the data. As in the previous chapter we exclude the background in the estimation of the signals' percentage weights. In the Si:P SOI sample the phosphorus line is clearly visible when the sample is investigated both in dark and under illumination. The extracted g-factor is of approximately $g \approx 1.9984(2)$ that is consistent with the value for P dopants in silicon reported in literature (1.99850). Also a linewidth of 0.15 mT is in agreement with the reported values [71] [105]. In the SOI substrate, EPR signals are only visible under photoexcitation and at high microwave power. The data can be fitted with two lines. The first one from the right has a g-factor of about 1.999, that can be attributed to the silicon conduction electrons (CE) [106]. Under illumination,

carriers are in fact being photogenerated in the conduction band. The second EPR signal is related to the interface. The extracted g-factor of approximately 2.0049 can be associated to the silicon dangling bonds (DB) [107]. We expected and actually found the same two lines in the Si:P SOI sample when measured under illumination. Considering now figure 5.7(a), other EPR structures are also visible, besides the P line. The broad signal can be fitted with two lines with g-factors consistent with conduction electrons and dangling bonds as before, even if the linewidths are slightly different. Comparing the EPR spectra in dark and under illumination (5.7(a) and (b)) it is possible to note that beside the P line, the other structures have opposite phase when photo excited. Looking back at figure 5.4a (a) it is clear that the phase variation is not only due to illumination, but it is also related to the microwave power. High microwave power and illumination allow us to detect an out-of-phase EPR signal. The underlying mechanisms is still under discussion, but similar out-of-phase signals, particularly strong for interface defects, are reported in literature for phosphorus-doped silicon under illumination [108].

Sample	RMSD	specie	g-factor	line-width (mT)	weight %
Si:P SOI dark	0.017	^{31}P	1.9984(2)	0.15(2)	33
		CE	1.9989(2)	0.24(2)	16
		DB	2.0049(5)	0.69(5)	51
Si:P SOI led	0.02	^{31}P	1.9984(2)	0.14(2)	18
		CE	1.9991(2)	0.35(2)	5
		DB	2.0049(5)	0.46(5)	32
SOI led	0.02	CE	1.9991(2)	0.46(2)	57
		DB	2.0049(5)	0.49(5)	43

Table 5.2: Fitting parameters for the EPR spectra of the 30 nm samples.

(a)

(b)

(c)
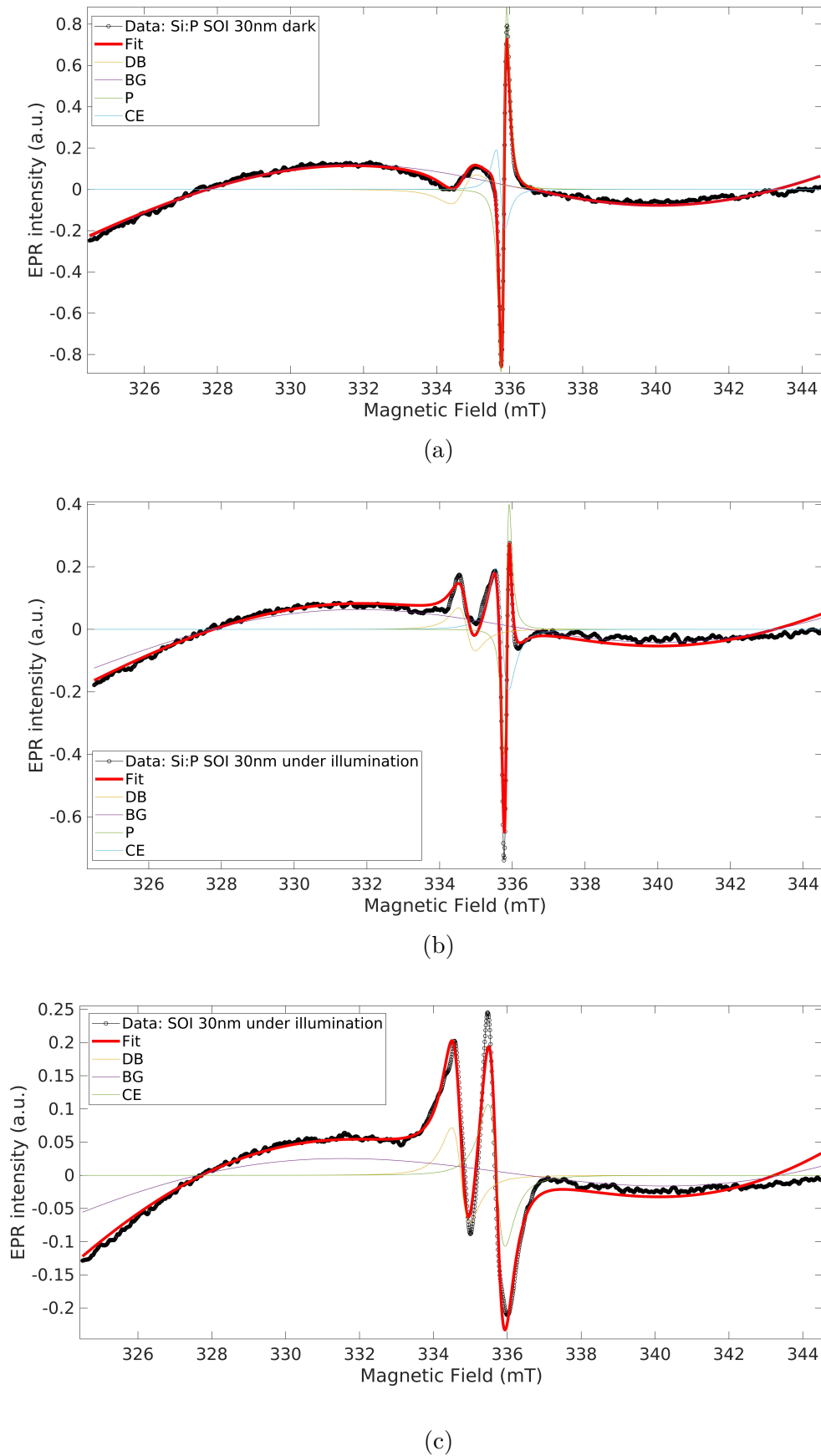
Figure 5.7: Data fitting of the EPR signals of the 30 nm samples, measured at P=60 mW and T=4.2 K: (a) Si:P SOI in dark, (b) Si:P SOI under illumination, (c) SOI under illumination.

95

EDMR

In order to identify the paramagnetic centers that are involved in spin dependent transport, electrically detected magnetic resonance is performed. The microwave source is fixed in the X band (≈ 9.4 GHz) and the highest possible microwave power is used (P = 190 mW). The magnetic field is modulated at frequency $f_{mod} = 5 \, kHz$ with an amplitude of 0.1 mT. A DC voltage of 10 V is applied to one electrode, while the other one is connected to the detection circuitry. If not otherwise stated, EDMR measurements were performed illuminating the samples with a blue light source, monitoring the photocurrent variation. All the measurements were performed at 4.2 K. An I-V measurement is first performed on the Si:P SOI device to evaluate its electrical behavior in dark and under illumination. The resulting curves are plotted in figure 5.8. When spin dependent recombination processes are investigated, the EDMR signal is proportional to the photogenerated carriers and therefore to the difference between photocurrent and dark current. Considering the current value at 10 V, it is possible to estimate an increase in photocurrent of two orders of magnitude. We can also notice in the inset that the dark current is almost linear at low temperature. This linearity is found only in the 30 nm device layer sample. The
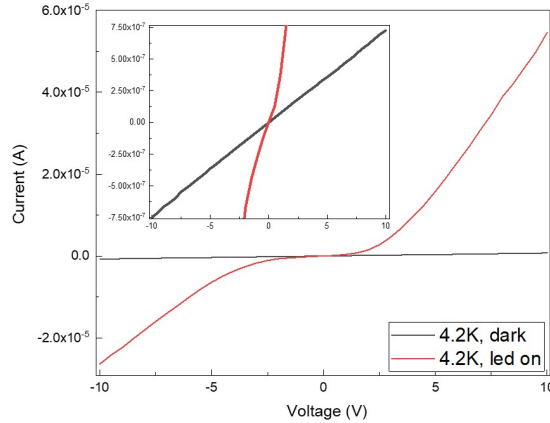
Figure 5.8: I-V measurements of the 30 nm sample at 4.2 K. The inset shows an enlargement of the dark current.

resulting EDMR spectra are reported in figure 5.9: the conventional measurement with the sample under illumination (red line) and the one in dark (black line). Interesting to note that this device is the only one that shows a resonance signal without photoexcitation. Monitoring the dark current variation in resonance gives us information about spin dependent scattering processes in the device. Fitting the data is possible to extract the g-factors that identify the different structures in the spectrum. More details will be given later in the dedicated section. A single signal is detected performing EDMR in dark. The g-factor indicates that P dopants are involved in spin dependent scattering. Considering the signal phase, the current is

reduced in resonance as a consequence of an increased scattering rate. The signal does not present angular dependence, confirming the expected isotropy of the P line. The same signal is also detected in the EDMR measured under illumination, with the same phase. Other structures are observed when the variation of photocurrent is measured. The extracted g-factors can be attributed to the conduction electrons ($g \approx 1.999$), E' centers ($g \approx 2.002$) and silicon dangling bonds ($g \approx 2.005$). All these signals have a positive phase, meaning that the photocurrent increases in resonance due to a reduced recombination rate. To better define the broad signal from the
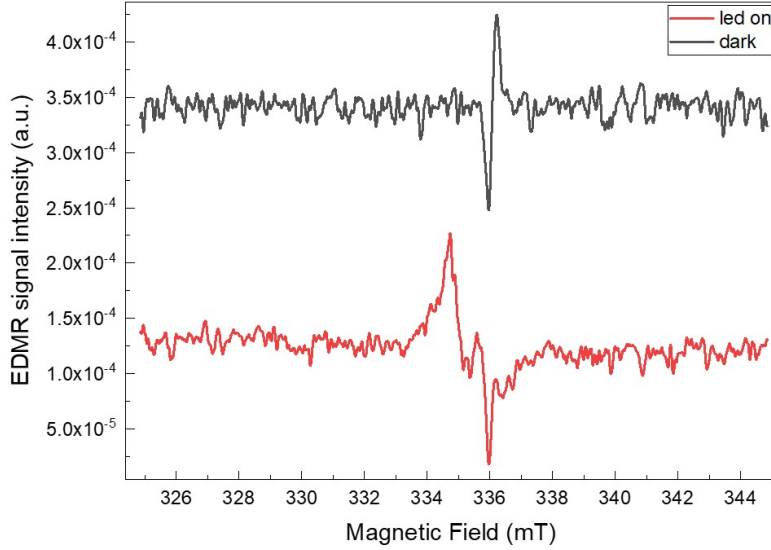
Figure 5.9: EDMR spectra of the Si:P SOI sample (30 nm), measured in dark and under photoexcitation at 4.2 K with microwave power of 190 mW.

interface, we change the sample orientation. The EDMR spectrum at 20° is shown in figure 5.10. Angles are measured with respect to the [100] direction. At 0° the magnetic field is parallel to the [110] direction. The signals we associated to the interface defects are affected by the orientation. The intensity is reduced because of the limited illumination in this configuration. The lines related to P dopants, conduction electron and E' center are not affected by the different orientations, due to their isotropic nature. As it will be clarified later the P line is visible as a shoulder in the conduction electrons signal. The interface signal split in two, with g-factors of approximately 2.004 and 2.0075, compatible with the P_{b0} centers [109]. To validate our hypothesis we tested the pristine SOI substrate, without phosphorus implantation. We first noticed that no resonance signal is detectable in dark. When the sample is illuminated EDMR signals can be measured as visible in figure 5.11. These signals can be identified as the resonance of silicon dangling bonds and conduction electrons, confirming what seen before. As in the previous case, the photocurrent increases in resonance due to a reduced recombination rate. Figure 5.12 presents a comparison of the EDMR spectra of the 30 nm SOI samples. The
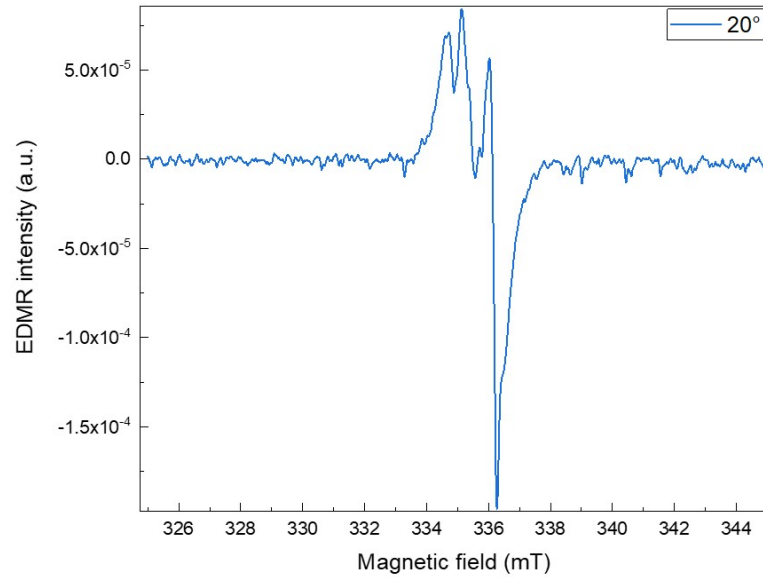
Figure 5.10: EDMR spectrum of the Si:P SOI sample (30 nm), measured under photoexcitation at 20°. The measurement is performed at 4.2 K, with microwave power of 190 mW.

grey area highlights the signal coming from the SOI substrate that are reproduced in the phosphorus implanted sample. This plot, considering also the result of the data fitting, helps to identify the signal due to the phosphorus dopants.
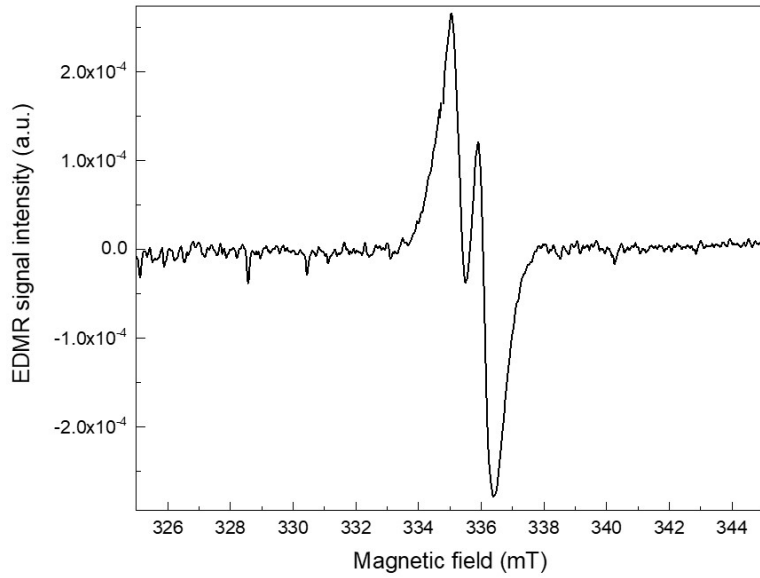
Figure 5.11: EDMR spectrum of the SOI substrate (30 nm), measured under photoexcitation at 4.2 K, with microwave power of 190 mW.
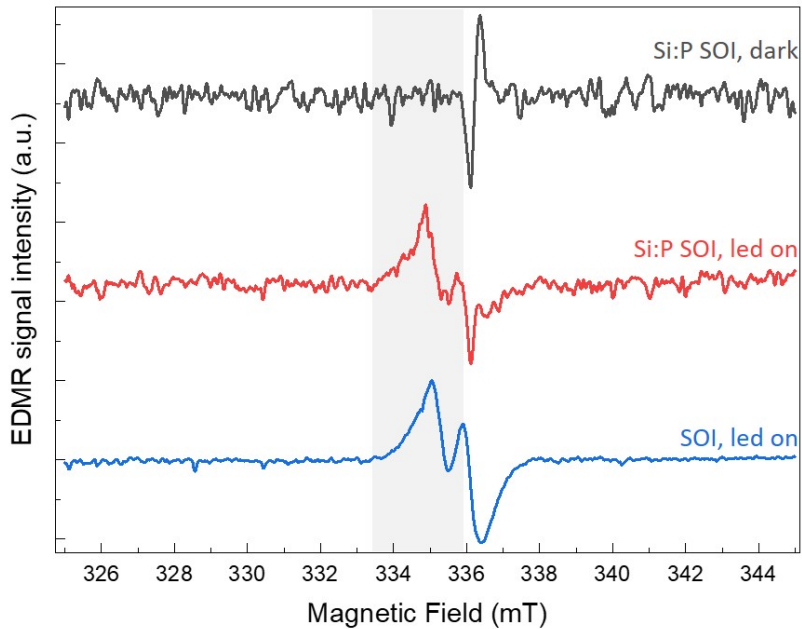
Figure 5.12: Comparison between the EDMR signals of the SOI samples with and without phosphorus doping. The grey area highlights the EDMR signals present in both the samples. Measurements are performed at 4.2 K, with microwave power of 190 mW.

Data fitting and discussion

We now discuss the EDMR spectra more in detail. The fitted data are shown in figure 5.13 and figure 5.14, respectively in the case of P-doped SOI sample and the pristine SOI substrate. The extracted g-factors, linewidths and weights are listed in table 5.3. As before, the parenthesis indicate the uncertainty and weights are re-normalized over the sum of all the signals intensities. The sign (-) in the weights indicates negative signal phase and therefore a reduction of the measured current in resonance. The EDMR spectrum measured in dark (5.13(a)) can be fitted with a single line characterized by a g-factor of 1.99847 and linewidth of 0.14 mT. As already mentioned these values are consistent with the expected ones for clusters of phosphorus atoms. We now propose a scattering mechanism that we think responsible for the detected P signal. We saw in Chapter 2, that at high concentration of phosphorus ($\approx 4 \times 10^{18}$ cm^{-3}, in this case) a dopants miniband is formed. The DOS is centred at E_{dop} and with a certain broadening D_{dop}. It is reasonable to consider that in a central region of the miniband electrons are fully delocalized. A sufficient number of P clusters is formed and electrons can move freely in the miniband. At the same time, considering the miniband tails, it is also possible to have smaller dopants clusters not connected to the others. Electrons are in this case localized: they can move freely within the cluster, but do not contribute to the macroscopic transport. The spin dependent mechanism we are obsessing could therefore be related to scattering between free electrons in the dopant mini band and localized electrons in the P^0 clusters. The difference in g-factor of this spin pair involved in scattering is too little to be detected and this would explain the detection of a single line associated with phosphorus. Our hypothesis follows the theory of spin-dependent scattering between a two dimensional electron gas (2DEG) and donors in a field effect transistor proposed by De Sousa [84]. Adapted to our case, we are assuming that delocalized electrons in the miniband behave like a 2DEG. The same P signal is detected in the photoexcited EDMR and the fitting confirms the g-factor value. The extracted linewidth is slightly larger compared to the value found in the dark spectrum. This could be a fitting error, due to the partial superposition of the P line with the conduction electron signal. It is possible that the same mechanism is still active also under photoexcitation. Other signals are present in the EDMR spectrum measured under illumination and represent the paramagnetic centers involved in spin dependent recombination. Electrons are photogenerated in the conduction band and can recombine forming spin pairs with mid-gap defects. Signals from the conduction electrons ($g \approx 1.999$), silicon dangling bond ($g \approx 2.005$) and E' center ($g \approx 2.002$) are in fact detected. The signal phase is always positive, meaning that the recombination rate is decreased in resonant condition. Considering

Sample	RMSD	specie	g-factor	line-width	weight
Si:P SOI dark	0.009	^{31}P	1.9985(1)	0.14(1)	(-)32
Si:P SOI led	0.03	^{31}P	1.9985(2)	0.18(3)	(-)3
		CE	1.9997(2)	0.54(3)	42
		DB	2.0049(5)	0.56(5)	52
		E'	2.0025(3)	0.23(3)	3
Si:P SOI led 20°	0.019	^{31}P	1.9985(2)	0.14(2)	(-)2
		CE	1.9995(2)	0.42(2)	45
		P_{b0}	2.0041(3)	0.50(5)	38
		E'	2.0022(3)	0.25(3)	4
		P_{b0}	2.0076(3)	0.42(5)	11
SOI led	0.014	CE	1.9997(2)	0.57(2)	55
		DB	2.0044(5)	0.57(5)	45

Table 5.3: Fitting parameters for the EDMR spectrum of the 30 nm samples.

the EDMR spectrum measured at $\theta = 20°$, it is possible to better define the signal coming from the Si/SiO_2 interface. The two lines associated with the P_{b0} centers can now be properly distinguished at $g \approx 2.0041$ and $g \approx 2.0076$. We mentioned before that the P_b centers are the only detected paramagnetic centers showing angular dependence. This anisotropy is due to the crystallography orientation of the defect. Finally also in the pristine SOI substrate, without P doping, it is possible to observe spin dependent recombination processes. Recombination between the same spin pair (CE/DB) is detected, with the same signal phase. Therefore also in this case photocurrent is increased due to a decreased recombination rate.
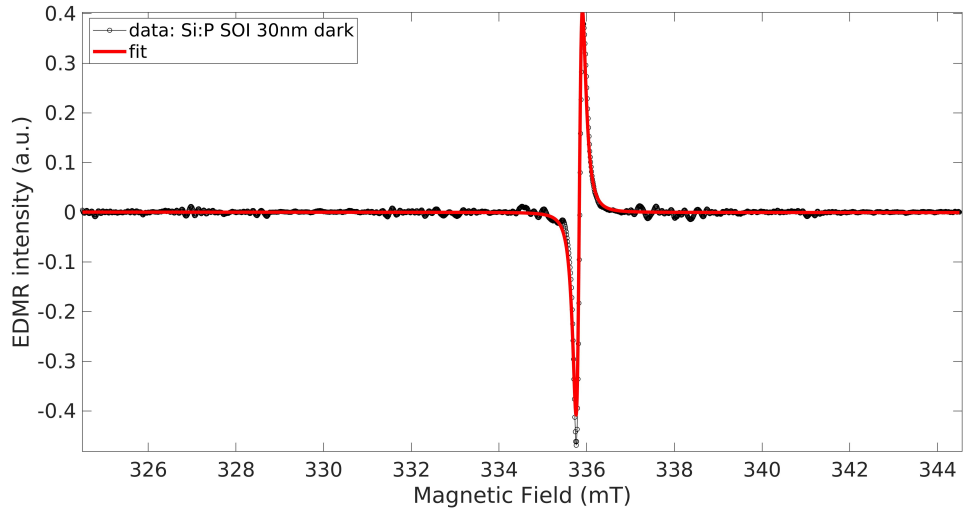
(a)
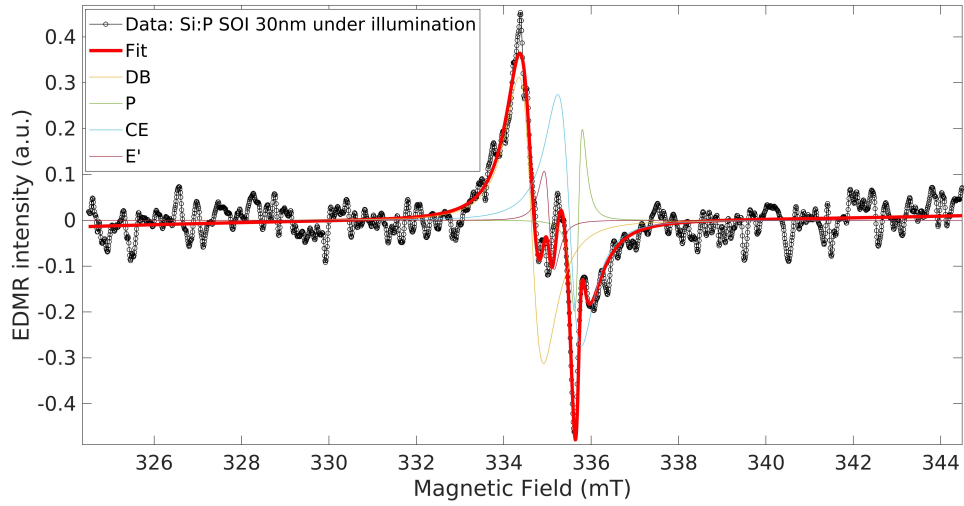
(b)
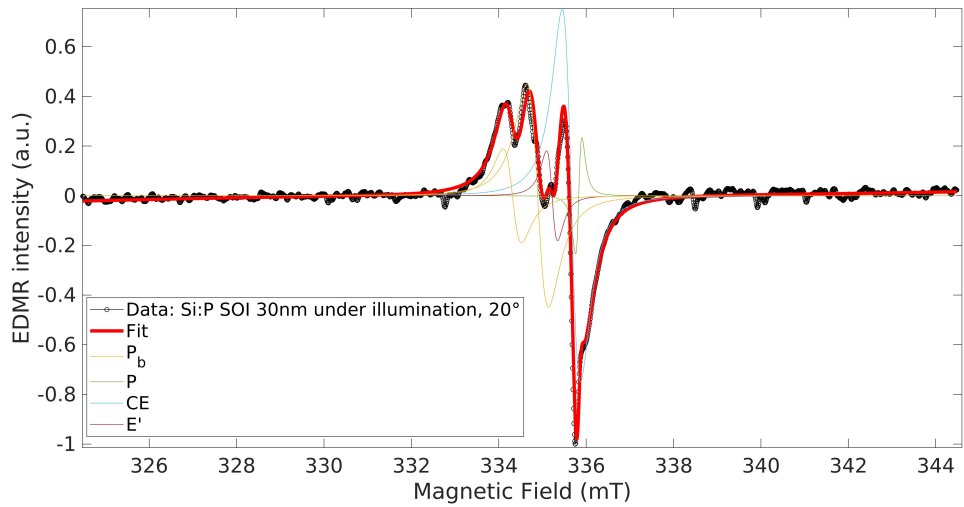
(c)

Figure 5.13: Data fitting of the EDMR signals of the 30 nm samples: (a) Si:P SOI in dark, (b) Si:P SOI under illumination, (c) Si:P SOI under illumination, $\theta = 20°$. ($P_{\mu w} = 190 \; mW$, T=4.2 K).
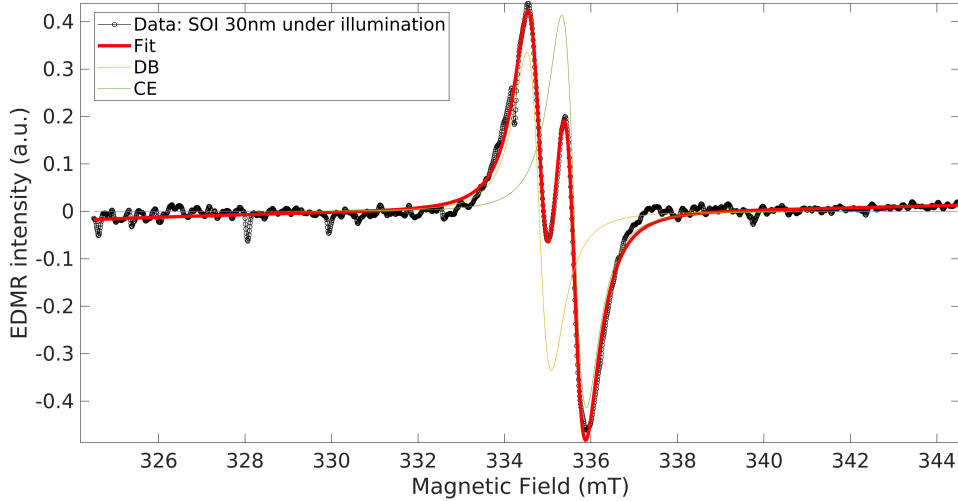
Figure 5.14: Data fitting of the EDMR signal of the 30 nm SOI substrate under illumination. ($P_{\mu w} = 190 \ mW$, T=4.2 K).

5.3 Device layer 20 nm

We now analyzed a Si:P SOI device with a thinner device layer of 20.92 nm. In this case we did not measure the pristine SOI substrate, but we do not expect significant differences from the previous case.

EPR

Electron paramagnetic resonance measurements are performed with microwave source fixed at $\approx$ 9.4 GHz and variable microwave power from 1 mW up to 80 mW. The magnetic field is modulated at frequency $f_{mod} = 100$ kHz with an amplitude of 0.1 mT. All the measurements were performed at 4.2 K. EPR measurements were performed both in dark and under illumination, as a function of the microwave power. The results are shown respectively in figure 5.15a and 5.16a. The P dopants signal can be detected also in this sample, together with a small signal at lower field probably related to the interface. We can also confirm that two signals form at magnetic field lower than 336 mT, when the EPR measurement is taken under photoexcitation and at high microwave power ($P_{\mu w} \geq 30 \ mW$). The power dependency of the signals intensity is reported in figure 5.15b in the case of dark EPR, figure 5.16b for the photoexcited case. In the first case we focus on the phosphorus line, that reaches saturation when the microwave power is increased. The P signal is not particularly affected by illumination. The other two signals present in the photoexcited EPR spectra are strongly dependent on the microwave power. To estimate the intensity we consider only the first signal at lower field, since the peaks are well defined. The second line overlap with the P signal. Also in this sample, we could therefore observe

an out-of-phase EPR signal when the sample is measured at high microwave power and under illumination.
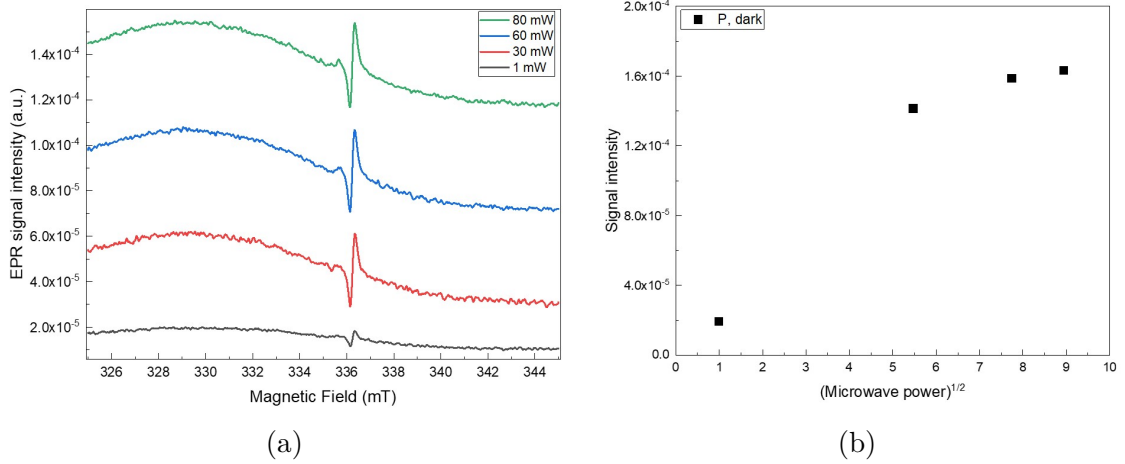
Figure 5.15: (a) EPR spectra of the Si:P SOI sample (20 nm) in dark at 4.2 K. (b) Microwave power dependence of the signal intensity.
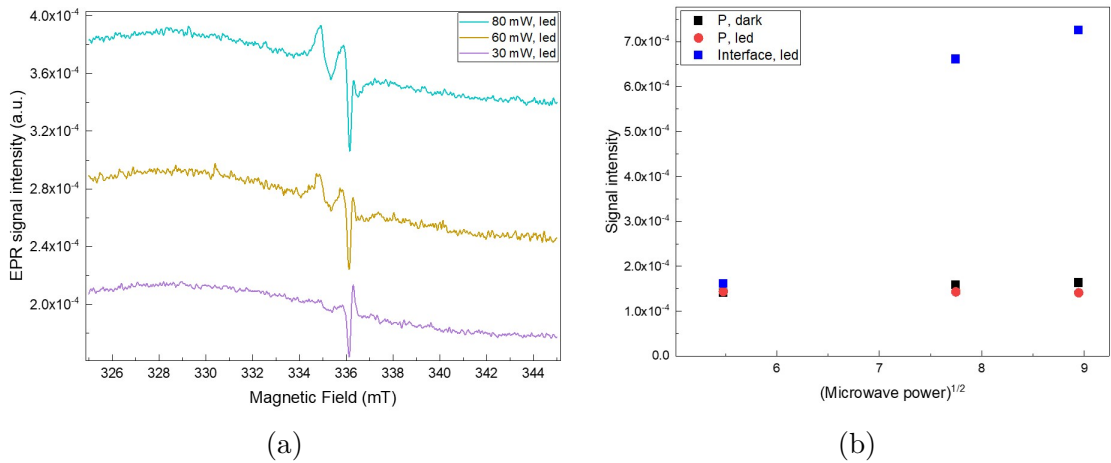
Figure 5.16: (a) EPR spectra of the Si:P SOI sample (20 nm) under illumination at 4.2 K. (b) Microwave power dependence of the signal intensity.

EDMR

I-V measurements were performed at 4.2 K in dark and under illumination. The resulting curves are shown in figure 5.17. The photocurrent in the 20 nm Si:P SOI device is three orders of magnitude greater than the dark current value at 10 V. EDMR measurements were performed at 4.2 K, applying a DC voltage of 10 V to one of the device's electrodes. The microwave power is fixed at 190 mW, and the magnetic field is modulated at frequency $f_{mod} = 5 \ kHz$ with an amplitude of 0.1 mT. All measurements were performed with the sample under illumination, since no signal was detected in dark. Therefore only spin dependent recombination
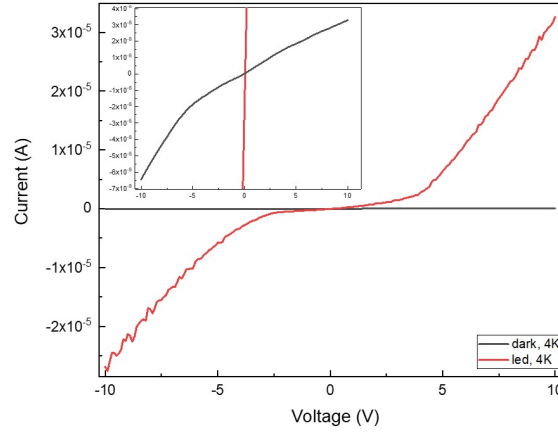
Figure 5.17: I-V measurements of the 20 nm sample at 4.2 K. The inset shows an enlargement of the dark current.
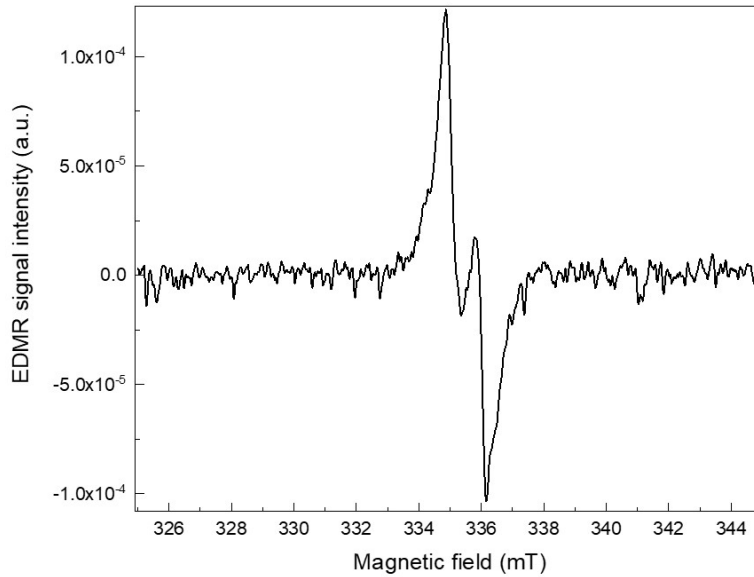
Figure 5.18: EDMR spectrum of the Si:P SOI sample (20 nm), measured under photoexcitation at 4.2 K, with microwave power of 190 mW.

processes are observed in this sample. The resulting EDMR spectrum is presented in figure 5.18. Compare to the previous case, the phosphorus resonance line is not clearly visible. Knowing the g-factor and signal phase from the previous sample, we can detect the P signal as a shoulder in the conduction electrons line centred at approximately g=1.999. The other signal, at higher g, can be attributed to interface defects.

Data fitting and discussion

In this section we discuss the data presented above on the 20 nm sample. Both EPR and EDMR data fitting are presented here. Table 5.4 summarizes the extracted g-

Sample	RMSD	specie	g-factor	linewidth (mT)	weight %
EPR					
Si:P SOI led	0.003	^{31}P	1.9984(2)	0.20(2)	12
		CE	1.9991(2)	0.42(3)	53
		DB	2.0049(5)	0.46(5)	35
Si:P SOI dark	0.011	^{31}P	1.9984(2)	0.20(2)	54
		CE	1.9990(2)	0.35(3)	17
		DB	2.0024(5)	0.45(5)	29
EDMR					
Si:P SOI led	0.015	^{31}P	1.9980(4)	0.14(4)	-1
		CE	1.9994(4)	0.58(4)	46
		DB	2.0045(5)	0.59(5)	53

Table 5.4: Fitting parameters for the EPR and EDMR spectra of the 20 nm sample.

factors, linewidths and re-normalized weights for both the measurements. Figure 5.19 reports the obtained fitting curve in the case of EPR measurements. Also in this case, it is necessary to consider a background signal centred at fixed $g = 1.998$ and with a variable linewidth of (20 ± 5) mT. Compared to the previous case, the background is more intense hindering the fitting procedure. Some mismatches between data and fitting curve are visible for example in the dark EPR spectrum, especially in the background. In both the EPR spectra the P resonance line is clearly visible and it can be fitted with a g-factor of approximately 1.998(4), compatible with the expected value. The linewidth is of 0.2 mT, larger than before, but it could be related again to the poor fitting of the background. In the dark spectrum, the g values of conduction electron and dangling bonds can be extracted from the broad line before the phosphorus signal, even if the fitting is not precise in that region. In the photoexcited spectrum instead, the two signals can be properly fitted. It is worth to note the change in the signal phase, compared to the dark spectrum and also to the phosphorus signal. Linewidths are now better identified and are consistent with the ones found in the previous sample. The same species can be identified fitting the EDMR data. We can conclude that conduction electrons ($g \approx$ 1.999) and interface defects ($g \approx 2.004$) participate in spin dependent recombination process. The positive phase of both the signals suggests an increase in the measured photocurrent in resonant condition. The recombination rate is therefore reduced. The EDMR data fitting considers also a signal due to the phosphorus dopants ($g \approx$ 1.998) with negative phase, similar to the one detected in the previous sample. The actual spin dependent transport mechanism here involved is still under discussion.
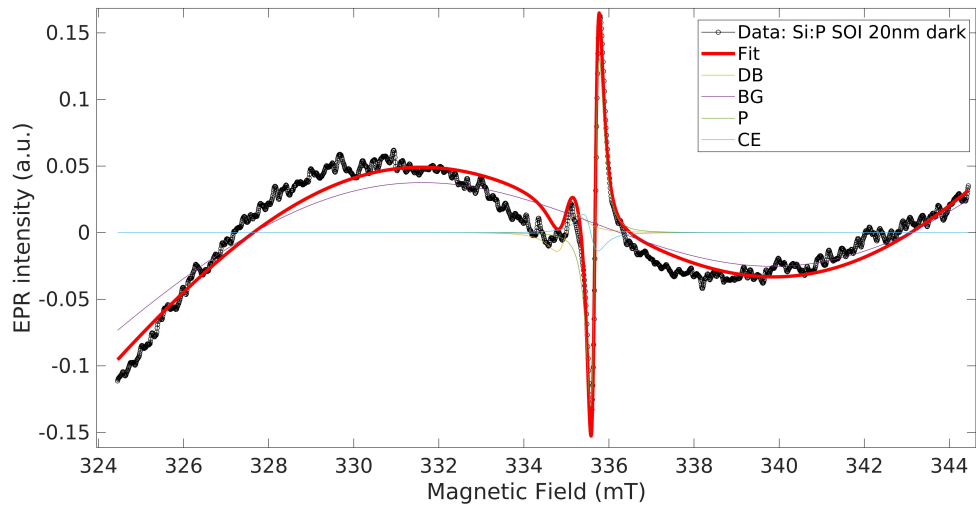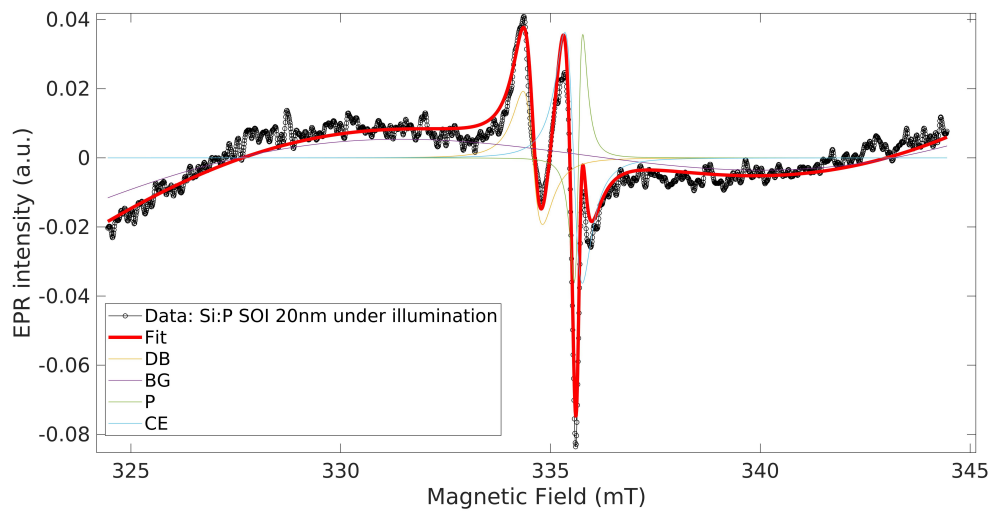
Figure 5.19: Data fitting of the EPR signals of the 20 nm samples, measured at P=80 mW and T=4.2 K: (a) Si:P SOI in dark, (b) Si:P SOI under illumination.
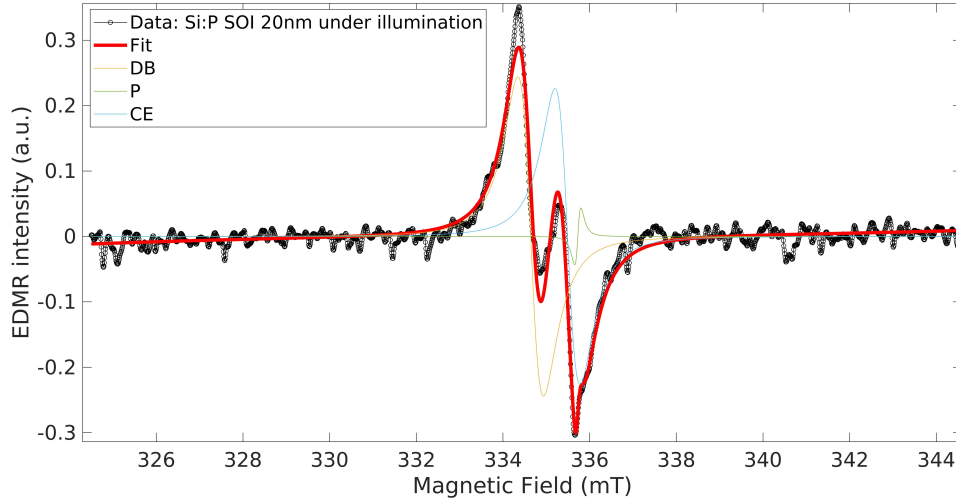
Figure 5.20: Data fitting of the EDMR spectrum of the Si:P SOI sample (20 nm), measured under photoexcitation. ($P_{\mu w} = 190\ mW$, T=4.2 K).

5.4 Device layer 11 nm

Results on the Si:P SOI device with a device layer thickness of 11.35 nm are presented in this section. The analysis of this sample is still in a preliminary stage, further measurement are ongoing.

EPR

EPR measurements were performed on the sample in dark and under illumination, at 4.2 K. Different microwave power, from 1 mW to 80 mW, were tested, with a fixed frequency of $\approx$ 9.4 GHz. The magnetic field is modulated at frequency $f_{mod} = 100$ kHz with an amplitude of 0.1 mT. Compare to the previous cases, the measurements shown in figure 5.24a presented a more intense background signal, that hinders the detection of the other EPR lines. This background signal can be modeled with a g-factor of $\approx$ 1.998 and a linewidth of $\approx$ 23 mT. The background strongly grows in intensity with the microwave power. At least two signals can be detected that we attributed to the phosphorus dopants and interface defects. The microwave power dependence of the signal intensity is shown in figure 5.24b, even if the peaks position and intensity in the spectra are not well defined. Therefore this plot only aims at highlight a possible trend. Differently from all the other samples, the 11 nm does not present an EPR signal at the low microwave power of 1 mW. It could be possible that the background is covering it.

108

(a) (b)
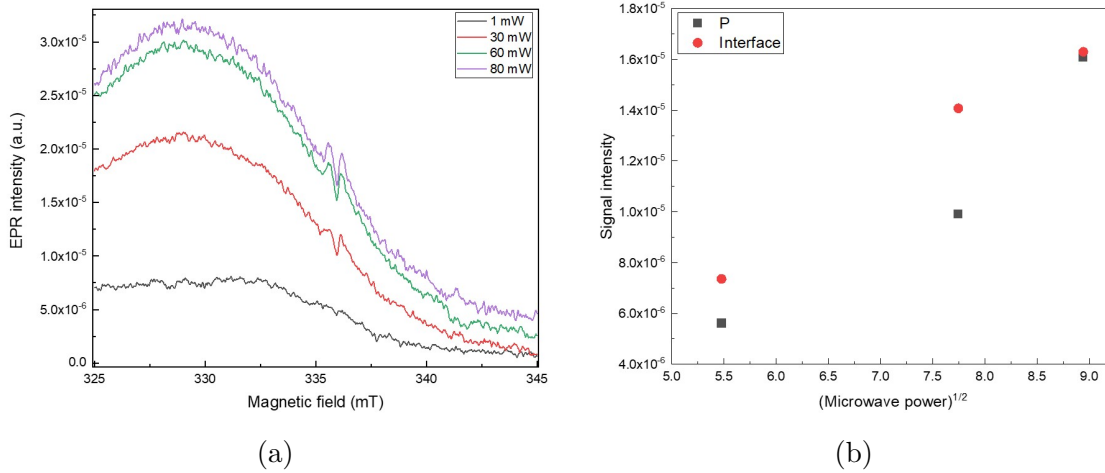
Figure 5.21: (a) EPR spectra of the Si:P SOI sample (11 nm) in dark at 4.2 K. (b) Microwave power dependence of the signal intensity.

EDMR

The comparison between photocurrent and dark current is shown in figure 5.22. I-V curves were taken at 4.2 K. The increase in current under photoexcitation is of three orders of magnitude at 10 V, voltage that's applied to the device in order to perform EDMR measurements. In order to perform EDMR measurements the microwave
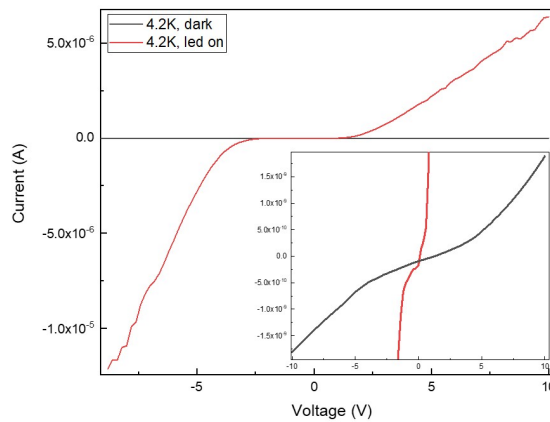
Figure 5.22: I-V measurements of the 11 nm sample at 4.2 K. The inset shows an enlargement of the dark current.

power is fixed at 190 mW, and the magnetic field is modulated at frequency $f_{mod} = 5\ kHz$ with an amplitude of 0.1 mT. The measurements were taken at 4.2 K, with the device under illumination. Also in this case, no signal could be detected without carriers photogeneration. The resulting EDMR spectrum is shown in figure 5.23. Together with the expected signals from the interface, it was also possible to detect two lines with a field separation of $\Delta B \approx 4.1\ mT$. These signals match the hyperfine splitting of the phosphorus isolated dopants, even if the concentration is a little high. Examples of detected phosphorus hyperfine splitting in EDMR experiments

are reported in literature [110] with a concentration of dopants up to $[P] = 1 \times 10^{18} cm^{-3}$.
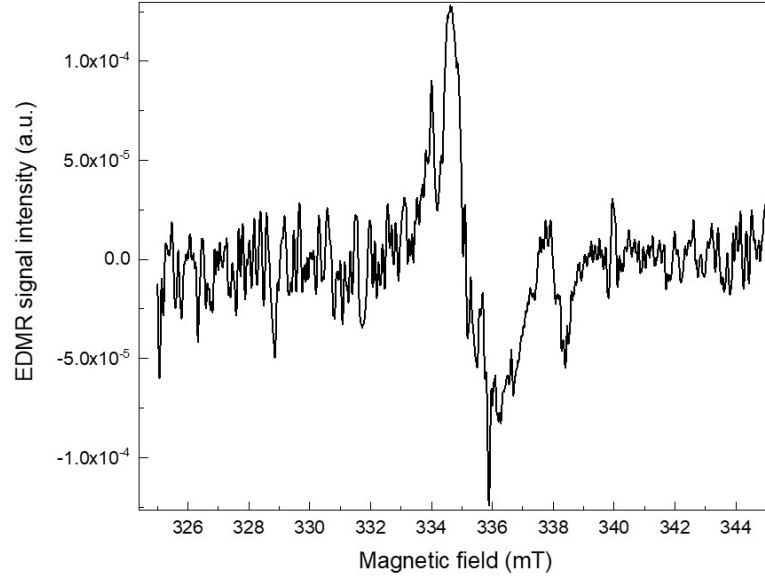
Figure 5.23: EDMR spectrum of the Si:P SOI sample (11 nm), measured under photoexcitation at 4.2 K, with microwave power of 190 mW.

Data fitting and discussion

The fitting of the EPR and EDMR spectra are presented in figure 5.24 (a) and (b) respectively. The extracted g-factors, linewidths and weights are listed in table 5.5. We report the fitting of the EPR spectrum measured at the microwave power of 80 mW. The phosphorus line can be identified with its g-factor of 1.99851 and linewidth of 0.17 mT, similar to what found before. Conduction electrons are also present in the fitting curve, together with another signal at g-factor of 2.00294, lower than the expected ones, considering our previous results. We believe it may be possible that the background is affecting the fitting. The fitting of the EDMR measurements are more complicated, and further simulations are ongoing.
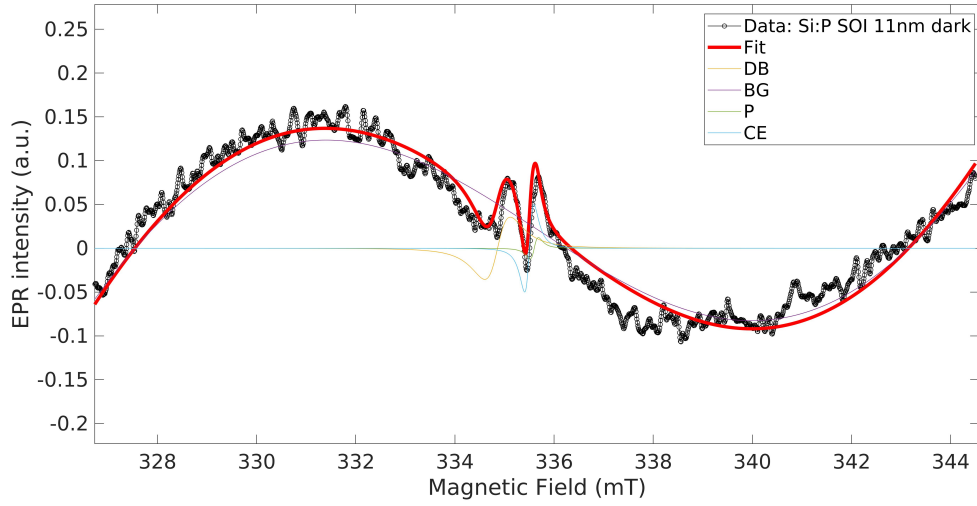
(a)
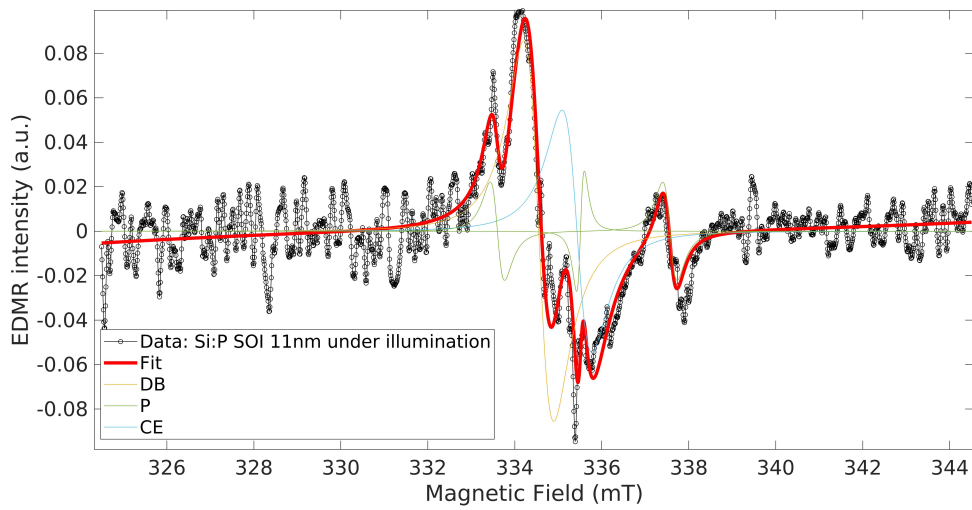
(b)

Figure 5.24: Device layer 11 nm: (a) data fitting of the EPR signal in dark ($P_{\mu w} = 80 \ mW$, T=4.2 K), (b) data fitting of the EDMR signal under photoexcitation ($P_{\mu w} = 190 \ mW$, T=4.2 K).

Sample	RMSD	specie	g-factor	line-width (mT)	weight	A (MHz)
EPR						
Si:P SOI dark	0.018	^{31}P	1.9985(2)	0.17(2)	3	
		CE	1.9991(5)	0.19(5)	15	
		DB	2.0029(5)	0.51(5)	82	
EDMR						
Si:P SOI led	0.01	^{31}P	1.9989(4)	0.18(4)	(-)1	
		CE	1.9995(4)	0.69(4)	36	
		DB	2.0048(5)	0.69(5)	7	
		^{31}P (HF)	1.9985(2)	0.33(2)	56	110(4)

Table 5.5: Fitting parameters for the EPR and EDMR spectra of the 11 nm sample.

5.5 Device layer 6 nm

The last analyzed SOI based device is characterized by a phosphorus doped silicon layer of 6 nm. Also in this case, we report some preliminary results.

EPR

EPR measurements are shown in figure 5.25a. Different microwave power, from 1 mW to 80 mW, were tested, with a fixed frequency of ≈ 9.4 GHz. The magnetic field is modulated at frequency $f_{mod} = 100$ kHz with an amplitude of 0.1 mT. All the measurements were performed at 4.2 K, keeping the sample in dark. Also in this sample, it is possible to note that the background signal plays an important role, with intensity that increases with the microwave power. It is possible to confirm also in this case the presence of phosphorus dopants, resulting in a single line at $g \approx 1.9985$. Another more intense structure is also detected. As the fitting will confirm we are observing the signal from the interface defects and conduction electron, even if the intensity of the latter is small. To evaluate the signal intensity as a function of the square root of the microwave power, we consider the first peak from the left, labeled as interface. Both the signals saturate with the microwave power.

EDMR

I-V measurements were performed at 4.2 K, in dark and under illumination. The resulting dark current and photocurrent are shown in figure 5.26. The ratio between the photocurrent value and the dark one at 10 V is of 5.5×10^3. The EDMR spectrum is presented in figure 5.27. The measurements were taken at 4.2 K, with
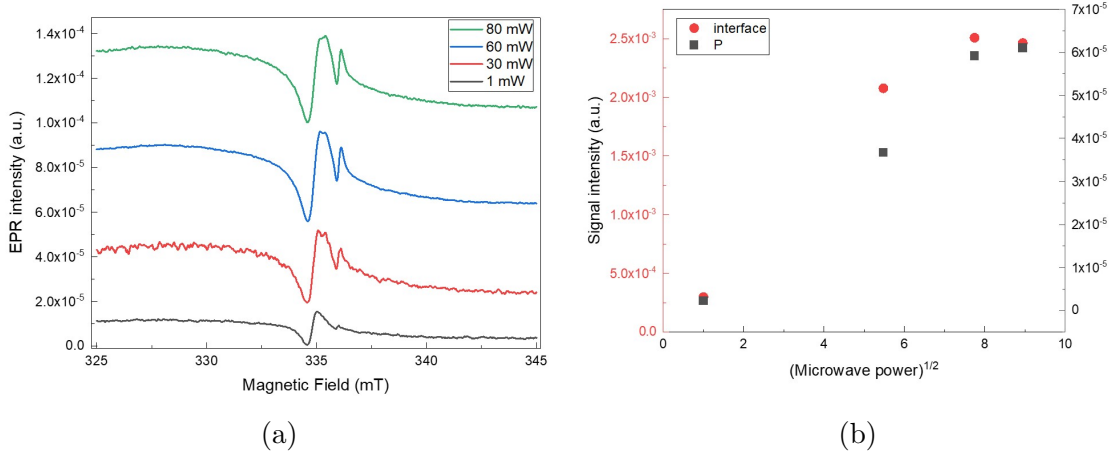
Figure 5.25: (a) EPR spectra of the Si:P SOI sample (6 nm) in dark at 4.2 K. (b) Microwave power dependence of the signal intensity.
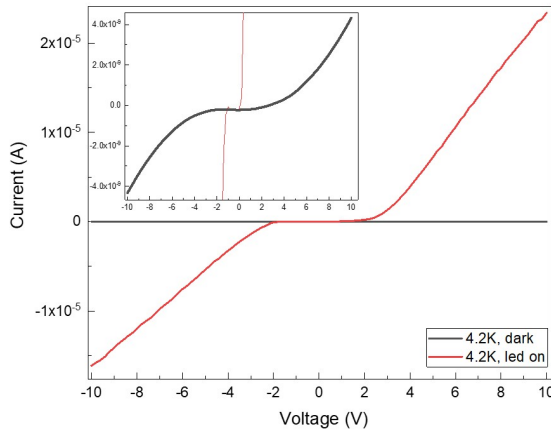
Figure 5.26: I-V measurements of the 6 nm sample at 4.2 K. The inset shows an enlargement of the dark current.

the device under illumination. Also in this case, no signal is detected in dark. The microwave power is fixed at 190 mW, and the magnetic field is modulated at frequency $f_{mod} = 5\ kHz$ with an amplitude of 0.1 mT. Similar considerations as in the previous cases can be made. The main signals come from interface defects and conduction electrons. The phosphorus resonance line can be seen as a little shoulder in the conduction electrons signal.

Data fitting

In this section we show the data fitting of the EPR and EDMR spectrum. The extracted parameters are reported in table 5.6. For the EPR, we report as an example the fitting of the data measured at 80 mW microwave power. We considered a background signal centered at $g = 1.998$ with a linewidth of ≈ 22 mT. The background signal weight is not considered in the normalization of the others. A
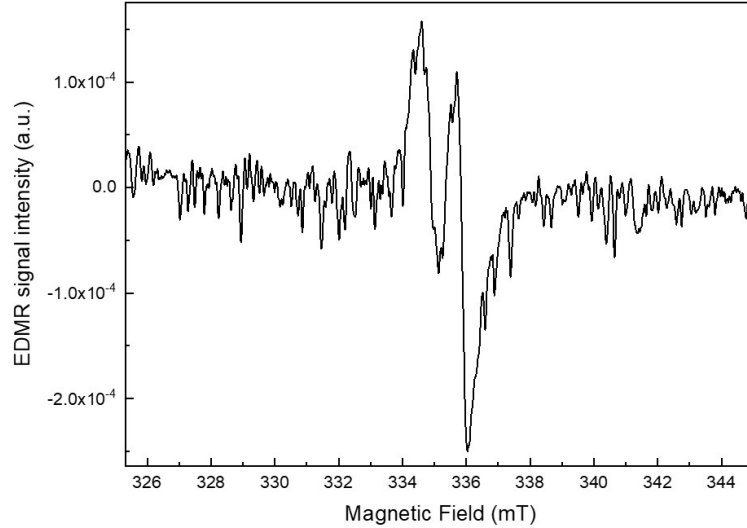
Figure 5.27: EDMR spectrum of the Si:P SOI sample (6 nm) measured at 4.2 K, with microwave power of 190 mW.

Sample	RMSD	specie	g-factor	line-width	weight
		EPR			
Si:P SOI dark	0.02	³¹P	1.9985(2)	0.18(2)	2.4
		CE	1.9989(2)	0.29(2)	1.6
		DB	2.0052(5)	0.69(5)	96
		EDMR			
Si:P SOI led	0.016	³¹P	1.9982(3)	0.19(3)	(-)1
		CE	1.9994(3)	0.49(3)	48
		DB	2.0053(5)	0.62(5)	51

Table 5.6: Fitting parameters for the EPR and EDMR spectra of the 6 nm sample.

single line related to the phosphorus dopants can be identified with a g-factor of ≈ 1.99848 and linewidth of 0.18, consistent with the expected value. A more intense peak can be due to the silicon dangling bonds at $g \approx 2.00522$. Overlapping to this signal, the fitting curve considers also the conduction electrons line at $g \approx 1.99890$. Approximately the same g-factors can be extracted from the fitting of the EDMR spectrum, with small variations. In this spectrum is not straightforward to identify the phosphorus line, since it is only visible as a shoulder in the conduction electrons line. The phase of the P signal, that is negative, suggests a reduction of the current in resonance condition. The other two signals instead have positive phase, meaning that the photocurrent is increased. Conduction electrons and dangling bonds are involved in spin dependent recombination, decreasing the recombination rate.
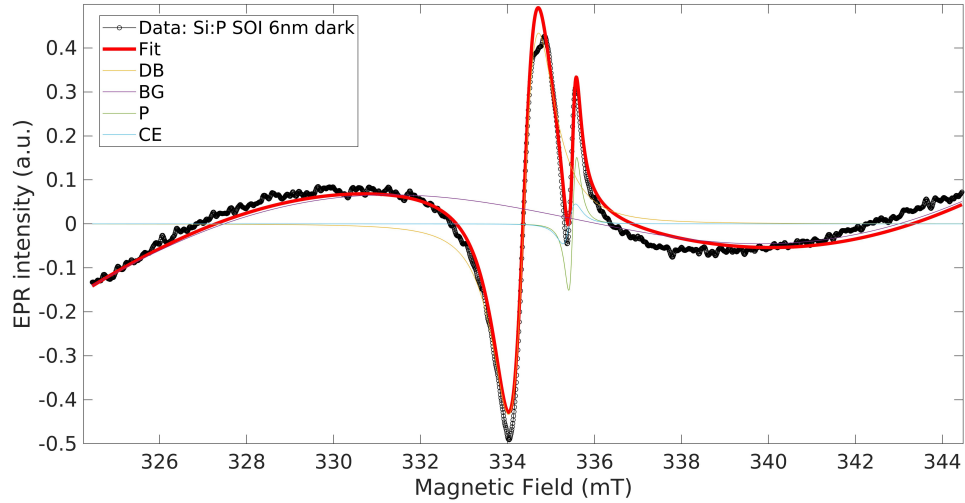
(a)
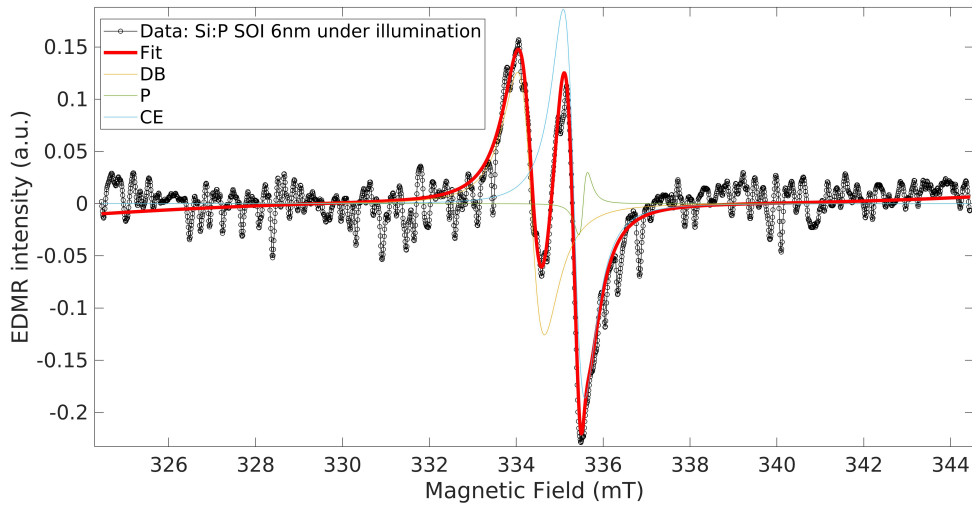
(b)

Figure 5.28: Device layer 6 nm: (a) data fitting of the EPR signal in dark ($P_{\mu w} = 80\ mW$, T=4.2 K), (b) Data fitting of the EDMR signal under photoexcitation ($P_{\mu w} = 190\ mW$, T=4.2 K).

5.6 Discussion

This section summarizes the results obtained so far on the phosphorus doped SOI samples. A comparison between the different analyzed samples is not totally straightforward, but it may help in highlighting some common features and a qualitative behavior. In fact, the thickness of the device layer is not the only changing parameters. Also the concentration of phosphorus impurities presents some variation in the four samples and it needs to be considered.

Figure 5.29 reports the EPR spectra of the different investigated samples. First, we conclude that the phosphorus dopants EPR signal is detected in every sample. Therefore we confirm the efficacy of the fabrication process and of the doping method employed. It is also possible to note that the background signal is always present. However its relative intensity, compared to the other detected signals, seems to become more important for silicon layers with a thickness equal or smaller than 20 nm. Especially in the 11 nm sample, the background signal is predominant and it makes it difficult to detect the other signals. Finally in the sample with the thinnest device layer (6 nm), we observed an inversion in the relative signals intensity. In samples 30 and 20 nm in fact, the phosphorus signal is more intense than the interface signal, while in the 6 nm sample the signal due to the interface defects becomes dominant. Figure 5.30 shows the EDMR spectra of the different phosphorus doped SOI based device. Also in this case, we want to give an overview of the overall behaviour and possible spin dependent transport mechanisms involved. The more complete characterization was performed on the 30 nm device layer sample. We discussed in section 5.2 spin dependent scattering in the 30 nm sample, when investigated in dark. The model we proposed seems to describe reasonably well our experimental observations. However, a question remains open. Contrary to the photo excited EDMR signals, that are well reproduced in every sample, the signal in dark is only detected in the 30 nm sample. We propose here two possible explanations. Considering the discussion in [84], spin dependent scattering is detected only for donors located at a narrow depth window quite far from the 2DEG interface. They show the existence of an optimal distance between the donor impurity ground state wavefunction and the conduction electron wavefunction. It could be therefore possible that in the 30 nm sample, donors are located in this sweet spot respect to the miniband. In the other samples, for geometrical o concentration reasons or both, it could not be the case. Another possible explanation is instead experimental. Considering the dark current level at which EDMR is performed in the different cases, the 30 nm sample is the most conductive one. An off-resonance current of 700 nA is measured in the 30 nm sample, while current of the order of 30 nA, 1 nA and 4 nA are measured in the 20 nm, 11 nm, and 6 nm samples respectively. It could be possible that the

dark EDMR signal is not detected because of poor sensitivity. The variation of the off-resonance photocurrent is instead smaller. Considering now the photocurrent in resonance condition, the behavior is similar in every sample. The main spin dependent mechanism observed is recombination involving interface detects and conduction electrons. It is still to be clarified the role of the phosphorus signal in photoexcited EDMR. If our considerations on the 30 nm sample are correct, then the P signal can be identified also in the 20 nm and 6 nm sample. In these spectra in fact, a shoulder in the conduction electrons line is detected at lower g-factors. As already seen in the EPR measurements the sample with device layer of 11 nm has a different behavior compared to the others and it will require further investigations. It is still not clear why it is possible to detect the phosphorus hyperfine splitting despite the high impurities concentration. A less noisy EDMR measurements will also improve the data fitting, allowing for a better identification of the species involved in spin dependent transport.

This initial analysis reveals some interesting behavior that could be exploited in future SOI based devices. Further investigations are therefore planned, especially concerning the thinner device layer thicknesses. To better investigate the influence of the device layer thickness it will be necessary to have a new set of samples with a given fixed dopant concentration and progressively thinner device layer. It will then be possible to establish when and how quantum confinement starts to affect spin dependent transport. Furthermore concentrations well below the Mott transition will allow to investigate isolated phosphorus dopants. The hyperfine splitting allows to better distinguish the phosphorus signals from the otherwise almost overlapping conduction electrons signals.
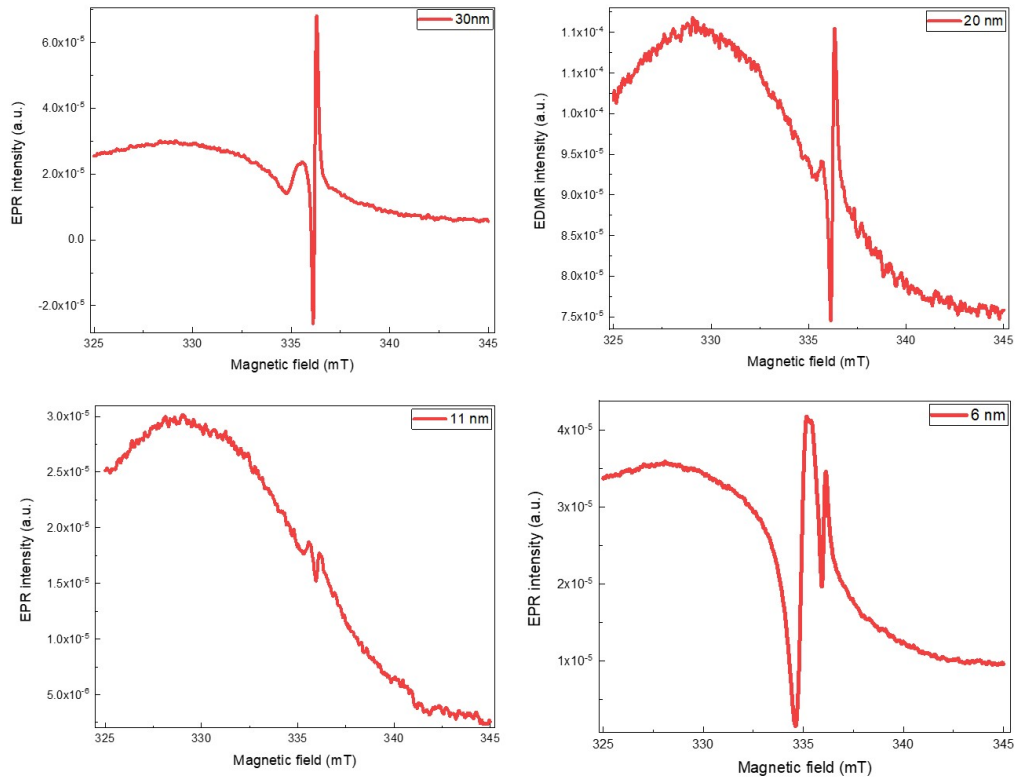
Figure 5.29: EPR spectra of the different Si:P SOI samples measured at 4.2 K, with microwave power of 1 mW. The device layer thickness is indicated in the plot.
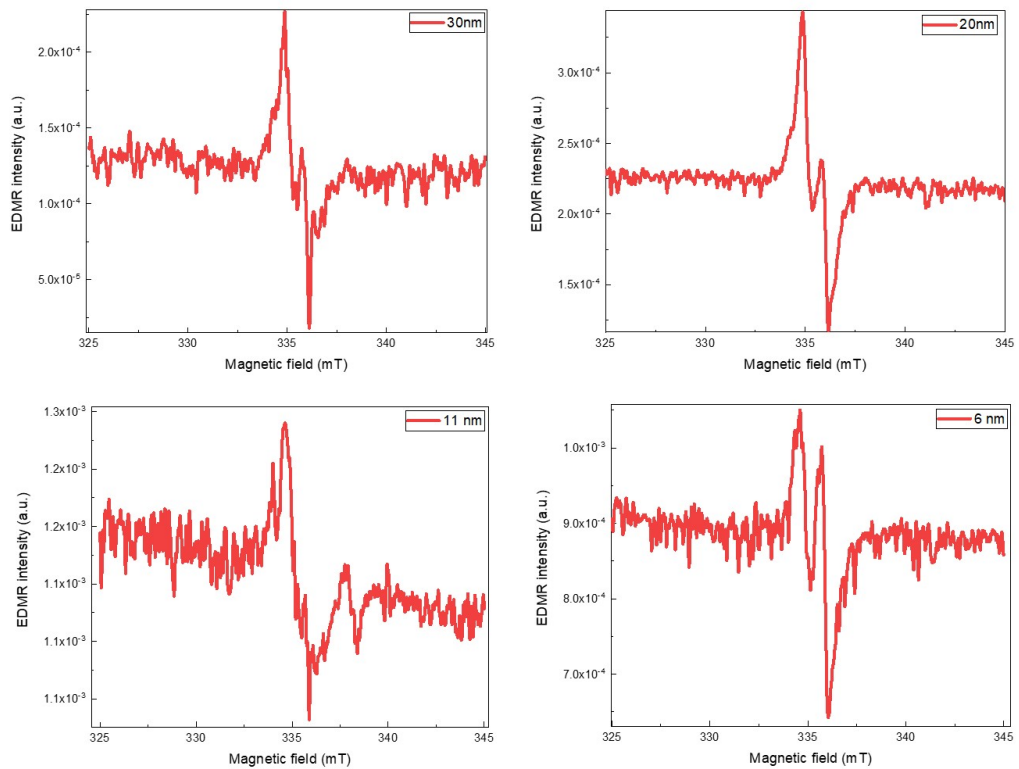
Figure 5.30: EDMR spectra of the different Si:P SOI samples measured at 4.2 K, with microwave power of 190 mW. The device layer thickness is indicated in the plot.

6 Conclusion and Outlook

The research work presented in this thesis focuses on the analysis of charge and spin-dependent transport in doped silicon based devices designed for unconventional computing. We report in this final chapter the main results on the two systems studied: the dopant network processing units and the SOI based devices. An overview of the future research directions is also given in the two cases.

6.1 Dopant Network processing Units

In Chapter 4 we showed the investigation of the DNPUs. In particular, charge and spin dependent transport mechanisms have been analyzed. The DNPUs have already been suggested as a promising scalable platform for in materia computing, as we highlighted in the introduction to the chapter. Within this thesis, we investigated more in depth the physical properties of the dopant networks in order to possibly extend their functionalities.

We analyzed the behavior of three DNPUs having nominal dopants concentrations at the surface of 4×10^{18} atoms/cm^3, 2×10^{18} atoms/cm^3, and 8×10^{17} atoms/cm^3. Charge transport was investigated in different temperature ranges. At high temperatures the DNPUs electrical response is linear, and thermally activated charge transport is observed. The extracted activation energy, properly corrected considering the doping level, the dielectric mismatch and the dielectric anomaly, suggests that only donors located in the first few atomic layers from the device surface contribute to transport. This is reasonably compatible with the DNPU's structure and doping profile. Lowering the temperature the network response becomes progressively highly resistive and non linear. Variable range hopping becomes the dominant charge transport mechanism. Both Efros-Schlovskii and 2D Mott variable range hopping models can describe the experimental data equally well. The extracted values of T_{ES} are consistent with the calculated ones, considering the proper corrections. The Mott temperatures are comparable with similar cases reported in literature. Therefore it was not yet possible to identify the preferential mechanism. The resulting non linearity in the hopping regime is at the base of the DNPU's

working mechanism. However, it is not enough to solve linearly inseparable classification problems, such as the XOR Boolean logic gate. For this kind of problems a more complex non linear response is necessary and it is achieved in the DNPU manipulating the network potential landscape thanks to the control voltages. We showed that the application of control voltages to one or more electrodes results in a complex non linear output current characterized by the presence of negative differential resistance, or at least part of it. We presented the behaviour of the NDR in different electrodes configuration and temperature ranges, demonstrating a correlation between the hopping nature of charge transport and the presence of NDR. The input and control voltages set a potential landscape of the dopant network that results in carriers movement following the allowed paths. The superposition of the current contributions from all the electrodes involved results in the complex output response.

The DNPU behavior was investigated also in response to external stimuli. The network photocurrent was studied by illuminating the DNPU with a red light source, in different electrode configurations. We found an interesting magnetic field dependence of the photoconductivity. A reduction of the photocurrent is in fact observed when a static magnetic field is applied, probably due to an off-resonance recombination.

As presented in section 4.3 and section 4.4, the DNPUs have shown a complex electrical behavior that calls for further investigations. In particular, we highlighted the importance of the diffuse $p-n$ junction in the substrate, whose contribution to charge transport cannot be neglected. To better define this contribution and fully understand the experimental evidence, we are simulating the DNPU with Sentaurus Device. A 2-dimensional simulation of the DNPU top-bottom configuration has already been performed and revealed a mismatch with the experimental data. A 3-dimensional simulation, that considers the entire device's structure, is therefore needed and it has been configured. The simulated DNPU structure is presented in figure 6.1a, with a particular of the active region in figure 6.1b[1]. Simulations of the DNPU's electrical behavior are ongoing and the results will be compared with our experimental data. With these simulations we aim at identifying the currents distribution not only in the active region but also in the substrate. A current density map of the entire DNPU can in fact be simulated, replicating the electrodes configuration of our experiments. It is also possible to simulate the effective potential at every electrode clarifying their role.

---

[1]Courtesy of Dr. Lucia Zullino (STM)

(a)

(b)
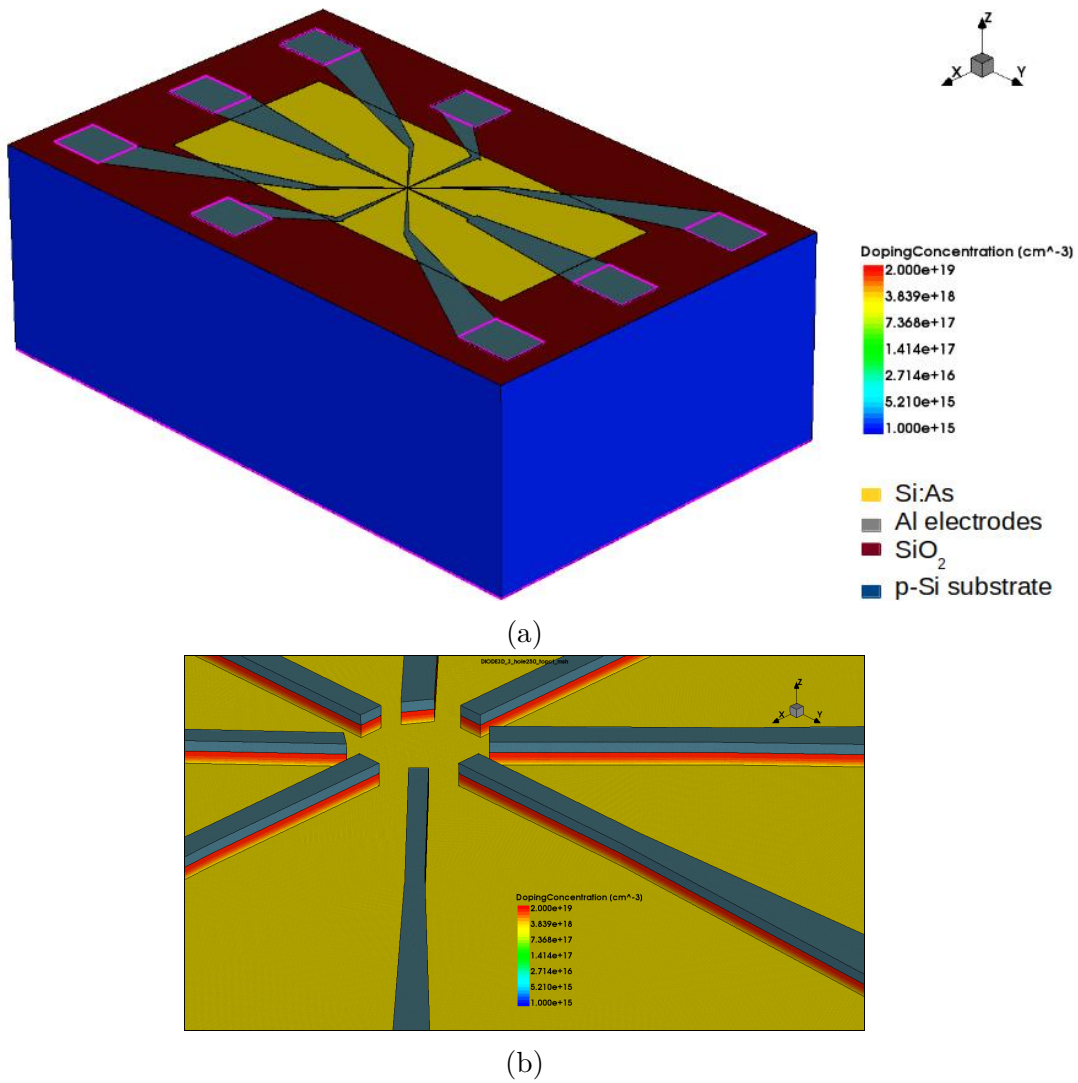
Figure 6.1: (a) 3-dimensional structure of the DNPU simulated with Sentaurus Device. (b) Particular of the DNPU's active region surrounded by the eight electrodes. The doping profile is visible under the electrodes.

Finally, special interest is put into the possibility to incorporate the spin physics of the dopants, to obtain new extended spin dependent functionalities. Spin dependent transport mechanisms were therefore investigated performing EDMR measurements on the DNPU. It was possible to observe spin dependent recombination processes via interface defects and clusters of donors. In particular, in resonant condition the recombination rate is increased resulting in a reduced photocurrent. The arsenic single line detected in resonance is consistent with the high dopant concentrations in the two studied DNPUs. We investigated spin dependent transport in different electrodes configuration, showing the possibility to manipulate the intensity of the resonant signals. A proof-of-concept experiment was also performed on the most doped DNPU, trying to correlate the detection of a spin dependent signal with a certain output state of the dopant network in a Boolean logic gate configuration. More investigations will be carried on in this, and more complex, configurations in order better define this correlation. If confirmed, it could open the way toward a spin dependent tuning of the dopant network response. We already showed that the manipulation of the donor spin state affects charge transport. The next step will be the incorporation of this behavior in the electrostatical tuning at the base of the DNPU's working mechanisms. A combination of electrostatical and magnetic tuning of the dopant network could in principle leads to an increased complexity, and therefore to the possibility to extend the DNPU's functionalities.

6.2 Silicon on Insulator

In Chapter 5 we followed a different approach, starting from the exploration of the material's properties. We investigated a phosphorus doped silicon-on-insulator (SOI) substrate and in particular spin dependent transport mechanisms in it. Four different substrates were investigated, with decreasing thickness of the device layer: 30 nm, 20 nm, 11 nm, and 6 nm. The doping of the device layer was performed by grafting of phosphorus end-terminated polymers. This method is effective in achieving a precise and uniform doping, also confirmed by ToF-SIMS measurement. The concentration in the device layers of the sample investigated has some variations, that do not allow a direct comparison between the sample. Only some overall observations may be given. Electron paramagnetic resonance and electrically detected magnetic resonance measurements were performed on all the substrates and presented in this thesis. EPR results confirm the success of the doping process in every sample. The detected single line due to clusters of phosphorus dopants is consistent with the high impurities concentration. Interesting out-of-phase EPR signals were also detected in the 30 nm and 20 nm samples when investigated under photoexcitation and at high microwave power. More investigations are ongoing to clarify

this mechanism. EDMR measurements allow us to investigate spin dependent transport mechanisms in the phosphorus doped SOI base devices. A deeper analysis was performed on the 30 nm sample, that can be taken as a bulk reference for future investigations. EDMR signals were detected by monitoring both the dark current and the photocurrent, evidence of the presence of both spin dependent scattering and spin dependent recombination. We interpreted the detected reduction of the dark current in resonant condition as an increase in the scattering rate between free electrons in the dopant miniband and localized electrons in clusters of dopants. The same mechanism seems to be present also under illumination. In addition to this, we observed spin dependent recombination. The extrapolated g-factors suggest spin dependent recombination between conduction electrons and silicon dangling bonds. In the particular case of the 30 nm sample, we could detect also the resonant lines of the E' centers and P_{b0} centers. Spin dependent recombination processes seem to be well reproduced in all the investigated sample, while we could detect the scattering mechanism only in the 30 nm sample and possible explanations have been suggested in section 5.6. More investigations are still ongoing on the samples with lower device layer thicknesses and may help clarifying the mechanisms involved. This initial analysis on the phosphorus-doped SOI based devices presents already an interesting rich behavior that calls for further investigations. In particular, this research will proceed in two directions. On the one hand, we want to investigate the possible effects of quantum confinement on the spin dependent transport mechanisms. A new set of samples is therefore needed with a fixed phosphorus concentration and progressively lower device layer thickness. Even better if the same sample is tested with EDMR in between the steps of the 'thinning' procedures. In this way, it should be possible to identify the critical thickness at which quantum confinement affects the spin properties of the device. A lower impurities concentration, below the Mott transition, will also allow to detect the phosphorus hyperfine splitting enabling an easier distinction between the donors signal and the conduction electrons one, otherwise almost overlapping. On the other hand, we want to move towards the realization of a SOI-based device with multiple electrodes, in such a way to consider electrostatical manipulation too. The choice of a SOI substrate, compared to the junction in the DNPU substrate, will prevent current leakage and therefore reduce the device power consumption. Moreover, better control over the dopants concentration can be reached, with consequent proper tailoring of the device conduction properties.

Bibliography

[1]   Gordon E. Moore. 'Cramming more components onto integrated circuits With unit cost'. In: *Electronics* 38.8 (1965), p. 114.

[2]   John M Shalf and Robert Leland. 'Computing beyond Moore'Law'. In: *IEEE Computer Society* 48.12 (2015), pp. 14–23. ISSN: 0018-9162.

[3]   John Shalf. 'The future of computing beyond Moore ' s Law Subject Areas :' in: *Philosophical Transactions Royal Society* 378.20190061 (2020), pp. 1–14.

[4]   M. Mitchell Waldrop. 'More Than Moore'. In: *Nature* 530.7589 (2016), pp. 144–147. ISSN: 14764687. DOI: 10.1038/530144a.

[5]   Anders Andrae and Tomas Edler. 'On Global Electricity Usage of Communication Technology: Trends to 2030'. In: *Challenges* 6.1 (2015), pp. 117–157. DOI: 10.3390/challe6010117.

[6]   Nicola Jones. 'The Information Factories'. In: *Nature magazine* 561 (2018), pp. 163–167. URL: http://scholar.google.com/scholar?hl=en&btnG=Search&q=intitle:The+Information+Factories#0.

[7]   Pascal Stark et al. 'Opportunities for integrated photonic neural networks'. In: *Nanophotonics* 9.13 (2020), pp. 4221–4232. ISSN: 21928614. DOI: 10.1515/nanoph-2020-0297.

[8]   Andrew Adamatzky. *Advances in Unconventional Computing*. Vol. 1. 2017. ISBN: 9783319339238. URL: http://www.springer.com/series/10624.

[9]   A Adamatzky et al. *Unconventional Computing*. Vol. i. 2018. ISBN: 978-1-905986-05-7.

[10] Susan Stepney. 'Guide to Unconventional Computing for Music'. In: *Guide to Unconventional Computing for Music* (2017), pp. 1–21. DOI: 10.1007/978-3-319-49881-2.

[11] Martin Ziegler. 'Novel hardware and concepts for unconventional computing'. In: *Scientific Reports* 10.1 (2020), pp. 10–12. ISSN: 20452322. DOI: 10.1038/s41598-020-68834-1. URL: https://doi.org/10.1038/s41598-020-68834-1.

[12] A Adamatzky et al. *Unconventional computing 2007*. Luniver Press, 2007. ISBN: 9781905986057. DOI: `10.3389/frobt.2014.00010`.

[13] G. Goos, J. Hartmanis and J. Leeuwen. *DNA Computing*. Vol. 1716. 1999, pp. 437–445. ISBN: 3540666664.

[14] Paul R. Prucnal et al. 'Introduction to JSTQE Issue on Photonics for Deep Learning and Neural Computing'. In: *IEEE Journal of Selected Topics in Quantum Electronics* 26.1 (2020). ISSN: 15584542. DOI: `10.1109/JSTQE.2020.2965384`.

[15] Arnoud S. Everhardt et al. 'Periodicity-Doubling Cascades: Direct Observation in Ferroelastic Materials'. In: *Physical Review Letters* 123.8 (2019), p. 87603. ISSN: 10797114. DOI: `10.1103/PhysRevLett.123.087603`. URL: `https://doi.org/10.1103/PhysRevLett.123.087603`.

[16] A. O. Leonov and M. Mostovoy. 'Multiply periodic states and isolated skyrmions in an anisotropic frustrated magnet'. In: *Nature Communications* 6 (2015). ISSN: 20411723. DOI: `10.1038/ncomms9275`.

[17] Jean C. Coulombe, Mark C.A. York and Julien Sylvestre. 'Computing with networks of nonlinear mechanical oscillators'. In: *PLoS ONE* 12.6 (2017), pp. 1–13. ISSN: 19326203. DOI: `10.1371/journal.pone.0178663`.

[18] A Babloyantz and C Lourengo. 'Computation with chaos: A paradigm for cortical activity (attentlveness/categorization/moton detection)'. In: *Proc. Nadl. Acad. Sci. USA* 91.September (1994), pp. 9027–9031.

[19] Olivier Bournez and Amaury Pouly. 'A Survey on Analog Models of Computation'. In: (2021), pp. 173–226. DOI: `10.1007/978-3-030-59234-9{\_}6`.

[20] Carver Mead. 'Neuromorphic Electronic System'. In: *Proceedings of the IEEE* 78.10 (1990). ISSN: 00471852.

[21] A. Mehonic and A. J. Kenyon. 'Brain-inspired computing needs a master plan'. In: *Nature* 604.7905 (2022), pp. 255–260. ISSN: 0028-0836. DOI: `10.1038/s41586-021-04362-w`.

[22] Melanie Poudevigne. '1014'. In: *Medicine & Science in Sports & Exercise* 43.5 (2011), p. 157. ISSN: 0195-9131. DOI: `10.1249/01.mss.0000400410.86982.70`.

[23] Dennis Valbjørn Christensen et al. '2022 Roadmap on Neuromorphic Computing and Engineering'. In: *Neuromorphic Computing and Engineering* (2022). DOI: `10.1088/2634-4386/ac4a83`.

[24]   Mantas Lukoševičius and Herbert Jaeger. 'Reservoir computing approaches to recurrent neural network training'. In: *Computer Science Review* 3.3 (2009), pp. 127–149. ISSN: 15740137. DOI: `10.1016/j.cosrev.2009.03.005`.

[25]   Mantas Lukoševičius, Herbert Jaeger and Benjamin Schrauwen. 'Reservoir Computing Trends'. In: *KI - Künstliche Intelligenz* 26.4 (2012), pp. 365–371. ISSN: 0933-1875. DOI: `10.1007/s13218-012-0204-5`.

[26]   Wolfgang Maass, Thomas Natschlger and Henry Markram. 'Real-Time Computing Without Stable States: A New Framework for Neural Computation Based on Perturbations'. In: *Neural Computation* 14.11 (2002), pp. 2531–2560. ISSN: 1098-6596. DOI: `10.1017/CBO9781107415324.004`.

[27]   T. Natschlger. 'The "liquid computer": A novel strategy for realtime computing on time series (special issue on foundations of information processing).' In: (2002).

[28]   H. Jaeger. 'Harnessing nonlinearity: predicting chaotic systems and saving energy in wireless telecommunication'. In: *Science* (2004), pp. 78–80. URL: `http://www.sciencemag.org/cgi/content/abstract/sci;304/5667/78`.

[29]   Herbert Jaeger. 'The "echo state" approach to analysing and training recurrent neural networks'. In: *GMD Report* 148.4 (2001), pp. 221–223. ISSN: 14715953. DOI: `10.1054/nepr.2001.0035`.

[30]   D. Verstraeten et al. 'Isolated word recognition with the Liquid State Machine: A case study'. In: *Information Processing Letters* 95.6 SPEC. ISS. (2005), pp. 521–528. ISSN: 00200190. DOI: `10.1016/j.ipl.2005.05.019`.

[31]   Amir F. Atiya and Alexander G. Parlos. 'New results on recurrent network training: unifying the algorithms and accelerating convergence'. In: *IEEE Transactions on Neural Networks* 11.3 (2000), pp. 697–709. ISSN: 10459227. DOI: `10.1109/72.846741`.

[32]   L. Appeltant et al. 'Information processing using a single dynamical node as complex system'. In: *Nature Communications* 2.1 (2011), pp. 1–6. ISSN: 20411723. DOI: `10.1038/ncomms1476`.

[33]   Helmut Hauser et al. 'The role of feedback in morphological computation with compliant bodies'. In: *Biological Cybernetics* 106.10 (2012), pp. 595–613. ISSN: 03401200. DOI: `10.1007/s00422-012-0516-4`.

[34]   Gouhei Tanaka et al. 'Recent advances in physical reservoir computing: A review'. In: *Neural Networks* 115 (2019), pp. 100–123. ISSN: 18792782. DOI: `10.1016/j.neunet.2019.03.005`. URL: `https://doi.org/10.1016/j.neunet.2019.03.005`.

[35] Matthew Dale et al. 'A substrate-independent framework to characterize reservoir computers'. In: *Proceedings of the Royal Society A: Mathematical, Physical and Engineering Sciences* 475.2226 (2019), pp. 1–19. ISSN: 14712946. DOI: `10.1098/rspa.2018.0723`.

[36] Paul A. Merolla et al. 'A million spiking-neuron integrated circuit with a scalable communication network and interface'. In: *Sciencemag.Org* 345.7812 (2014), pp. 668–673.

[37] C. Kaspar et al. 'The rise of intelligent matter'. In: *Nature* 594.7863 (2021), pp. 345–355. ISSN: 14764687. DOI: `10.1038/s41586-021-03453-y`. URL: `http://dx.doi.org/10.1038/s41586-021-03453-y`.

[38] Manuel Le Gallo and Abu Sebastian. 'An overview of phase-change memory device physics'. In: *Journal of Physics D: Applied Physics* 53.21 (2020). ISSN: 13616463. DOI: `10.1088/1361-6463/ab7794`.

[39] Geoffrey W. Burr et al. 'Phase change memory technology'. In: *Journal of Vacuum Science & Technology B, Nanotechnology and Microelectronics: Materials, Processing, Measurement, and Phenomena* 28.2 (2010), pp. 223–262. ISSN: 2166-2746. DOI: `10.1116/1.3301579`.

[40] Scott W Fong, Christopher M Neumann and H Philip Wong. 'Phase-change Memory - Towards a Storage-class Memory'. In: *IEEE Transactions on Electron Devices* (2017), pp. 1–13.

[41] David J. Moss et al. 'New CMOS-compatible platforms based on silicon nitride and Hydex for nonlinear optics'. In: *Nature Photonics* 7.8 (2013), pp. 597–607. ISSN: 17494885. DOI: `10.1038/nphoton.2013.183`.

[42] J. Feldmann et al. 'Parallel convolutional processing using an integrated photonic tensor core'. In: *Nature* 589.7840 (2021), pp. 52–58. ISSN: 14764687. DOI: `10.1038/s41586-020-03070-1`.

[43] Kandel ER et al. *Principles of Neural Science.* Fifth. 2014.

[44] Gianluca Milano et al. 'In materia reservoir computing with a fully memristive architecture based on self-organizing nanowire networks'. In: *Nature Materials* 21.2 (2022), pp. 195–202. ISSN: 14764660. DOI: `10.1038/s41563-021-01099-9`.

[45] Kaiwei Fu et al. 'Reservoir Computing with Neuromemristive Nanowire Networks'. In: *Proceedings of the International Joint Conference on Neural Networks* September (2020). DOI: `10.1109/IJCNN48605.2020.9207727`.

[46] J. B. Mallinson et al. 'Avalanches and criticality in self-organized nanoscale networks'. In: *Science Advances* 5.11 (2019), pp. 1–8. ISSN: 23752548. DOI: `10.1126/sciadv.aaw8438`.

[47] Saurabh K. Bose et al. 'Neuromorphic behaviour in discontinuous metal films'. In: *Nanoscale Horizons* 7.4 (2022), pp. 437–445. ISSN: 20556764. DOI: `10.1039/d1nh00620g`.

[48] J. F. Miller and K. Downing. 'Evolution in materio: Looking beyond the silicon box'. In: *Proceedings - NASA/DoD Conference on Evolvable Hardware, EH* 2002-Janua (2002), pp. 167–176. ISSN: 15506029. DOI: `10.1109/EH.2002.1029882`.

[49] Hajo Broersma, Julian F Miller and Stefano Nichele. *Advances in Unconventional Computing*. Vol. 23. Springer International Publishing Switzerland, 2017. ISBN: 978-3-319-33920-7. DOI: `10.1007/978-3-319-33921-4`. URL: `http://link.springer.com/10.1007/978-3-319-33921-4`.

[50] S. K. Bose et al. 'Evolution of a designless nanoparticle network into reconfigurable Boolean logic (Supplementary Information)'. In: *Nature Nanotechnology* 10.12 (2015), pp. 1048–1052. ISSN: 17483395. DOI: `10.1038/nnano.2015.207`.

[51] Tao Chen et al. 'Classification with a disordered dopant-atom network in silicon'. In: *Nature* 577.7790 (2020), pp. 341–345. ISSN: 14764687. DOI: `10.1038/s41586-019-1901-0`. URL: `http://dx.doi.org/10.1038/s41586-019-1901-0`.

[52] P. P. Altermatt, A. Schenk and G. Heiser. 'A simulation model for the density of states and for incomplete ionization in crystalline silicon. I. Establishing the model in Si:P'. In: *Journal of Applied Physics* 100.11 (2006), pp. 1–10. ISSN: 00218979. DOI: `10.1063/1.2386934`.

[53] P. P. Altermatt et al. 'A simulation model for the density of states and for incomplete ionization in crystalline silicon. II. Investigation of Si:As and Si:B and usage in device simulation'. In: *Journal of Applied Physics* 100.11 (2006). ISSN: 00218979. DOI: `10.1063/1.2386935`.

[54] Hibert V. Löhneysen. 'Metal-insulator transition in heavily doped semiconductors'. In: *Current Opinion in Solid State and Materials Science* 3.1 (1998), pp. 5–15. ISSN: 13590286. DOI: `10.1016/S1359-0286(98)80059-4`.

[55] P. F. Newman and D. F. Holcomb. 'Metal-insulator transition in Si: As'. In: *Physical Review B* 28.2 (1983), pp. 638–640. ISSN: 01631829. DOI: `10.1103/PhysRevB.28.638`.

[56] Mikael T. Björk et al. 'Donor deactivation in silicon nanostructures'. In: *Nature Nanotechnology* 4.2 (2009), pp. 103–107. ISSN: 17483395. DOI: `10.1038/nnano.2008.400`.

[57] Mamadou Diarra et al. 'Ionization energy of donor and acceptor impurities in semiconductor nanowires: Importance of dielectric confinement'. In: *Physical Review B - Condensed Matter and Materials Physics* 75.4 (2007), pp. 1–4. ISSN: 10980121. DOI: `10.1103/PhysRevB.75.045301`.

[58] M. Pierre et al. 'Single-donor ionization energies in a nanoscale CMOS channel'. In: *Nature Nanotechnology* 5.2 (2010), pp. 133–137. ISSN: 17483395. DOI: `10.1038/nnano.2009.373`.

[59] T. G. Castner et al. 'Dielectric anomaly and the metal-insulator transition in n-type silicon'. In: *Physical Review Letters* 34.26 (1975), pp. 1627–1630. ISSN: 00319007. DOI: `10.1103/PhysRevLett.34.1627`.

[60] J. Bethin, T.G. Castner and N.K. Lee. 'Polarizabilities of shallow donors in silicon'. In: *Solid State Communications* 14 (1974), pp. 1321–1324.

[61] R. A. Faulkner. 'Higher donor excited states for prolate-spheroid conduction bands: A reevaluation of silicon and germanium'. In: *Physical Review* 184.3 (1969), pp. 713–721. ISSN: 0031899X. DOI: `10.1103/PhysRev.184.713`.

[62] Takahisa Tanaka et al. 'Deionization of Dopants in Silicon Nanofilms even with Donor Concentration of Greater than 1019 cm-3'. In: *Nano Letters* 16.2 (2016), pp. 1143–1149. ISSN: 15306992. DOI: `10.1021/acs.nanolett.5b04406`.

[63] V.F. Gantmakher. *Electrons and disorder in solids.* Oxford University Press, 2005.

[64] Allen Miller and Elihu Abrahams. 'Impurity Conduction at Low Concentrations'. In: *Angewandte Chemie - International Edition* 120.3 (1960), pp. 745–755. ISSN: 15213773. DOI: `10.1002/anie.201911025`.

[65] N. F. Mott. 'Conduction in glasses containing transition metal ions'. In: *Journal of Non-Crystalline Solids* 1.1 (1968), pp. 1–17. ISSN: 00223093. DOI: `10.1016/0022-3093(68)90002-1`.

[66] A. L. Efros and B. I. Shklovskii. 'Coulomb gap and low temperature conductivity of disordered systems'. In: *Journal of Physics C: Solid State Physics* 8.4 (1975). ISSN: 00223719. DOI: `10.1088/0022-3719/8/4/003`.

[67] B. I. Shklovskii and A. L. Efros. *Electronic Properties of Semiconductors.* 1984, pp. 1–42. ISBN: 9783662024058. DOI: `10.1007/978-94-017-5355-5{\_}1`.

[68] G. Lancaster. *Electron spin resonance in semiconductors*. 1966. ISBN: 9781468417395.

[69] Gareth R. Eaton et al. *Quantitative EPR*. 2010. ISBN: 9783211929476.

[70] H.M. Assenheim. *Introduction to Electron Spin Resonance*. Vol. 4. 1. 1967. ISBN: 9781489955043.

[71] G. Feher, R. C. Fletcher and E. A. Gere. 'Exchange effects in spin resonance of impurity atoms in silicon'. In: *Physical Review* 100.6 (1955), pp. 1784–1786. ISSN: 0031899X. DOI: `10.1103/PhysRev.100.1784.2`.

[72] P. M. Lenahan. 'What can electron paramagnetic resonance tell us about the Si/SiO[sub 2] system?' In: *Journal of Vacuum Science & Technology B: Microelectronics and Nanometer Structures* 16.4 (1998), p. 2134. ISSN: 0734211X. DOI: `10.1116/1.590301`.

[73] M. Fanciulli et al. *Defects in High- κ Gate Dielectric Stacks*. Ed. by Physics NATO Advanced Studies Institute Series II: Mathematics and Chemistry. New York: Plenum, 2005, p. 26. ISBN: 9781402043666.

[74] M. Fanciulli et al. 'Electrically detected magnetic resonance of donors and interfacial defects in silicon nanowires'. In: *Nanoscience and Nanotechnology Letters* 3.4 (2011), pp. 568–574. ISSN: 19414900. DOI: `10.1166/nnl.2011.1213`.

[75] M Jivanescu, A Stesmans and V V Afanas'Ev. 'Multifrequency ESR analysis of theEδ defect in a-SiO 2'. In: *Physical Review B - Condensed Matter and Materials Physics* 83.9 (2011), pp. 1–16. ISSN: 10980121. DOI: `10.1103/PhysRevB.83.094118`.

[76] Daniel J. Lepine. 'Spin-Dependent Recombination on Silicon Surfcae'. In: 6.2 (1972), pp. 1–23.

[77] I. Solomon. 'Spin-dependent recombination in a silicon p-n junction'. In: *Solid State Communications* 20.3 (1976), pp. 215–217. ISSN: 00381098. DOI: `10.1016/0038-1098(76)90179-4`.

[78] I. Solomon, D. Biegelsen and J. C. Knights. 'Spin-dependent photoconductivity in n-type and p-type amorphous silicon'. In: *Solid State Communications* 22.8 (1977), pp. 505–508. ISSN: 00381098. DOI: `10.1016/0038-1098(77)91402-8`.

[79] D. Kaplan, I. Solomon and N. F. Mott. 'Explanation of the Large Spin-Dependent Recombination Effect in Semiconductors.' In: *J Phys (Paris) Lett* 39.4 (1978). ISSN: 0302-072X. DOI: `10.1051/jphyslet:0197800390405100`.

[80] G. Mendz and D. Haneman. 'Spin dependent recombination and photoconductive resonance in silicon [4]'. In: *Journal of Physics C: Solid State Physics* 11.6 (1978). ISSN: 00223719. DOI: 10.1088/0022-3719/11/6/004.

[81] P. Christmann, W. Stadler and B. K. Meyer. 'Temperature dependent electrically detected magnetic resonance studies on silicon pn diodes'. In: *Applied Physics Letters* 1521.January 1995 (1995), p. 1521. ISSN: 00036951. DOI: 10.1063/1.113633.

[82] D. D. Thornton and A. Honig. 'Shallow-donor negative ions and spin-polarized electron transport in silicon'. In: *Physical Review Letters* 30.19 (1973), pp. 909–912. ISSN: 00319007. DOI: 10.1103/PhysRevLett.30.909.

[83] Cheuk Chi Lo. 'Electrical detection of spin-dependent transport in silicon'. In: (2011), p. 165. URL: http://scholar.google.com/scholar?hl=en&btnG=Search&q=intitle:Electrical+Detection+of+Spin-Dependent+Transport+in+Silicon#0%5Cnhttp://www.eecs.berkeley.edu/Pubs/TechRpts/2011/EECS-2011-54.html.

[84] Cheuk Chi Lo and Jeffrey Bokor. 'Spin-dependent scattering in a silicon transistor'. In: (2018).

[85] G. Lancaster. *Electron Spin Resonance in Semiconductors*. 1967. ISBN: 9781468417395.

[86] Stefan Stoll and Arthur Schweiger. 'EasySpin, a comprehensive software package for spectral simulation and analysis in EPR'. In: *Journal of Magnetic Resonance* 178.1 (2006), pp. 42–55. ISSN: 10907807. DOI: 10.1016/j.jmr.2005.08.013.

[87] Thomas M. Cover. 'Geometrical and Statistical Properties of Systems of Linear Inequalities with Applications in Pattern Recognition'. In: *IEEE Transactions on Electronic Computers* EC-14.3 (1965), pp. 326–334. ISSN: 03677508. DOI: 10.1109/PGEC.1965.264137.

[88] Hans Christian Ruiz Euler et al. 'A deep-learning approach to realizing functionality in nanoelectronic devices'. In: *Nature Nanotechnology* (2020), pp. 1–106. ISSN: 1748-3395. DOI: 10.1038/s41565-020-00779-y. URL: http://dx.doi.org/10.1038/s41565-020-00779-y.

[89] Bram van de Ven. *Classification using Dopant Network Processing Units.* 2022. ISBN: 9789036553735.

[90] Jianhong Xue et al. 'Mott variable-range hopping transport in a MoS2 nanoflake'. In: *RSC Advances* 9.31 (2019), pp. 17885–17890. ISSN: 20462069. DOI: 10.1039/c9ra03150b.

[91] C. O'Raifeartaigh et al. 'Spin-dependent magnetophotoconductivity in silicon-on-sapphire'. In: *Journal of Applied Physics* 96.11 (2004), pp. 6557–6560. ISSN: 00218979. DOI: `10.1063/1.1814411`.

[92] I. Solomon. *Spin Effects in Amorphous Semiconductors.* Ed. by M.H. Brosky. Vol. 36. Berlin: Springer-Verlag, 1985, Chapter 7. ISBN: 0306420740. DOI: `10.1007/978-1-4613-2513-0{\_}49`.

[93] Victor S. L'vov, Lidia S Mima and O. V. Tretyak. 'Investigation of spin-dependent recombination in semiconductors'. In: *Soviet Physics-JETP* 56.4 (1982), pp. 897–902. ISSN: 00385700. URL: `http://scholar.google.com/scholar?hl=en&btnG=Search&q=intitle:Investigation+of+spin-dependent+recombination+in+semiconductors#0`.

[94] R. Haberkorn and W. Dietz. 'Theory of spin-dependent recombination in semiconductors'. In: *Solid State Communications* 35.6 (1980), pp. 505–508. ISSN: 00381098. DOI: `10.1016/0038-1098(80)90258-6`.

[95] C. C. Lo et al. 'Suppression of microwave rectification effects in electrically detected magnetic resonance measurements'. In: *Applied Physics Letters* 100.6 (2012). ISSN: 00036951. DOI: `10.1063/1.3684247`.

[96] A. Stesmans and V. V. Afanas'ev. 'Si dangling-bond-type defects at the interface of (100)Si with ultrathin HfO2'. In: *Applied Physics Letters* 82.23 (2003), pp. 4074–4076. ISSN: 00036951. DOI: `10.1063/1.1579564`.

[97] A. R. Stegner et al. 'Isotope effect on electron paramagnetic resonance of boron acceptors in silicon'. In: *Physical Review B - Condensed Matter and Materials Physics* 82.11 (2010), pp. 1–11. ISSN: 10980121. DOI: `10.1103/PhysRevB.82.115213`.

[98] Sorin Cristoloveanu and Sheng S. Li. *Electrical Characterization of silicon-on-insulator material and devices.* Ed. by the Kluwer International Series in Engineering and Computer Science Series Editor. 1995. ISBN: 9780792395485.

[99] T. E. Rudenko, A. N. Nazarov and V. S. Lysenko. 'The advancement of silicon-on-insulator (SOI) devices and their basic properties'. In: *Semiconductor Physics, Quantum Electronics and Optoelectronics* 23.3 (2020), pp. 227–252. ISSN: 16056582. DOI: `10.15407/spqeo23.03.227`.

[100] Yang-kyu Choi et al. 'Ultrathin-Body SOI MOSFET for Deep-Sub-Tenth'. In: *IEEE Electron Device Letters* 21.5 (2000), pp. 254–255.

[101] G. K. Celler and Sorin Cristoloveanu. 'Frontiers of silicon-on-insulator'. In: *Journal of Applied Physics* 93.9 (2003), pp. 4955–4978. ISSN: 00218979. DOI: `10.1063/1.1558223`.

[102] Andrea Pulici. 'Doping of thin silicon-on-insulator films by polymers terminated with a phosphorus containing moiety'. In: (2022).

[103] Michele Perego et al. 'Control of Doping Level in Semiconductors via Self-Limited Grafting of Phosphorus End-Terminated Polymers'. In: *ACS Nano* 12.1 (2018), pp. 178–186. ISSN: 1936086X. DOI: `10.1021/acsnano.7b05459`.

[104] Michele Perego et al. 'Silicon Doping by Polymer Grafting: Size Distribution Matters'. In: *ACS Applied Polymer Materials* 3.12 (2021), pp. 6383–6393. ISSN: 26376105. DOI: `10.1021/acsapm.1c01157`.

[105] G. Feher. 'Electron spin resonance experiments on donors in silicon. I. Electronic structure of donors by the electron nuclear double resonance technique'. In: *Physical Review* 114.5 (1959), pp. 1219–1244. ISSN: 0031899X. DOI: `10.1103/PhysRev.114.1219`.

[106] S. Shankar et al. 'Spin resonance of 2D electrons in a large-area silicon MOSFET'. In: *Physica E: Low-Dimensional Systems and Nanostructures* 40.5 (2008), pp. 1659–1661. ISSN: 13869477. DOI: `10.1016/j.physe.2007.10.030`.

[107] J. L. Cantin and H. J. Von Bardeleben. 'An electron paramagnetic resonance study of the Si(1 0 0)/Al2O3 interface defects'. In: *Journal of Non-Crystalline Solids* 303.1 (2002), pp. 175–178. ISSN: 00223093. DOI: `10.1016/S0022-3093(02)00981-X`.

[108] Shigeki Mizushima and Takahide Umeda. 'Electron paramagnetic resonance study of silicon-28 single crystal for realization of the kilogram'. In: *Metrologia* 59.2 (2022). ISSN: 16817575. DOI: `10.1088/1681-7575/ac5584`.

[109] A. Stesmans and V. V. Afanas'ev. 'Electron spin resonance features of interface defects in thermal (100)Si/SiO2'. In: *Journal of Applied Physics* 83.5 (1998). ISSN: 16629752.

[110] P.R. Cullis and J.R. Marko. 'Electron paramagnetic resonance properties of n-type silicon in the intermediate impurity-concentration range'. In: *Physical Review B* 11.11 (1975).

Acknowledgements

First and foremost, I would like to thank my supervisor Prof. Marco Fanciulli, for guiding and mentoring me through these years. His support has been essential for my work and I deeply appreciate it.

I would also like to thank the rest of the MSNS lab: Prof. Fabrizio Moro and Dr. Valerio Di Palma. Thank you Valerio for supporting me and for lightening up my mood in the most critical moments. You have been a precious presence.

I would like to express my gratitude to Dr. Michele Perego and Dott. Andrea Pulici (IMM-CNR) for our collaboration on the SOI project. My acknowledgment also to Dr. Matteo Belli, for supervising my experiment at the IMM-CNR, and to Dr. Emanuele Longo, for his help and the endless hours spent together in the lab.

A special thanks also to Dr. Lucia Zullino (STMicroelectronics) for setting up the simulations on the DNPU, and sharing her time and knowledge with me.

Part of my PhD was carried out in the NanoElectronics group at the University of Twente, The Netherlands. I am deeply grateful for this important period of my life, both professional and personal. First of all, I would like to express my gratitude to Prof. Wilfred van der Wiel for having me and welcoming me in the NE group. Thanks to Dr. Bram van de Ven for teaching me everything about the DNPUs, the research activity in the group, and especially for sharing his office with this talkative italian girl. Thank you Bram, and Maikee, for all the wonderful time spent together and our friendship. A special thanks to Ing. Martin Siekman for his technical support, both in Twente and virtually back in Italy. Thank you Martin for helping me survive in The Netherlands, and for being a good landlord, a personal trainer, and a friend. I probably cannot thank you enough. Unai and Rocio you have become an important reference point in my life. Thank you for being a rational voice in my head when I need it most. A special thanks also to my friendo Reza, Marc, Guus, Bas, Dilu, Pepijn, and the rest of the family I found in the NE group.

Back in Milan, I would like to thank all the people that have contributed to making these years so special. Thanks to Chiara CC, Sandrina, and Valeria, my girls, for all the happy moments spent together and for making this department a better place.